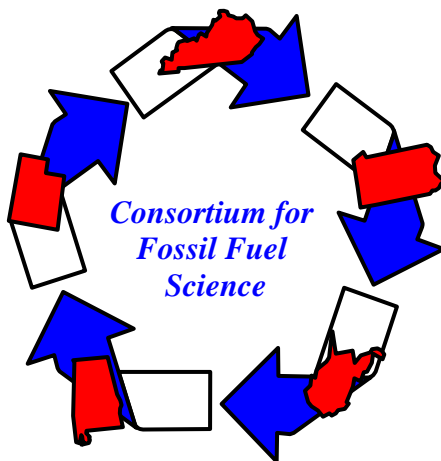


C1 Chemistry for the Production of Ultra-Clean Liquid Transportation Fuels and Hydrogen

Semi-annual six-month report
Research conducted October 1, 2004-March 31, 2005
DOE Contract No. DE-FC26-02NT41594
Prepared by the Consortium for Fossil Fuel Science

Gerald P. Huffman, Director
CFFS / University of Kentucky
533 S. Limestone Street, Suite 107
Lexington, KY 40506
Phone: (859) 257-4027
FAX: (859) 257-7215
E-mail: huffman@engr.uky.edu

Consortium for Fossil Fuel Science
University of Kentucky
West Virginia University
University of Pittsburgh
University of Utah
Auburn University



This report was prepared as an account of work sponsored by an agency of the United States Government. Neither the United States Government nor any agency thereof, nor any of their employees, makes any warranty, express or implied, or assumes any legal liability or responsibility for the accuracy, completeness, or usefulness of any information, apparatus, product, or process disclosed, or represents that its use would not infringe privately owned rights. Reference herein to any specific commercial product, process, or service by trade name, trademark, manufacturer, or otherwise does not necessarily constitute or imply its endorsement, recommendation, or favoring by the United States Government or any agency thereof. The views and opinions of authors expressed herein do not necessarily state or reflect those of the United States Government or any agency thereof.

Table of Contents

Topic	Page
Abstract	1
Executive Summary	2
Chain Initiation of Fischer-Tropsch with Acetylene Incorporation	6
SBA-15 Supported Cobalt and Iron Catalysts for Fischer-Tropsch Synthesis	10
Gas-Phase Incorporation of Organometallic Compounds within Aerogels for Synthesis of Fischer-Tropsch and Water-Gas Shift Catalysts	15
Stability and Structure of Cobalt Catalytic Systems in Fischer-Tropsch Synthesis: Supercritical Fluid Media Versus Conventional Gas-Phase Media	20
Development of Molybdenum-Promoted Catalysts Supported on Activated Carbon for Diesel Fuel Synthesis	26
New Catalysts for the Production of Chemicals, Light Olefins and Hydrogen via C-1 Chemistry	36
What C-13 chemical shift tensors can tell us about metal ligand interactions in catalysts	44
Science behind Catalysis in C1 Reactions: Catalyst characterization and determination of Active Species	46
Mössbauer, XAFS and TEM Analysis of Fe-Mo WGS catalysts	52
Hydrogen Production from Methanol in Supercritical Water	66
Coproduction of Hydrogen and Chemicals by Decomposition of Methanol	71
Hydrogen by Catalytic Reforming of Glycols	75
Hydrogen Production by Catalytic Methane Decomposition using a Semi-Continuous Fluidized-Bed Reactor	78

C1 Chemistry for Production of Ultra-Clean Liquid Transportation Fuels and Hydrogen

U.S. Department of Energy (Fossil Energy) Contract No. DE-FC26-02NT41594

Contact: Gerald P. Huffman, Director, Consortium for Fossil Fuel Science, University of Kentucky, Suite 107 Whalen Building, 533 S. Limestone St., Lexington, KY 40506-0043
(859) 257-4027; FAX: (859)257-7215; huffman@engr.uky.edu

Abstract

Faculty and students from five universities – the University of Kentucky, University of Pittsburgh, University of Utah, West Virginia University, and Auburn University - are collaborating in a research program to develop C1 chemistry processes to produce ultra-clean liquid transportation fuels and hydrogen, the zero-emissions transportation fuel of the future. The feedstocks contain one carbon atom per molecular unit. They include synthesis gas (syngas), a mixture of carbon monoxide and hydrogen produced by coal gasification or reforming of natural gas, methane, methanol, carbon dioxide, and carbon monoxide. An important objective is to develop C1 technology for the production of liquid transportation fuel and hydrogen from domestically plentiful resources such as coal, coalbed methane, and natural gas. An Industrial Advisory Board with representatives from Chevron-Texaco, Eastman Chemical, Conoco-Phillips, the Air Force Research Laboratory, the U.S. Army National Automotive Center (Tank & Automotive Command – TACOM), and Tier Associates provides guidance on the practicality of the research. The current report presents results obtained in this research program during the six months of the subject contract from October 1, 2002 through March 31, 2003. The results are presented in thirteen detailed reports on research projects headed by various faculty members at each of the five CFFS Universities. Additionally, an Executive Summary has been prepared that summarizes the principal results of all of these projects during the six-month reporting period.

Executive Summary

Prepared by Gerald P. Huffman, Director, Consortium for Fossil Fuel Science

(859) 257-4027; huffman@engr.uky.edu

Introduction

The Consortium for Fossil Fuel Science (CFFS), a five university research consortium, is conducting a program of basic research aimed at developing innovative and economical technology for producing clean liquid transportation fuels and hydrogen from coal, natural gas, and other hydrocarbons by C1 chemistry. The research program is made up of thirteen separate but coordinated research projects being conducted at the five CFFS universities, all contributing towards achieving the goal of producing clean, economical transportation fuel from domestic resources. The current report briefly summarizes progress made toward those goals during the first six months of the second year of this research contract. This Executive Summary briefly summarizes the principal results obtained during this period. The appended individual project reports provide more details and contain all the required elements of DOE research contract reports: an introduction, experimental procedures, results and discussion, conclusions, and references. Lists of all publications and presentations resulting from this research contract during this period are also given in these project reports.

Experimental

A discussion of experimental procedures is provided in each of the individual project reports that constitute the bulk of this report.

Results

Liquid fuels from Fischer-Tropsch (F-T) synthesis

Acetylene is incorporated into the F-T reaction much more effectively than are higher acetylenes, a finding similar to results reported with olefin addition. Alpha values decrease upon addition of acetylene, indicating that acetylene, a two-carbon entity serves as a chain initiator. Oxygenates on cobalt catalysts are formed by hydroformylation while oxygenates on iron catalysts proceed according to the ASF distribution.

XRD and magnetic characterization of the used $\text{Co}/\text{Al}_2\text{O}_3$ catalysts indicate that cobalt oxide is reduced in situ during the both gas-phase and supercritical hexane (SC) F-T reactions. In SCH-F-T conditions, the in situ reduction of Co_3O_4 produced both hcp and fcc Co^0 that were stable for long times-on-stream (TOS). As a result, the activity and selectivity of the catalyst in the SCH medium is more stable and recoverable than that under gas-phase F-T conditions.

The addition of Mo to Fe-Cu-K/AC F-T catalysts improves Fe dispersion after catalysts are reduced at 400°C for 12 h. Iron carbide (Fe_2C_5) and magnetite (Fe_3O_4) are detected on spent catalysts by XRD. These are postulated to be active phases for the FTS and WGS reactions. Mo

addition prevents agglomeration of the iron particles during reduction and reaction, leading to improved catalyst stability.

Mössbauer indicate that the Fe in these catalysts is present as superparamagnetic ferrihydrite prior to reaction, while Mo x-ray absorption near-edge spectroscopy (XANES) suggests that the Mo oxidation state is principally as Mo(VI) in molybdate. After reaction, the Fe and Mo are primarily present as carbides. The Mössbauer spectra resemble those of ϵ and χ carbide. The question of whether the Mo and Fe are present in the same carbide or oxide phase or form distinct carbide and oxide phases is less clear. The preliminary TEM study was inconclusive; Mo-free Fe-rich particles, Fe-free Mo particles, and some Fe-Mo mixed particles were observed.

Production of light olefins (C_2 - C_4) from methanol or syngas over silicoaluminophosphate (SAPO) catalysts provides an indirect way of converting fossil resources to industrially valuable olefins and other value-added products such as polymers and fine chemicals. Catalytic activity and selectivity for light olefins can be influenced by many catalyst parameters such as silicon content, acid site density, acid strength, crystallite size, and nature of template.

The high surface areas and highly porous nature of aerogels offer promise not just for the F-T reaction, but also for the WGS. The use of gas phase deposition is likely to generate catalyst centers in very highly dispersed form, whether for aerogels, zeolites, or supports. It also appears that a silica aerogel structure can be of value in providing a robust framework onto which more fragile support species, such as ceria, can be anchored. New ^{13}C NMR techniques are being developed to investigate metal-ligand complexes in these catalysts.

Six different SBA-15 supported cobalt and iron catalysts were prepared to study the impact of different impregnation methods, active metals, and aluminum incorporation in SBA-15 on catalytic activity in Fischer-Tropsch (FT) synthesis. The cobalt impregnation method had a significant effect on catalytic activity and selectivity because of differences in reducibility of cobalt oxides. Aluminum added to an iron-based catalyst is also advantageous.

Hydrogen

There are several advantages of carrying out the reforming reactions in supercritical water over the conventional processes. The density of supercritical water is higher than that of steam, which results in a high space-time yield. The higher values of thermal conductivity and specific heat of supercritical water are beneficial for the endothermic reforming reaction. H_2 is available at a high pressure and can be stored directly, avoiding the problems associated with compression. Hydrogen volume percentages produced during reforming of methanol in supercritical water in the output stream are ~98%, while CO and CO_2 percentages are <2 %. CH_4 formation can be suppressed by (1) operating at a low residence time, (2) using a Ni-Cu reactor or (3) adding K_2CO_3 or KOH in the feed.

Thermodynamically, co-production of hydrogen and methyl formate from methanol is favored at temperatures below 220°C. At temperatures higher than 250°C, complete methanol decomposition is favored to form syngas with a ratio of $H_2/CO=2$. The presence of steam favors hydrogen but decreases methyl formate production. Copper catalysts are active for decomposition of methanol in the order of $Cu/Al_2O_3 > Cu/ZSM-5 > Cu/MgO$.

To overcome the plugging of the fixed bed reactor by carbon nanotubes (CNT) during catalytic methane dehydrogenation and to make hydrogen and nanotube production continuous,

fluidized-bed mode and mixed-mode catalytic dehydrogenation experiments were performed. These experiments showed that the hydrogen production is most efficient in a fixed bed mode. Tumbling and inter particle collisions of bed material did not separate nanotubes anchored to the catalyst bed particles as hoped for. Instead, a very high methane flow rate was used to rapidly blow the all bed material out of the reactor and it was replenished with fresh catalyst.

Partial oxidation of propane was investigated using Pt/CeO₂ catalysts, with CeO₂ prepared by different techniques. It was found that Pt catalyzes the reduction of surface CeO₂ but has little effect on reduction of bulk CeO₂. Pt on CeO₂ prepared by a decomposition method exhibited the highest BET surface area, reducibility, and catalytic activity for partial oxidation of propane at 700°C.

Experiments on the aqueous-phase reforming of ethylene glycol and of glycerol in a continuous system have shown that significant amounts of hydrogen are produced with low CO content. This method for producing hydrogen appears promising for use with PEM fuel cells.

The dehydrogenation-hydrogenation of cyclic hydrocarbons, i.e. cyclohexane, methylcyclohexane, tetralin, etc. has been proposed as a possible technology to store, transport, and locally produce hydrogen. Some advantages of this are lack of poisonous CO, reaction reversibility, relatively high hydrogen content (6-8 wt.%), and convenient liquid phase transportability. Pt catalysts supported on mesoporous SBA appears to offer good potential for dehydrogenation and hydrogenation of cyclic hydrocarbons such as cyclohexane, although Ru impregnated SBA is also active. Catalyst particle size reduction is effective in increasing olefins yield and lifetime in some, but not all, SAPO catalysts. Ru addition to the SAPO catalysts did not appear to offer significantly increased lifetimes, although other metals may be effective in this regard.

Conclusions

Liquid fuels from Fischer-Tropsch (F-T) synthesis

1. Small (~1%) additions of acetylene to the F-T reaction causes chain initiation and promotes oxygenate formation.
2. XRD, magnetic studies, Mössbauer spectroscopy, XAFS spectroscopy, and TEM have been used to obtain detailed structural information for F-T, WGS, and dehydrogenation catalysts.
3. The addition of Mo to Fe-Cu-K/AC F-T catalysts prevents agglomeration of catalyst particles during reduction and reaction, leading to improved catalyst stability. Mössbauer and XAFS spectroscopy indicate that the Fe and Mo are primarily present as carbides.
4. A method to synthesize light olefins (C₂-C₄) from methanol or syngas over SAPO catalysts has been developed.
5. The use of gas phase deposition to place highly dispersed metal catalysts on high surface areas and high porosity aerogels offers promise for both the F-T and the WGS reactions. ¹³C NMR techniques are being developed to investigate metal-ligand complexes in these catalysts.
6. The activity of F-T catalysts consisting of Co and Fe supported on SBA-15 supports prepared by different impregnation methods is being investigated.

Hydrogen

1. Hydrogen volume percentages produced during reforming of methanol in supercritical water in the output stream are ~98%, while CO and CO₂ percentages are <2 %.
2. A continuous fluidized-bed/fixed-bed catalytic methane dehydrogenation reactor was developed for continuous hydrogen and nanotube production.
3. Several copper catalysts have been shown to be active for the co-production of hydrogen and methyl formate from methanol.
4. Partial oxidation of propane was investigated using Pt/CeO₂ catalysts.
5. Aqueous-phase reforming of ethylene glycol and of glycerol in a continuous system have produced significant amounts of hydrogen with low CO content.
6. Pt supported on mesoporous SBA appears to offer good potential for dehydrogenation and hydrogenation of cyclic hydrocarbons such as cyclohexane, methylcyclohexane, tetralin, etc. that have been proposed for storage, transportation, and local production of hydrogen.

CHAIN INITIATION OF FISCHER-TROPSCH WITH ACETYLENE INCORPORATION

Yulong Zhang, Li Hou, John W. Tierney and Irving Wender

Department of Chemical and Petroleum Engineering, University of Pittsburgh

Introduction

The Fischer-Tropsch (F-T) synthesis converts syngas (CO and H₂), which can be produced from coal, natural gas, biomass and any carbonaceous material, into long chain hydrocarbons which can be transformed to fuels and chemicals. The mechanism of the F-T reaction is still under debate although it has been investigated for many years. It is difficult to distinguish among the many complex intermediates formed during F-T reactions. Schulz¹ has pointed out that the F-T regime is established during the synthesis by restructuring the catalyst surface and suppressing undesired reactions. The use of probe molecules has been shown to be an effective way to study the F-T mechanism².

The F-T synthesis is a stepwise growth of hydrocarbon chains by addition of monomeric units. Unlike usual polymerization processes, the reaction proceeds by addition of monomers formed in-situ. In previous studies, we found that long chain alkynes are incorporated more easily than corresponding alkenes³. It has been reported that ethylene is 10 to 40 times more easily incorporated into the F-T synthesis than are higher olefins. We have reported incorporation of long chain alkynes, phenylacetylenes and preliminary results of incorporation of acetylene on F-T cobalt and iron catalysts. In this work, the effects of operating variables such as temperature and pressure on co-feeding of acetylene were investigated. A rhodium catalyst is also studied due to its characteristics in hydroformylation. Possible pathways of F-T synthesis are discussed and a chain initiation mechanism with a two-carbon entity is proposed.

Experimental

Supported cobalt catalysts were prepared by incipient-wetness impregnation of cobalt nitrate on alumina. A rhodium catalyst was prepared by incipient wetness impregnation of rhodium (III) chloride hydrate on alumina. A precipitated iron catalyst with a composition of 100Fe/4.4Si/1.25K was obtained from Dr. B. Davis of the University of Kentucky.

The F-T reaction was carried out in a computer controlled fixed bed reactor (stainless-steel with i.d. 3/8 inches). Acetylene was introduced from a tank of premixed gas containing (mol): 1% acetylene, 10% Ar, 44% CO, and 45% H₂ obtained from Praxair. H₂ was added when the H₂/CO ratio needed to be adjusted. Co catalysts were activated by H₂ at a rate of 50 ml/min, with a temperature program ramping from room temperature to 350°C at 1°C/min, holding at 350°C for 10 hours. Fe catalysts were activated similarly but kept at 350°C for 5 hours and 450°C for 2 hours. The F-T reaction was started by gradually increasing the CO and H₂ flow rate to avoid a temperature surge due to active sites present in the fresh catalysts. Products were analyzed by two online GCs (HP6890 and HP5890).

Results and Discussion

The addition of acetylene on cobalt catalysts increases the yield of C₂⁺ products up to about C₁₀. It can be seen from Figure 1 that C₃ has a three fold increase upon addition of 1% acetylene.

Compared to 1-hexyne, acetylene is 3 to 4 times easier to incorporate into the F-T products. As shown in Table 1, a significant amount of acetylene is dimerized to C₄ on Co and Rh catalysts but very little on the Fe catalyst. Dimerization is not a part of the F-T reaction since it is not sensitive to sulfur poisoning. It is most likely due to the acidic Al₂O₃ support used in cobalt and rhodium catalysts. C₄ products are mainly internal olefins; however, they are also capable of chain initiation. As with co-feeding of internal acetylenes reported earlier³, isomers such as 2-methylbutane and 3-methylpentane are produced when acetylene is co-fed.

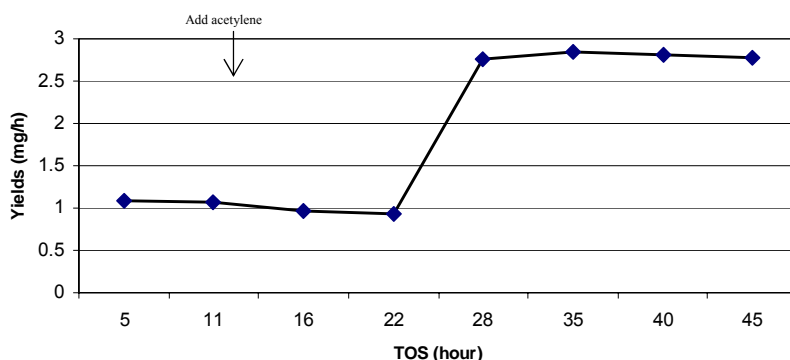


Figure 1. Yield of C₃ hydrocarbons with TOS on a cobalt catalyst (10Co/90Al₂O₃) at 100 psi., 180°C, H₂/CO=1, 1% acetylene.

The effects of temperature and pressure on F-T without/with acetylene were investigated. Compared to the base reaction (without acetylene), co-feeding acetylene greatly increases the amount of F-T products at various temperatures for both Co and Fe catalysts. Incorporation is lower at very low temperatures, e.g. at 120°C, but becomes stable at temperatures above 180°C, as shown in Table 1. About 60% of acetylene is incorporated into higher products with both catalysts. The rhodium catalyst shows a low incorporation rate, probably due to its low F-T activity. Increase in pressure from 100 to 700 psi. has little effect on the incorporation ratio on Co and Fe catalysts, but it enhances oxygenate formation.

Table 1 Comparison of incorporation of acetylene on several F-T catalysts at 220°C

	Temperature (°C)	Hydrogenation (%)	Dimerization (%)	Incorporation (%)
10Co/90Al ₂ O ₃	120	40	28	32
	180	8	36	56
	220	14	27	59
100Fe/4.4Si/1.25K	180	30	7	63
	220	33	7	60
	260	34	5	61
5Rh/95Al ₂ O ₃	220	20	65	15

A striking effect of co-feeding acetylene is initiation of the F-T chain growth at lower temperatures. At 120°C, appreciable amounts of F-T products can still be obtained on cofeeding of 1% of acetylene; the FT reaction does not take place at such a low temperature. Incorporation of acetylene on a Co catalyst only produces C₃ and a small amount of C₅ oxygenates, apparently by hydroformylation of adsorbed unsaturated C₂ and C₄ species. Iron catalysts, however, produce a spectrum of oxygenates which follows the Anderson-Schultz-Flory (ASF) distribution as shown in Figure 2.

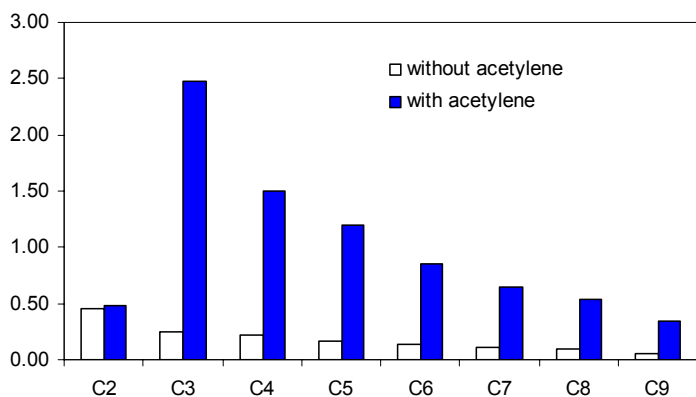


Figure 2. Oxygenated product distribution without/with acetylene incorporation on an iron catalyst (10Co/90Al₂O₃) at 300psi, 180°C, H₂/CO=1, 1% acetylene.

Acetylenes initiate the chain but are not incorporated into the growing chain. The alpha value of the F-T reaction declines with co-fed acetylene due to the increasing number of chain initiators. There are many studies on the nature of the species formed from two-carbon entities added to an F-T reaction^{2,4,5}. These include ethylene, vinyl ethylidene, ethylidyne and, undoubtedly, a variety of other similar adsorbates. Zaera⁶ has provided surface science evidence that two-carbon entities interconvert on the surface of a metal catalyst, as shown in Figure 3.

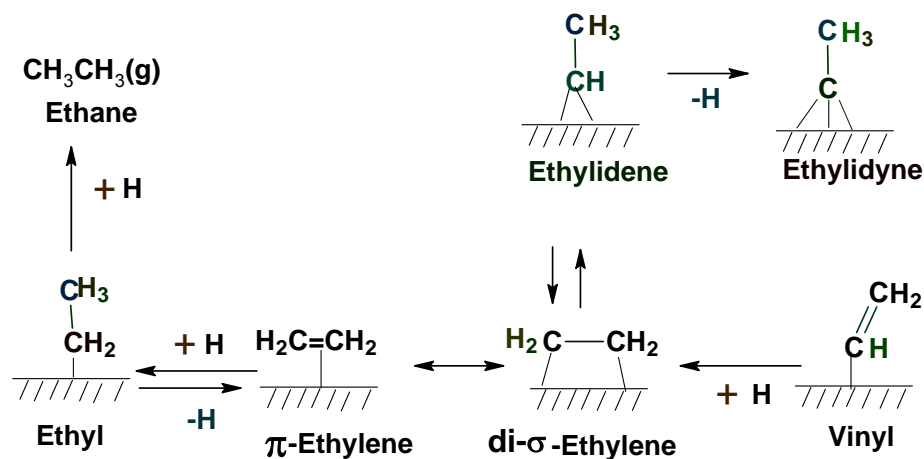


Figure 3. Reaction mechanisms for the conversion of ethylene on Pt (111)⁸

Alkylidyne species are well-known in adsorption studies on metal atoms. It is possible that terminal acetylenic compounds are adsorbed at low temperature on F-T catalysts to form alkylidyne species which initiate the reaction. Stable alkylidyne compounds have been reported in organometallic complexes having one and two metal centers; however, the most stable alkylidyne species is that in which nests in the center of three metal atoms. This has been substantiated by the synthesis of an organometallic compound, ethylidyne tricobalt nonacarbonyl ($\text{CH}_3\text{CCo}_3(\text{CO})_9$). There is undoubtedly a close relation between unsaturated hydrocarbon ligands in organometallic compounds and those on metal surfaces.

Conclusions

Acetylene is incorporated into the F-T reaction much more effectively than are higher acetylenes, a finding similar to results reported with olefin addition. Alpha values decrease upon addition of acetylene, indicating that acetylene, a two-carbon entity serves as a chain initiator. Oxygenates on cobalt catalysts are formed by hydroformylation while oxygenates on iron catalysts proceed according to the ASF distribution.

References

- (1) Schulz, H.; Nie, Z. Q.; Ousmanov, F. *Catal. Today* **2002**, *71*, 351-360.
- (2) Turner, M. L.; Marsih, N.; Mann, B. E.; Quayoum, R.; Long, H. C.; Maitlis, P. M. *J. Am. Chem. Soc.* **2002**, *124*, 10456.
- (3) Zhang, Y.; Hou, L.; Tierney, J. W.; Wender, I. *Top. Catal.* **2005**, *33*.
- (4) Slivinskii, E. V.; Romyantsev, V. Y.; Voitsekhovskii, Y. P.; Zvezdkina, L. I.; Loktev, S. M. *J. Catal.* **1990**, *123*, 333-40.
- (5) Loktev, S. M. *J. Mol. Catal.* **1982**, *17*, 225-30.
- (6) Long, H. C.; Turner, M. L.; Fornasiero, P.; Kaspar, J.; Graziani, M.; Maitlis, P. M. *J. Catal.* **1997**, *167*, 172.
- (7) Zaera, F.; Bernstein, N. *J. Am. Chem. Soc.* **1994**, *116*, 4881.
- (8) Zaera, F. *Chem. Rev.* **1995**, *95*, 2651.

SBA-15 Supported Cobalt and Iron Catalysts for Fischer-Tropsch Synthesis

Dae Jung Kim, Brian C. Dunn, and Edward M. Eyring

Department of Chemistry, University of Utah Salt, Lake City, UT 84112

Introduction

Fischer-Tropsch (FT) synthesis is a promising pathway to very clean alternative fuels derived from coal syngas. It is important to develop active catalysts with high selectivity for production of long chain hydrocarbons. The activity of catalysts for FT synthesis depends primarily on the overall amount of exposed metal atoms. Thus, a highly active catalyst requires a high dispersion of cobalt metal. Mesoporous silica materials such as SBA-15 have been recently used as supports for cobalt.¹⁻⁴ The high surface area (500 - 1500 m²/g) of the mesoporous materials gives higher metal dispersions at higher cobalt loadings compared with conventional amorphous silicas. Furthermore, the uniform pore diameters (2 - 30 nm) of the mesoporous silica materials permit better control of the cobalt particle size and the distribution of hydrocarbon products from the FT synthesis.⁵ We have proposed that surface modification of SBA-15 via silylation increases the catalytic activity and hydrocarbon selectivity in FT synthesis.⁶

The objectives of this present study are to determine the relative merits of impregnation methods, advantages of iron over cobalt and the consequences of aluminum incorporation in SBA-15 on catalytic activity in Fischer-Tropsch synthesis. Six different catalysts were prepared. The physical and chemical properties of the catalysts were obtained from N₂ adsorption/desorption, XRD and TPR experiments. The catalytic performance in FT synthesis was evaluated with a fixed-bed reactor.

Experimental

Catalyst preparation. SBA-15 was obtained by a procedure described elsewhere.^{6,7} Triblock polymer Pluronic P123 (EO₂₀PO₇₀EO₂₀, M_{av} = 5800, BASF) was used as the structure-directing agent of SBA-15. Anhydrous sodium metasilicate (Na₂SiO₃, Aldrich) was used as the silica source of SBA-15. Aluminum incorporation in SBA-15 was achieved using the following post-synthesis procedure. 1.0 g of calcined pure SBA-15 was added to a 50 mL ethanol solution containing AlCl₃ (Aldrich). The mixture was stirred at ambient temperature overnight, and filtered using a glass membrane filter. The filtered sample was dried in air at 100 °C overnight, and then calcined in air at 550 °C overnight. The amount of incorporated aluminum was analyzed by ICP-AES.

SBA-15 supported cobalt catalysts were prepared by three different cobalt impregnation methods: incipient wetness, post-synthesis and supercritical solvent. The cobalt post-synthesis impregnation was similar to that used to graft aluminum on SBA-15. The impregnation of the SBA-15 with cobalt using a supercritical solvent proceeded as follows: The SBA-15 was added to a 250 mL ethanol solution of Co(NO₃)₂ · 6H₂O, and stirred at ambient temperature for 1 h. The suspension was transferred to an autoclave placed inside a furnace. The autoclave was purged ten times with 200 psi N₂ to remove any oxygen trapped in the system. The autoclave was heated to 350 °C at 5 °C/min, then held at 350 °C for 3h. The pressure inside the autoclave was maintained at 2000 psi by controlled venting through a high-pressure valve. The system was cooled to 200 °C, and the gas inside the autoclave was

Table 1. Specifications of SBA-15 supported cobalt and iron catalysts.

Catalyst	Silica	Precursor	Co loading (Wt %)	Loading method
CAT1	SBA15	Co(NO ₃) ₂	6	IW
CAT2	SBA-15	Co(ac) ₂ ^b	6	PS
CAT3	SBA-15	Co(NO ₃) ₂	6	SS
CAT4	SBA-15	Co(NO ₃) ₂	20	IW
CAT5	SBA-15	Fe(NO ₃) ₃	20	IW
CAT6	AlSBA-15	Fe(NO ₃) ₃	20	IW

^a IW: incipient wetness, PS: post synthesis, SS: Supercritical solvent

^b Co(ac)₂ is anhydrous cobalt acetate

vented for 1 h. The system was then cooled to ambient temperature. The cobalt impregnated sample was calcined in air at 550 °C overnight. In this study, iron impregnated SBA-15 samples were prepared by incipient wetness impregnation using Fe(NO₃)₃·9H₂O dissolved in ethanol solution. All calcined samples were reduced under hydrogen at 500 °C for 10 h to obtain active metallic cobalt or iron for the FT synthesis. Specifications of SBA-15 supported cobalt and iron catalysts used in this study are shown in Table 1.

Catalyst characterization. To evaluate the pore structure of the catalyst samples, nitrogen adsorption isotherms were measured using an Autosorb-1 instrument (Quantachrom). The isotherms were used to calculate the BET specific surface area (S), total pore volume (V_t), and average pore diameter (D_p). The pore structure of the samples was also evaluated using XRD patterns. The reduction of cobalt oxides in the sample was evaluated by temperature programmed reduction (TPR, Micromeritics). The H₂ consumption of the sample was calculated using the reduction of CuO as the standard.

FT synthesis and product analysis. The FT synthesis was carried out in a fixed-bed stainless steel reactor (5 mm I.D. and 168 mm length) at 100 psi and 265 °C. An H₂/CO molar ratio of 2 was used, and a ratio of sample weight to total gas flow rate (W/F) was 0.47 - 0.91. The gas flow rates for reactant gases (CO, H₂) and internal standard (Ar) were controlled by mass flow controllers (MKS). Iron carbonyl impurities in the CO reactant stream were removed by a PbO₂/Al₂O₃ trap. The test for the FT synthesis was carried out for 36 h on stream. Reactants and hydrocarbon products were analyzed by gas chromatography (Shimadzu). The GC oven was heated using a heating program as follows: 10 °C for 4 min, then heating from 10 to 350 °C with the heating rate of 20 °C/min and holding at 350 °C for 10 min. Reactants were separated on a capillary column (CarboPlot, 0.53 mm I.D. and 30 m length) with a TCD detector. Hydrocarbon products were separated on a capillary column (DB-5, 0.25 mm I.D. and 10 m length) with an FID detector.

Results and Discussion

The results of XRD patterns and nitrogen adsorption/desorption isotherms revealed that all cobalt catalysts having 6 wt% cobalt had the 2-D hexagonal structure of pure SBA-15. Pore structural parameters calculated from nitrogen adsorption/desorption isotherms for the cobalt SBA-15 catalysts are listed in Table 2. The BET surface area, pore volume and pore diameter of SBA-15 are decreased by cobalt impregnation. However, the three cobalt catalysts prepared by three different impregnation methods have similar pore structural values. This implies that the impregnation method does not have a significant impact on the pore structure of SBA-15.

Table 2. Physical and chemical properties of SBA-15 supported cobalt catalysts.

Catalyst	S ^a (m ² /g)	V _t ^b (cc/g)	D _p ^c (nm)	Co ₃ O ₄ ^d Diameter (nm)	Reduction ^e (%)
Pure SBA-15	724	1.243	8.09	-	-
CAT1	465	0.811	8.08	11.1	49
CAT2	472	0.858	8.08	-	18
CAT3	461	0.815	8.08	11.6	63

^a BET Surface area, ^b Total pore volume, ^c average pore diameter,

^d Co₃O₄ crystallite diameter calculated from the widths of XRD peaks using the Scherrer equation ($2\theta = 36.68^\circ$), ^e reduction degree of cobalt oxides during TPR at 30 – 500 °C.

The mean Co₃O₄ crystallite sizes deduced from the XRD data using the Scherrer equation and the reduction percentage of the cobalt oxides at temperatures less than 500 °C are presented in Table 2. The XRD peak at 36.68° for CAT2 was not detected. This suggests that most of cobalt oxides are present as cobalt silicates in the framework of the SBA-15, and the average crystallite size of Co₃O₄ on the surface of the SBA-15 is very small. The mean Co₃O₄ crystallite size on CAT3 is slightly larger than on CAT1. This result indicates that the crystallite size of Co₃O₄ is clearly dependent on the impregnation method.

Figure 1 shows TPR profiles of three cobalt catalysts, CAT1, CAT2 and CAT3. CAT1 and CAT3 show similar TPR profiles with three typical peaks. However, the TPR profile of CAT2 with two peaks is significantly different. For CAT1 and CAT3, the first peak at temperatures less than 380 °C can be assigned to the reduction of Co₃O₄, and the second peak in the 380 - 600 °C range corresponds to the reduction of cobalt oxides strongly interacting with the SBA-15. The third peak in the 600 - 760 °C range can be attributed to the reduction of cobalt oxides very strongly interacting with the SBA-15. The maximum temperatures of the three peaks for CAT3 are located at lower temperatures than for CAT1. In particular, the intensity of the third peak for CAT3 is very low. This suggests that highly irreducible cobalt oxides on CAT3 are less prevalent

than on CAT1. CAT2 shows two peaks in its TPR profile. The first peak is at temperatures in the range of 200 – 500 °C, and the second peak is located at temperatures above 760 °C, corresponding to the reduction of cobalt oxides in the framework of SBA-15. The reduction percentage of the cobalt oxides at temperatures less than 500 °C are presented in Table 2. CAT3 shows the highest reducibility of cobalt oxides among the

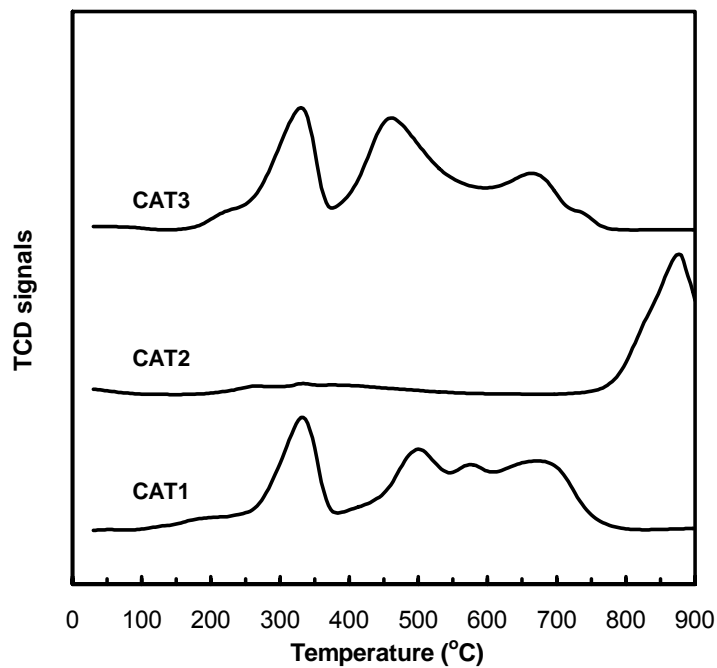


Fig.1 TPR profiles of three cobalt catalysts

three catalysts prepared by different impregnation methods. According to the TPR results, undesirable cobalt oxides (those not easily converted to active cobalt metal at lower temperature) were abundantly produced in CAT1. Catalytic activities of SBA-15 supported cobalt and iron catalysts in FT synthesis are summarized in Table 3.

Table 3. CO conversion, hydrocarbon selectivity and chain growth probability of SBA-15 supported cobalt and iron catalysts

Catalyst	W/F (g h/mol)	CO conversion (%)	Product selectivity (C mol%)				^a
			C ₁	C ₂ -C ₄	C ₅ -C ₁₀	C ₁₀ +	
CAT1	0.73	15.7	8.6	38.6	39.0	13.8	0.86
CAT2	0.91	4.6	15.8	56.8	24.2	3.2	0.82
CAT3	0.67	21.1	7.3	32.4	45.3	15.0	0.88
CAT4	0.55	22.2	7.2	32.3	46.5	14.0	0.88
CAT5	0.47	23.8	6.2	6.5	32.8	54.5	0.95
CAT6	0.47	32.5	4.9	6.1	27.3	61.7	0.98

^a chain growth probability obtained from Anderson-Schulz-Flory equation

CO conversion and higher hydrocarbon selectivity can be related to the reducibility of the cobalt oxides and pore structure of a cobalt catalyst. The three samples (CAT1, CAT2, CAT3) having the same loading of cobalt showed similar values in BET surface area, pore volume and average pore size. However, the three samples showed differences in the reducibility of cobalt oxides. CAT3 shows the highest CO conversion, C₅₊ selectivity and chain growth probability among the three catalysts obtained by three different cobalt impregnation methods. This result is quite consistent with the TPR result.

In this study, to investigate the effect of active metal and aluminum incorporation of SBA-15 on catalytic activity, we prepared a cobalt catalyst (CAT4) and two iron catalysts (CAT5, CAT6). The three samples have the same metal loading. CAT5 shows higher CO conversion, C₅₊ selectivity and chain growth probability than CAT4. This indicates that iron in the SBA-15 is more effective than cobalt for FT synthesis.

As the results of TPR and EXAFS tests, after aluminum incorporation of SBA-15, reducible iron oxides such as Fe₂O₃ on CAT6 were greatly increased compared to CAT5. This indicates that the increase of reducible iron oxides leads to an increase in catalytic activity of the iron catalyst.

Conclusions

The cobalt impregnation method has a significant effect on catalytic activity and selectivity through differences in reducibility of cobalt oxides. Aluminum added iron-based catalyst is also advantageous.

References

1. J.S. Girardon, A.S. Lermontov, L. Gengembre, P.A. Chernavskii, A. Griboval-Constant and A.Y. Khodakov, *J. Catal.*, **2005**, 230, 339-352.
2. K. Okabe, M. Wei and H. Arakawa, *Energy & Fuels*, **2003**, 17, 822-828.
3. A. Martinez, C. Lopez, F. Marquez and I. Diaz, *J. Catal.*, **2003**, 220, 486-499.
4. J. Panpranot, J. G. Goodwin Jr. and A. Sayari, *Catal. Today*, **2002**, 77, 269-284
5. Y. Wang, M. Noguchi, Y. Takahashi and Y. Ohtsuka, *Catal. Today*, 2001, **68**, 3-9.
6. D. J. Kim, B. C. Dunn, P. Cole, G. Turpin, R. D. Ernst, R. J. Pugmire, M. Kang, J. M. Kim, and E. M. Eyring, *Chem. Commun.*, **2005**, 1462-1464.
7. J. M. Kim and G. D. Stucky, *Chem. Commun.*, **2000**, 1159-1160.

Gas-Phase Incorporation of Organometallic Compounds within Aerogels for Synthesis of Fischer-Tropsch and Water-Gas Shift Catalysts

October 1, 2004 – March 31, 2005

Gregory C. Turpin, Yifan Shi, and Richard D. Ernst

Department of Chemistry, University of Utah, Salt Lake City, Utah 84112

I. Introduction

The Fischer-Tropsch and Water Gas Shift reactions each offer the potential for providing solutions to important future energy concerns. In each case, catalysts employed for these processes tend to be late transition metals deposited on typical supports such as silica, alumina, or titania. While numerous studies have addressed the roles played by various catalyst and support combinations, far less attention has been devoted to studies involving aerogel supports, whose highly porous natures should promote more effective catalyst dispersal and enhanced mass transport of reactant and product molecules through the aerogel pores.¹ Additionally, catalytic studies utilizing aerogel supports may be carried out either under gas-phase or supercritical conditions, leading to additional control over the nature of the reaction.²

The unique structures and properties of aerogels allow for the preparation of very new catalyst/support motifs. In one application, the highly porous aerogel backbone can serve as a framework onto which a more desirable support material may be deposited. This approach could be advantageous in cases in which the more desirable support either may be costly, or does not form a reasonable aerogel structure on its own. As will be described, this approach has been successfully applied to the preparation of a ceria-coated silica aerogel. A second opportunity for aerogels relates to the catalyst incorporation step. Since partial wetting of an aerogel structure can lead to drastic collapse of the pore structure, gas phase incorporation processes could offer some advantages, including the potential of effecting single site metal incorporation and of delivering one metal selectively to another on the support surface.

II. Experimental

Catalyst Supports. Silica aerogels were prepared as previously described.³ Solution phase loading of cerium(IV) alkoxides⁴ was accomplished by first replacing the solvents in a 10 mL solid monolithic alcogel sample through 4-5 equilibrations with 20-25 mL volumes of THF, after which the external solvent was replaced by a solution of the cerium alkoxide in THF. Subsequent equilibration led to an even distribution of cerium throughout the entire solution volume, within and outside of the alcogel. The alcogel monolith was then removed and subjected to two similar equilibrations with acetone, after which the monolith was placed in a CO₂ atmosphere, pressurized to supercritical conditions, and dried to yield the aerogel.

Catalyst Preparations. The metal pentadienyl compounds were prepared according to literature methods,⁵⁻⁷ as were the cobalt catalyst precursors.^{8,9} For gas phase incorporations of the transition metal complexes, the appropriate masses of organometallic compound and crushed aerogel were combined under nitrogen in a Schlenk tube which was then placed under static vacuum and rotated constantly until the separate organometallic phase was no longer visible. Oxygen gas was then passed over the doped aerogel, beginning at 25 °C, with the temperature

thereafter slowly brought to 25-300 °C, depending on sample. Subsequently, the supported metal oxide was heated to 500 °C, and reduced in a hydrogen stream.

Catalytic Studies. Fischer-Tropsch reactions were carried out in a laboratory-scale packed bed reactor, as previously described,³ except that C₁-C₁₃ hydrocarbon products were analyzed by gas chromatography on a capillary column (DB-5, 0.53 mm I.D. and 30 m length) with an FID.

III. Results and Discussion

In the last year, a substantial backlog of catalysts to be tested has developed. Some effort, particularly by Dr. Brian Dunn, has therefore been expended to remove a GC/MS analyzer and make modifications to allow for simultaneous monitoring of up to six reactors, which should greatly facilitate our future studies. Some significant progress has been achieved over the past 6 months. Together with the Eyring and Pugmire groups, a number of zeolite-supported Fischer-Tropsch (FT) catalysts have been studied, and a publication of some of the results has recently appeared.

Further reactivity studies of aerogel-supported cobalt and ruthenium FT catalysts have been carried out. For the most part, these data continue the trends seen in the preliminary results described in last year's report. One especially intriguing result has been obtained, however, for a 2% ruthenium catalyst. While our other ruthenium catalysts were air-oxidized, subsequently calcined at ca. 350 °C, and thereafter reduced by hydrogen, the most recent sample was simply air-oxidized at room temperature, and then reduced. Unlike all of our other ruthenium and cobalt catalysts, which did not show an induction period prior to the onset of activity, this one at first was nearly inactive, but after ca. 16 hours, its activity began to increase, and by ca. 30 hours, it had become even more active than our previous 10% ruthenium catalyst (see Fig. 1). It could be that by avoiding the high temperature calcinations process, the extent of ruthenium aggregation

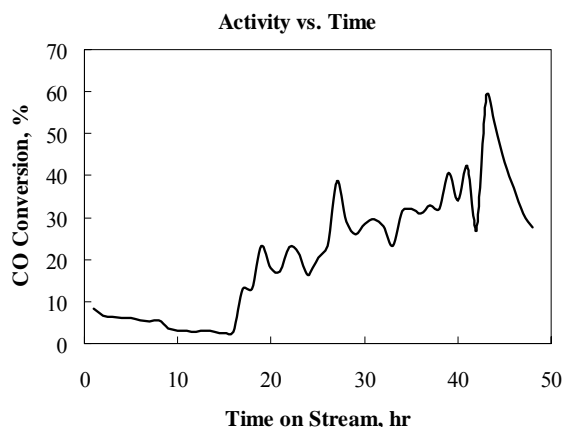


Fig. 1. Dependence of activity with time for an unusual ruthenium catalyst.

was reduced, leading initially to a lower activity catalyst, but with time agglomeration might have taken place to yield a more optimal metal distribution than obtained via higher temperature calcination. Clearly this preliminary result needs to be checked for reproducibility, and appropriate microscopic studies should help establish the natures of the metal particles at the key stages of preparation and use. If this preliminary observation holds up, it will clearly impact significantly on our future studies with hydrogen. It has also been observed that the initially

incorporated ruthenium reacts directly with hydrogen, which provides another alternative to calcination.

While we have developed a gas-phase "redox targeting" approach that appears to selectively deliver cobalt to supported ruthenium on an aerogel surface (described in our last yearly report), it was also of interest to devise a strategy for achieving this via solution methods. A number of other groups have studied a variety of mixed Co/Ru carbonyl complexes, which can be incorporated via gas or solution phase methods, but the carbonyls clearly have cost and convenience issues. We have therefore turned our attention to the utilization of pyridazine (**1**) and pyrazole (**2**), as ligands with the potential to link cobalt and ruthenium. One possibly useful



result has been obtained, from the reaction of pyridazine with (1,5-COD)RuCl₂ (readily obtained from commercial "RuCl₃ hydrate" with 1,5-cyclooctadiene¹⁰). In the presence of H₂, the COD ligand is hydrogenated to cyclooctane, and rather surprisingly, six pyridazines coordinate to the ruthenium center, giving [Ru(1,2-C₄N₂H₄)₆]²⁺ (Fig. 2). Previously, no more than three pyridazines could be incorporated into a ruthenium complex. Further work to attach cobalt to the uncoordinated ends of the pyridazines is underway.

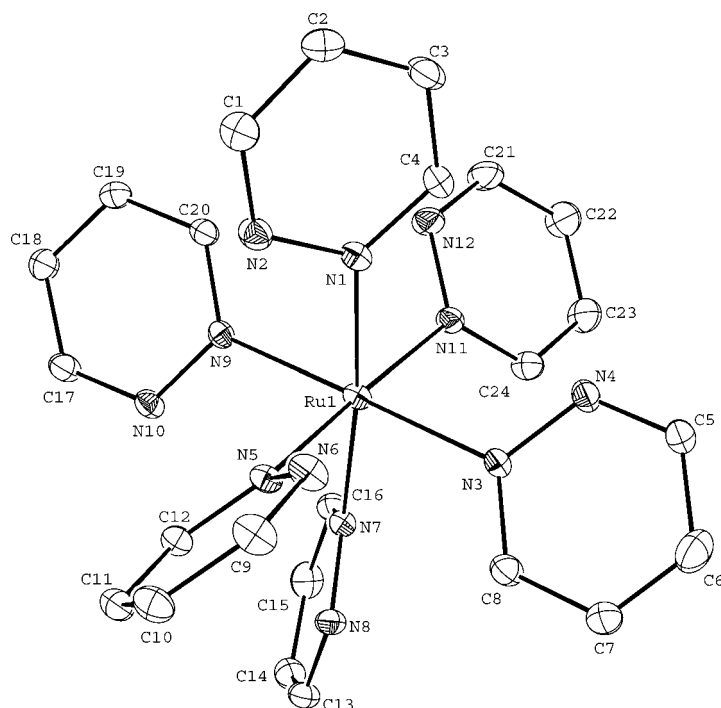


Fig. 2. Structure of the [Ru(1,2-C₄N₂H₄)₆]²⁺ complex.

Chris Roberts' group has completed a gas phase study of one of our 10% ruthenium on aerogel catalysts, as a comparison to the results they obtained previously under supercritical conditions. As opposed to their results with cobalt, the gas phase FT reaction for ruthenium appears superior to reaction under supercritical conditions. Particularly interesting was that in some cases, the isoparaffin content exceeded the n-olefin content.

Jim Guin's group has studied cyclohexane dehydrogenation on SBA-15 catalysts onto which 1% ruthenium had been incorporated via gas-phase deposition. The catalysts showed significant activity, though not nearly to the extent as 1% Pt. Of course, ruthenium is much less expensive; furthermore, the ruthenium catalyst had undergone high temperature calcinations, and the preliminary result described above for a 2% FT catalyst prepared without high temperature calcinations suggests that better dehydrogenation activity might be obtained without the high temperature calcination. Additionally, it would be of interest to incorporate palladium and platinum via gas-phase deposition, which should yield a more dispersed catalyst.

Studies of the Water Gas Shift (WGS) Reaction. Copper, gold, and palladium catalysts supported on ceria have recently been reported to yield very active catalysts for the WGS reaction.^{11,12} One of our goals from the 2003-2004 yearly report was therefore to develop a means to prepare the equivalent of a ceria aerogel, whose large pores and surface area should offer substantial advantages as a support. Unfortunately, ceria aerogels undergo collapse at higher temperatures.¹³ Hence, it was of interest to see if silica aerogel could be used as the equivalent of a scaffold on which ceria could be deposited, yielding the equivalent of a more robust ceria aerogel. This approach not only would yield a stronger, yet still highly porous support structure, it would also reduce the amount of the more expensive ceria required for a given amount of support.

Indeed, we have found that the very hydrolytically sensitive $\text{Ce}(\text{O}-i\text{-C}_3\text{H}_7)_4(i\text{-C}_3\text{H}_7\text{OH})$ seems to incorporate very well, to at least 10%, into silica aerogels via standard solution methods. This sample will be sent out for BET measurements shortly. Now that ceria-containing aerogels have been accessed, this should ensure our ability, with the Eyring and Pugmire groups, to explore and exploit the advantages offered by aerogel supports for the WGS reaction. Initially, gold-derived catalysts will be prepared by solution-phase incorporation, while palladium will be incorporated via the gas phase using $\text{Pd}(\text{C}_3\text{H}_5)_2$ ¹⁴ or $\text{Pd}(\text{C}_5\text{H}_5)(\text{C}_3\text{H}_5)$.¹⁵

IV. Conclusions

The high surface areas and highly porous nature of aerogels offer promise not just for the FT reaction, but also WGS and certainly others as well. The use of gas phase approaches likely to generate catalyst centers in very highly dispersed form, whether for aerogels, zeolites, or some other support. It also appears that a silica aerogel structure can be of value in providing a robust framework onto which more fragile species such as ceria can be anchored.

V. Papers Presented or Published

1. "Silica Aerogel Supported Catalysts for Fischer-Tropsch Synthesis," Dunn, B.C.; Cole, P.; Covington, D.J.; Webster, M.C.; Pugmire, R.J.; Ernst, R.D.; Eyring, E.M.; Shah, N.; Huffman, G.P. *Appl. Catal. A* **2005**, 278, 233-238.
2. "Silica Xerogel Supported Cobalt Metal Fischer-Tropsch Catalysts for Syngas to Diesel Range Fuel Conversion," Dunn, B.C.; Covington, D.J.; Cole, P.; Pugmire, R.J.; Muezeelaar, H.L.C.; Ernst, R.D.; Heider, E.C.; Eyring, E.M.; Shah, N.; Huffman, G.P.; Seehra, M.S.; Manivannan, A.; Dutta, P. *Energy & Fuels* **2004**, 18, 1519-1521.

3. "Enhancement in Reducibility of Cobalt Oxides and Catalytic Activity of a Mesoporous Silica Supported Cobalt Catalyst by Silylation," Kim, D.J.; Dunn, B.C.; Cole, P.; Turpin, G.C.; Ernst, R.D.; Pugmire, R.J.; Kang, M.; Kim, J.M.; Eyring, E.M. *J. Chem. Soc., Chem. Commun.* **2005**, 1462-1464.
4. "Use of Organometallic Compounds for the Synthesis of Fischer-Tropsch Catalysts," Turpin, G.C.; Dunn, B.C.; Ma, Z.; Pugmire, R.J.; Eyring, E.M.; Ernst, R.D. Poster, Gordon Research Conference (Hydrocarbon Resources), January 9-14, 2005, Ventura, CA.

VI. Future Work

In addition to completing our comparisons of FT activities for cobalt, ruthenium, and mixed cobalt/ruthenium catalysts incorporated via gas-phase deposition, the potentially important influence of calcination on catalyst activity needs to be elucidated, both through further catalytic studies and microscopy, the latter with Naresh Shah, Frank Huggins, and Jerry Huffman. Additional collaborative studies with the Roberts and Guin groups on FT and cyclohexane dehydrogenation would seem of value. The recent success in loading ceria on a silica aerogel framework will be followed with the Eyring and Pugmire groups. In particular, the physical properties of these composites need to be studied, as well as the incorporation of gold and palladium into the composites, which will then be examined for activity in the WGS reaction.

VII. References

- (1) Husing, N.; Schubert, U. *Angew. Chem. Int. Ed.* **1998**, *37*, 22-45.
- (2) Elbashir, N.O.; Roberts, C.B. *Ind. Eng. Chem. Res.* **2005**, *44*, 505-521.
- (3) Dunn, B.C.; Cole, P.; Turpin, G.C.; Ma, Z.; Pugmire, R.J.; Ernst, R.D.; Eyring, E.M.; Shah, N.; Huffman, G.P. Preprints of Symposia - American Chemical Society, Division of Fuel Chemistry **2004**, *449(1)*, 329-330.
- (4) Vaartstra, B.A.; Huffman, J.C.; Gradeff, P.S.; Hubert-Pfalzgraf, L.G.; Daran, J.-C.; Parraud, S.; Yunlu, K.; Caulton, K.G. *Inorg. Chem.* **1990**, *29*, 3126-3131.
- (5) Wilson, D.R.; Stahl, L.; Ernst, R.D. *Organometallic Syntheses* **1986**, *3*, 136.
- (6) Elschenbroich, C.; Bilger, E.; Ernst, R.D.; Wilson, D.R.; Kralik, M.S. *Organometallics* **1985**, *4*, 136.
- (7) Gleiter, R.; Hyla-Kryspin, I.; Ziegler, M.L.; Sergeson, G.; Green, J.C.; Stahl, L.; Ernst, R.D. *Organometallics* **1989**, *8*, 298.
- (8) Otsuka, S.; Rossi, M. *J. Chem. Soc. A.* **1968**, 2630.
- (9) Eisch, J.J.; King, R.B. *Organometallic Syntheses* **1965**, *1*, 70.
- (10) Albers, M.O.; Ashworth, T.V.; Oosthuizen, E.; Singleton, E. *Inorg. Syn.* **1989**, *26*, 68-69.
- (11) Fu, Q.; Saltsburg, H.; Flytzani-Stephanopoulos, M. *Science* **2003**, *301*, 935-938.
- (12) Qi, X.; Flytzani-Stephanopoulos, M. *Ind. Eng. Chem. Res.* **2004**, *43*, 3055-3062.
- (13) Thundathil, M.A.; Lai, W.; Noailles, L.; Dunn, B.S.; Haile, S.M. *J. Am. Ceram. Soc.* **2004**, *87*, 1442-1445.
- (14) Krause, J.; Bonrath, W.; Porschke, K.R. *Organometallics* **1992**, *11*, 1158-1167.
- (15) Tatsuno, Y.; Yoshida, T.; Otsuka, S. *Inorg. Syn.* **1979**, *19*, 220-223.

STABILITY AND STRUCTURE OF COBALT CATALYTIC SYSTEMS IN FISCHER-TROPSCH SYNTHESIS: SUPERCRITICAL FLUID MEDIA VERSUS CONVENTIONAL GAS-PHASE MEDIA

N. O. Elbashir^a, C. B. Roberts^a

^aDepartment of Chemical Engineering, Auburn University, AL 36849,

P. Dutta^b, M. S. Seehra^b,

^bPhysics Department, West Virginia University, Morgantown, WV 26506

1. Introduction

The limitations of the conventional media (gas-phase and liquid-phase) for Fischer-Tropsch synthesis (FTS) have driven research towards the application of supercritical fluid (SCF) solvents. The objective is to improve product control in the liquid fuels range and provide an opportunity for selective control of hydrocarbon distribution. The advantages of utilizing SCF solvents in the FTS reaction can be attributed to the fact that they offer high diffusivities (relative to a liquid phase FTS) and high solubilities and improved heat transfer (relative to a gas phase FTS). Utilization of cobalt-based catalysts in the FTS is known to provide the best compromise between performance and cost for the synthesis of hydrocarbons from syngas. Cobalt catalysts were also found to give the highest yields and longest lifetime producing mainly linear alkanes (paraffins)¹. Since cobalt catalysts are not inhibited by the water-gas-shift (WGS), they give high productivity at high syngas conversion². The efficiency of the synthesis process is critically dependent on the effectiveness and the stability of the cobalt catalyst. Most of the industrial cobalt-based systems used in the FTS reaction are either alumina supported or silica supported catalysts. Therefore, cobalt dispersion on the supported catalyst surface³ and the interaction of the Co with the metal oxide support (which affects the electronic density as well as the structure of the metal crystallites⁴) are assumed to play significant roles in the catalyst performance measured by the hydrocarbon selectivity (C₅₊) and the catalyst activity.

The stability of the cobalt catalyst structure represents a major challenge to commercial-scale plants. The catalyst cost in addition to its regeneration cost represents a considerable proportion of the overall process cost. In many cases the cost of regenerating the catalyst is more expensive than the fresh catalyst cost⁵. Deactivation of the catalyst was assumed to be due to carbonaceous formations (specifically crystalline carbides) in the catalyst surface⁶, and also as a result of re-oxidation by the by-product water⁷.

Several techniques (XRD, magnetization, and electron magnetic resonance) were used to characterize our catalysts to determine the surface structure of the catalyst and the electronic states (Co⁰, CoO, Co₃O₄, Co²⁺) before and after the reaction. Our objective is to study the sensitivity of the supported-cobalt catalyst structure (physico-chemical characteristics, oxidation states, and crystalline structure of the active phase) during the FTS reaction. In general, it has been shown that supercritical phase FTS results in better catalyst stability at long time-on-stream (TOS) compared to conventional gas-phase FTS.

2. Experimental

2.1 Catalysts. Three catalytic systems were tested under both conventional gas-phase and supercritical phase FTS (15% Co/SiO₂ HSA supported on high surface area silica, 15% Co/SiO₂ LSA supported on high surface area silica, and 15% Co/Al₂O₃). The two silica supported catalysts were prepared in our lab⁸. The alumina catalyst is a commercial catalyst purchased from United Catalyst Co. The silica supported catalysts were reduced in hydrogen environment, while the alumina supported catalyst was reduced in carbon monoxide environment.

2.2 Catalyst Characterizations. Room temperature X-ray diffraction (XRD) patterns of these catalysts were obtained with a Rigaku diffractometer using CuK_α radiation with $\lambda = 0.15418$ nm. Measurements of magnetization M versus temperature T and magnetic field H were done with a commercial SQUID (superconducting quantum interference devices) magnetometer. Electron magnetic resonance (EMR) studies were carried out at the X-band frequency of 9.278 GHz with a variable temperature cryostat from Oxford Instruments. In this system, the microwave cavity remains at room temperature whereas the sample temperature can be varied from 4 K to 300 K. In the EMR resonance condition $h\nu = g\mu_B H_0$, the microwave frequency ν is accurately measured by a frequency counter and the resonance field H_0 by a NMR probe. The magnetic field is modulated at 100 kHz so that the experimental traces represent dP/dH versus H , with P being the power absorbed. The back ground for the magnetic theory and the interpretation of the magnetic data was discussed in some detail in our previous study⁸.

2.3 Fischer-Tropsch Studies. The FTS reaction was carried out in a high-pressure FTS unit. A detailed description of this unit has been given elsewhere⁹. Hexanes (HPLC grade purchased from Fishers Co.) was used as the solvent for the supercritical phase FTS studies. The molar ratio between hexanes/syngas was kept at 3/1 whereby the syngas ($H_2/CO = 1$) flows was at a rate of 50 sccm/g_{cat}. In this study we referred to the supercritical hexanes FTS experiments as SCH-FTS.

Analysis of reactants and products was carried out by two online GCs. The results from the two GCs were used for conversion and selectivity calculations. A Varian 3300 GC with capillary column (DB-5) and a FID detector was used for the analysis of C₂-C₄₀ hydrocarbons and oxygenates. Analysis of permanent gases (H₂, CO, N₂, CH₄, CO₂, C₂H₄, and C₂H₆) was conducted by a Varian CP-3800 GC with a packed column (Hayesep-DB100/120) and TCD detector. The online injection of our samples to the two GCs was carried out by two automated six-way-valves. Quantitative analysis of the results from the Varian CP-3800 provided the necessary data for the calculations. Reactants conversion (CO conversion and H₂+CO (syngas) conversion), CH₄ selectivity, CO₂ selectivity, and C₂ (ethane and ethylene) selectivities were calculated using the response factor of N₂ from the TCD analysis as a reference. On the other hand, hydrocarbon product distributions (i.e. C₂ to C₃₀ selectivity data) were determined from the FID and TCD analysis as described in detail elsewhere⁹.

3. Results and Discussion

Table 1 shows a summary of our catalyst XRD and EMR characterizations before (fresh calcined catalyst) and after the reaction (used catalyst after either conventional gas-phase FTS or SCH-FTS). Detailed discussions on the characteristics of fresh catalyst were given elsewhere⁸. Summarizing the results of Table1, we conclude that the LSA 15% Co/SiO₂ used sample (under

gas-phase FTS condition) contains Co^0 only which is the product of the reduction of Co_3O_4 in the calcined unused sample. In the HSA 15% Co/SiO_2 used sample under (SCH-FTS conditions), we observed Co^0/CoO composite, the quantity of CoO being much less than that of Co^0 . Thus either the reduction of Co_3O_4 to Co^0 is not complete since some CoO is observed or some oxidation of Co^0 to CoO has taken place subsequent to the FTS experiments because of the high surface area of the catalysts.

Table 1. Summary of the XRD and EMR characterization of the used cobalt-based catalytic systems under both gas-phase FTS and SCH-FTS.

	XRD & EMR Characterizations	
	Fresh	Used
<u>Silica Catalysts</u>		
HAS 15% Co/SiO_2 (Used 10 days in gas-phase)	$\text{SiO}_2, \text{Co}_3\text{O}_4$	SiO_2 (quartz, cristobalite, tridymite)
LSA 15% Co/SiO_2 (Used 13 days in SCH-FTS)	$\text{SiO}_2, \text{Co}_3\text{O}_4,$ Co^{2+}	fcc- $\text{Co}^0, \text{CoO}, \text{Co}_3\text{O}_4$ (small) SiO_2 (cristobalite)
<u>Alumina Catalysts</u>		
15% $\text{Co}/\text{Al}_2\text{O}_3$ (Unused, reduced catalyst)	$\text{Co}_3\text{O}_4; \gamma\text{-Al}_2\text{O}_3$ $\epsilon\text{-Al}_2\text{O}_3$ $\text{CoO}, \text{hcp Co}^0$	—
15% $\text{Co}/\text{Al}_2\text{O}_3$ (Used 13 days in SCH-FTS)	$\text{Co}_3\text{O}_4, \delta\text{-Al}_2\text{O}_3,$ Co^{2+}	hcp- $\text{Co}^0, \text{CoO}, \text{Co}_3\text{O}_4;$ $\gamma\text{-Al}_2\text{O}_3, \epsilon\text{-Al}_2\text{O}_3$
15% $\text{Co}/\text{Al}_2\text{O}_3$ (Used 7 days in gas-phase-FTS)	$\text{Co}_3\text{O}_4, \delta\text{-Al}_2\text{O}_3,$ Co^{2+}	hcp- $\text{Co}^0, \text{fcc-Co}^0;$ $\gamma\text{-Al}_2\text{O}_3$

Three samples of the alumina supported catalysts were characterized; (1) unused 15% $\text{Co}/\text{Al}_2\text{O}_3$ which was reduced in CO environment.; (2) used sample of 15% $\text{Co}/\text{Al}_2\text{O}_3$ after SCH-FTS condition for 13 days; (3) used sample of 15% $\text{Co}/\text{Al}_2\text{O}_3$ after gas-phase FTS for 7 days for temperatures up to 260°C. Partial reduction of the alumina supported catalyst in CO environment (the unused sample) prior to in situ reduction with the syngas during FTS allows us an opportunity to evaluate the extent of in situ reduction. Our XRD characterization of the unused alumina catalyst showed two Al_2O_3 phases and Co_3O_4 with only a hint of the presence of the hexagonal-close-packed (hcp) phase of Co^0 . For the used sample after supercritical phase operation the characterizations show presence of some CoO and hcp Co^0 and absence of Co_3O_4 . Thus reduction of Co_3O_4 to CoO and hcp Co^0 has occurred. For the used sample from gas-phase FTS both fcc Co^0 and hcp Co^0 are present. Thus the reduction of Co_3O_4 to Co^0 is complete for that sample. The particle sizes of Co^0 determined from the width of the XRD peaks are 13 nm for fcc Co^0 and 14 nm for hcp Co^0 .

Figs. 1 and 2 show an example of stability tests on the alumina-supported catalyst (15% Co/Al₂O₃) under different reaction conditions in the SCH-FTS and gas phase-FTS reactions at relatively long TOS. Syngas conversion is used to represent the activity of the catalyst. During the SCH-FTS testing, the catalyst showed good stability in syngas conversion (~ 80%) at 240 °C and 60 bar. The temperature was then decreased to 230 °C, while the pressure was kept constant at 60 bar. As a result, syngas conversion decreased to ~58%. A stable trend was observed under these conditions for more than 48 hrs TOS. The stability test was then followed by increasing the temperature to 250 °C and the pressure to 65 bar. At these conditions, syngas conversion reaches its highest level, 93%, at the initial 2 hrs TOS and then declined to ~87% for more than 100 hrs TOS. The aforementioned conditions were selected based on our previous investigations of the alumina-supported catalyst, whereby an optimum performance in both activity and selectivity was observed⁹. Upon returning to the initial conditions (240 °C and 60 bar), no significant changes in either syngas conversions was observed as shown in Fig.1.

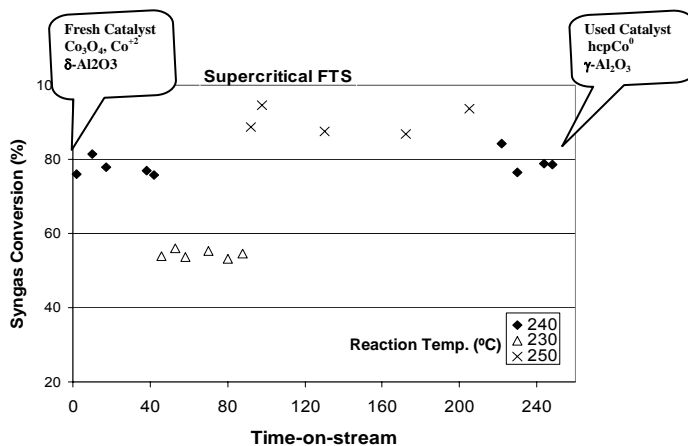


Figure 1. Stability of the 15% Co/Al₂O₃ catalyst activity (syngas conversion (%)) with TOS in SCH-FTS at different reaction conditions (240 °C and 60 bar; 230 °C and 60 bar; 250 °C and 65 bar; and 240 °C and 60 bar). P_{syngas} = 20 bar, syngas flowrate 50 sccm/g_{cat}, and hexane/syngas molar ratio is 3.

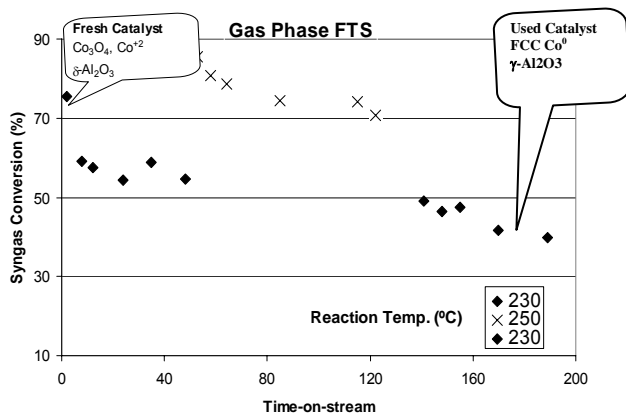


Figure 2. Stability of the 15% Co/Al₂O₃ catalyst activity (syngas conversion (%)) with TOS in gas phase-FTS at different reaction conditions (230 °C and 20 bar; 250 °C and 20 bar; and 230 °C and 20 bar). P_{syngas} = 20 bar, syngas flowrate 50 sccm/g_{cat}.

In the gas phase-FTS (Fig.2), the stability test was initialized at 230 °C and 20 bar for 50 hrs TOS. The catalyst reached a steady value of activity within 10 h of ~59% syngas conversion. Upon increasing the temperature to 250 °C, significant increase in syngas conversion (~88%) was obtained during the first 7 hrs. However, as the TOS was increased (up to 45 h) the syngas conversion decreased to reach 74%. The activity reached a steady value after 70 hrs TOS under the above conditions. Returning to the low temperature conditions (230 °C) resulted in a significant drop (c.a. 25%) in syngas conversion.

In order to understand the role of the reaction media on the catalyst structure and activity we conducted a correlation between the stability tests and the used catalyst characteristics. As discussed earlier our findings show that the dominant cobalt phase of the used sample from SCH-FTS is hcp Co⁰, whereas, the dominant phase in the used sample from gas-phase FTS is fcc Co⁰. It is noteworthy to mention here that the fcc Co⁰ was not detected in the reduced catalyst before the reaction (reduced-unused 15% Co/Al₂O₃). This suggests that the in situ reduction during the SCH-FTS stabilizes the hcp Co⁰ form, which has more surface defects (corners and edges) in the metallic phase than the cubic phase one (fcc Co⁰). In a previous study, Rathousky, et al. stated that the metallic cobalt formed on the outer surface of the CoO crystal-lines enhances the adsorption centers of weakly bonded carbon monoxide molecules¹⁴. Another reason that may contribute to the stability in the catalyst activity in the SCH media is the good temperature distribution inside the fixed-bed-reactor compared to the poor one in the gas-phase media¹⁶. The control of temperature distribution in the reduction process is known to avoid the increase of cobalt-support interactions and agglomerations of cobalt nano-particles¹⁰. Our results shows that there is no significant difference between cobalt particle size of the unused catalyst and that of used catalyst from SCH-FTS (both have size >12 nm)¹⁷. Small particles could easily be reoxidized by water and other reaction conditions during the FTS reaction.

The used silica-supported catalysts showed different characteristics from that of the alumina supported ones. The XRD characterizations of the silica supported catalyst (Table 1) show the presence of quartz, cristobalite, and tridymite silicate forms; however, minimal amounts were detected in SCH-FTS used catalyst. It is also important to mention that no Co⁰, CoO, Co₃O₄ XRD pattern was observed in the used catalyst from the gas-phase where only silicate forms were detected. This suggests that the in situ reduction of the catalyst during the gas-phase FTS is minimal. The presence of the silicate forms in the two used catalysts suggests that the in situ reduction during the FTS reaction is different from that in the alumina-supported catalyst.

4. Conclusions

Our XRD and magnetic characterizations of the used catalysts show that in situ reducibility of the cobalt oxide takes place during the FTS reaction in both gas-phase FTS and SCH-FTS conditions. In the latter, the in situ reduction of Co₃O₄ gave active crystal-lines of hcp and fcc Co⁰ that were found to be very stable for a long TOS. As a result, the activity and selectivity of the catalyst in the SCH medium is more stable and recoverable than that under gas-

phase FTS conditions. Our findings also show that the in situ reduction pathway of the silica supported catalyst is different than that of the alumina supported one; however, a stable form of fcc Co⁰ has also been detected on the used catalyst from the SCH-FTS operation. Detailed discussions on the influence of the catalyst surface characteristics on both the activity and selectivity of the FTS reaction in both gas-phase and SCH phase were covered elsewhere¹⁷.

Acknowledgments. The authors would like to acknowledge the financial support of the Consortium for Fossil Fuel Science (under the Department of Energy Grant DE-FC26-02NT41594) and by Nippon Oil Corporation, Japan (CBR and NOE).

References

- (1) Chaumette, P.; Verdon, C.; Boucot, P. *Topics in Catalysis* **1995**, 2, 301-311.
- (2) Van Berge, P. J.; Everson, R. C. *Studies in Surface Science and Catalysis (Natural Gas Conversion IV)* **1997**, 107, 207-212.
- (3) Tauster, S. J.; Fung, S. C. *J. Catal.* **1978**, 55, 29.
- (4) Iglesia, E.; Soled, S. L.; Fiato, R. A. *J. Catal.* **1992**, 137, 212-224.
- (5) Zhan, X.; Arcuri, K.; Huang, R.; Agee K.; Engman, J.; Robota, H. J. *Prep. Pap.-Am. Chem. Soc., Div. Pet. Chem.* **2004**, 49, 179.
- (6) Gruver, V.; Zhan, X.; Engman, J.; Robota, H. J. *Prep. Pap.-Am. Chem. Soc., Div. Pet. Chem.* **2004**, 49, 192-194.
- (7) Li, J.; Jacobs, G.; Das, T.; Zhang, Y.; Davis, B. *App. Catal. A: Gen.* **2002**, 236, 67-76.
- (8) Dutta, P.; Elbashir, N. O.; Manivannan, A.; Seehra, M. S.; Roberts, C. B. *Catal. Letters* **2004**, 98, 203-210.
- (9) Elbashir, N. O.; Roberts, C. B. *Ind. Eng. Chem. Res.* **2005**, 44, 505-521.
- (10) Khodakov, A. Y.; Griboval-Constant, A.; Bechara, R.; Zholobenko, V. L. *J. Catal.* **2002**, 206, 230-241.
- (11) Iglesia, E.; Reyes, S. C.; Madon, R. J.; Soled, S. L. *Adv. Catal.* **1993**, 39, 221-302.
- (12) Reuel, R. C.; Bartholomew, C. H. *J. Catal.* **1984**, 85, 78-88.
- (13) Elbashir, N. O.; Roberts, C. B. *Prep. Pap.-Am. Chem. Soc., Div. Pet. Chem.* **2004**, 49, 157-160.
- (14) Rathouský, J.; A., Z.; Lapidus, A.; Krylova, A. *App. Catal. A: Gen* **1991**, 79, 167-180.
- (15) Enache, D. I.; Rebours, B.; Roy-Auberger, M.; Revel, R. *J. Catal.* **2002**, 205, 346-353.
- (16) Yokota, K.; Hanakata, Y.; Fujimoto, K. *Chemical Engineering Science* **1990**, 45, 2743-2749.
- (17) Elbashir, N. O.; Dutta, P.; Manivannan, A.; Seehra, M. S.; Roberts, C. B. *App. Catal. A: Gen.* **2005**, in press.

DEVELOPMENT OF MOLYBDENUM-PROMOTED CATALYSTS SUPPORTED ON ACTIVATED CARBON FOR DIESEL FUEL SYNTHESIS

(First Six-Month Progress Report, October 01, 2004 – March 31, 2005)

Wenping Ma, Edwin L. Kugler, James Wright and Dady B. Dadyburjor

Department of Chemical Engineering
West Virginia University
Morgantown, WV 26505-6102

I. Introduction

It is well known that the Fischer-Tropsch Synthesis (FTS) provides an alternative way to convert coal indirectly to transportation fuels. The traditional industrial catalysts used for this reaction are precipitated iron and silicon supported cobalt catalysts, which initially appeared in the FTS plant in Sasol, South Africa and Malaysia [1-2]. These two types of FTS catalysts have been famous for optimal production of high-molecular-weight hydrocarbons, which need to be further treated (by isomerization and hydrocracking) to yield liquid diesel fuels. In order to simplify the conventional FTS technology and to lower the capital cost of the diesel fuels, selective FTS catalysts have been suggested, on which medium-molecular weight hydrocarbons (mainly diesel fuels) expect to be directly formed from syngas [3-4]. Hydrocarbon chain growth can be limited over iron and cobalt catalysts supported on cheap Activated Carbon (AC) and on Carbon Nanotube supports, indicating that carbon material may be a good choice for limiting hydrocarbon chain length to a certain range.

We have been working on AC-supported Mo catalysts since 1991. Mo-Ni/AC catalysts have been successfully used for synthesis of high-molecular-weight alcohols [5, 6]. These studies also demonstrated that AC-supported catalysts are able to produce hydrocarbons with limited carbon numbers, e.g. less than C₆, and that the nature of the activated carbon plays a role in the product distribution. In the present study, we have investigated physico-chemical properties of AC-supported Mo-promoted Fe-Cu-K catalysts as a function of Mo loading (0-12%). The catalysts have been characterized by N₂ adsorption, x-ray diffraction (XRD), temperature-programmed reduction (TPR), CO chemisorption and isothermal reduction. The influence of Mo loading on the degree of reduction of iron, iron dispersion, and the particle size of iron containing active sites are discussed.

II. Experimental

Catalyst Synthesis. The catalysts were prepared as described earlier [7], except that the only support used was activated carbon from peat, as obtained from Sigma Aldrich. The final catalyst contains 0-12% Mo, 15.7 % Fe, 0.8 wt% Cu and 0.9 wt% K. The catalysts were characterized before and after reaction.

BET surface area measurement. The BET surface area and pore volume of the peat-AC support and catalysts before and after FTS reactions were determined by isothermal adsorption of N₂ at 77 K in a Coulter Omnisorp 360 system. Prior to the adsorption measurements, the samples were degassed under vacuum at 300°C for 10 h.

EDS measurement. The supports and catalysts were analyzed by energy-dispersive spectroscopy (EDS) in order to confirm the elements and the relative ratio of iron to carbon on the catalyst surface. The sample was placed on double-stick adhesive tape and placed in the instrument.

XRD measurement. Powder x-ray diffraction (XRD) analysis of the catalysts after reaction was carried out at room temperature using a Rigaku Diffractometer (DMAX-B) and Cu K_α radiation (1.5418 Å). The samples were mounted on a silicon plate for x-ray measurements. The identification of different phases was conducted using Jade software and the ICDD-PDF4 library. The average particle sizes of iron oxide and iron carbide in the different catalysts were estimated by the Scherrer equation using the most intense reflection at $2\theta = 35.5^\circ$ and 43.1° , respectively.

TPR study. Temperature-programmed reduction (TPR) of the catalysts was conducted in a mixture of 5% hydrogen-95% argon at a total flow rate of 50 cm³/min. About 50 mg of the catalyst was placed in a quartz U-tube (5 mm × 300 mm) and heated from room temperature (RT) to 915°C at a constant rate of 10°C/min, and then it was held at 915°C for 30 mins before quenching. The H₂ consumption rate was monitored in a thermal conductivity detector (TCD). The TCD was calibrated previously by reduction of 14 mg of ultra-high purity CuO (99.9999%) between RT and 500°C at the same heating rate. The peak areas in the TPR patterns of the catalysts were deconvoluted using PeakFit software, and the corresponding H₂ consumption at each deconvoluted peak was precisely quantified (H_{exp}). The total theoretical H₂ consumption (H_{tot}) was calculated assuming that Fe and Mo are in the forms of Fe₂O₃ and MoO₃ before reduction, and that they are completely reduced to Fe and Mo metals. Then the degree of reduction of the metal, R_T, corresponding to the deconvoluted TPR peak, can be calculated as:

$$R_T = (H_{\text{exp}}) / (H_{\text{tot}}) \quad (1)$$

CO pulse chemisorption / Isothermal Reduction. CO adsorption behavior on partially reduced catalysts was studied in order to estimate the Fe and Mo metal dispersion on the catalyst surface. About 200 mg of the AC support or catalyst was pretreated at 400°C for 12 hours using 5%H₂ in Ar. After that, the reactor was cooled to room temperature by flowing Ar. CO chemisorption was conducted by injection of 10 μl of CO in a stream of Ar. The quantity of CO not chemisorbed on the catalyst was recorded by a TCD. The injections were continued until CO saturates the surface and peak size does not change with subsequent injections. The number of iron sites on the surface, [Fe_s], was estimated from the CO chemisorbed, [CO], using

$$[\text{CO}] / [\text{Fe}_s] = 2 \quad (2)$$

The dispersion (D) is determined by:

$$D (\%) = 100 * [\text{Fe}_s] / (\text{total number of Fe atoms}) \quad (3)$$

Finally, the chemisorbed sample was reduced at 400°C for 12 h and the amount of hydrogen required for that was determined. The degree of reduction of the metals during this isothermal reduction, R_I , was estimated using Eqn (1).

III. Results and Discussion

BET-based Properties of support and supported catalysts. BET surface areas, total pore volumes, and average pore diameters of the peat-AC support and the catalysts before and after FTS reaction are shown in Table 1. After addition of Fe, Cu and K to the support, the BET surface area of the fresh catalysts is reduced by 42%, and the total pore volume by about 50%. Correspondingly, the average pore diameter of the fresh catalyst is decreased by 30%. Addition of 6 wt% Mo does not further decrease the surface area, pore volume or average pore diameter appreciably. When the catalyst contains 12 wt% Mo, the surface area decreases by another 30%, while the pore volume does not decrease appreciably, but the average pore diameter increases to approximately the value of AC alone. It might be that more micro-pores on the 12 % Mo catalyst are filled or blocked by metal precursors, leading to a relatively greater loss of surface area in comparison with its pore volume and larger average pore diameter.

The decrease in BET surface area and pore volume for the fresh catalysts might arise from two factors. One could be metal precursors filling and blocking a fraction of micro- and meso-pores of the AC support; another could be lower mass concentration of the AC support after impregnation (25-42% less). For the spent catalysts, the BET surface areas of all the catalysts decrease by 95%, and the pore volumes by 40 – 70%, but the average pore diameters increase to 102 -152 Å. This indicates that the pores of the spent catalysts are collapsed partially after FTS and/or some of the FTS products remain in the micro-pores of the catalyst.

EDS. Table 2 gives the EDS results for the AC support and the three fresh catalysts. The catalysts are characterized by slightly higher mole ratios of iron to carbon than the bulk values, and slightly lower amount of Mo, but probably within the range of experimental error. EDS also detects oxygen and trace amounts of Si, Ca and Mg elements on surface of the carbon support.

XRD. Figure 1 shows the patterns of the three spent Fe-Mo-Cu-K/AC catalysts after 72-396 h FTS reaction at 310-320°C. All three catalysts show qualitatively similar XRD patterns between $2\theta = 30^\circ - 80^\circ$. The diffraction peaks match very well with the standard Fe_5C_2 phase and magnetite (Fe_3O_4) phase. This is in good agreement with previous studies on precipitated-iron FTS catalyst [8-10]. Some metallic iron may not be carbonized and may be present on the catalyst surface during reaction. But the current XRD patterns cannot reveal this phase, since the catalyst sample was exposed to air after reaction and any metallic iron would be oxidized.

Figure 1 also shows that the diffraction peaks become smaller and less sharp (particularly at $2\theta = 35.5^\circ$ and 43.8°) when the Mo loading increases. This suggests that the particles of iron oxide and iron carbide become smaller with increasing Mo content. This is quantified by using the Scherrer equation and the results are shown in Table 3. Apparently, the dispersions of Fe_5C_2 and Fe_3O_4 phases on the catalyst are improved after addition of the Mo promoter.

Further, note that the values of the average crystal sizes of Fe_5C_2 and Fe_3O_4 (8-29 nm) in Table 3 are larger than those of the average pore diameters of the spent catalysts in Table 1 (10-15 nm). This suggests that the Fe_5C_2 and Fe_3O_4 particles are outside the micropores and mesopores.

Also, no Mo crystalline phase (oxide or carbide) is observed in the XRD pattern of the 6% Mo catalyst, probably indicating that the Mo precursor is highly dispersed on the AC support. Similar results on a 10wt% Mo/AC catalyst after H_2 treatment at 600°C were reported by Liang *et al.* [11]. However, when the Mo loading is increased to 12wt%, two additional peaks occur. The new peaks (at 21.4° and 23.7°) do not fit any form of molybdenum carbides or molybdenum oxides. But a new Mo-Fe oxide or Mo-Fe carbide phase might be formed for the 12wt % Mo catalysts during reduction or FTS reaction.

TPR. Patterns for 0, 6 and 12 wt% Mo catalysts are shown in Figure 2. All three patterns have similar shapes and can be characterized by five distinct structures in the temperature range of RT to 915°C . The first peak (Peak A, $200 - 300^\circ\text{C}$) could be assigned to the reduction of Fe_2O_3 to Fe_3O_4 and CuO to Cu [12,13]. However, the calibration results with pure CuO , as described earlier, indicate that the contribution of Cu in Peak A is negligible, relative to the contribution of Fe . The second peak, B, is observed in the temperature range of $300-400^\circ\text{C}$. Peak B may be assigned to the subsequent reduction of Fe_3O_4 to FeO . Peak C, observed at $400-700^\circ\text{C}$, may be assigned to the reduction of FeO to metallic Fe or, if Mo is present, to the reduction of MoO_3 to an oxide of Mo with low chemical valence, i.e. MoO_2 , or to Mo [14]. Peak C is much broader than Peaks A and B; it demonstrates that the reduction of iron in the third stage (FeO to metallic Fe) is a slow process [9,12]. The fourth peak, D, ($700 - 800^\circ\text{C}$) is relatively small and could be attributed to reduction of smaller Fe_3O_4 or FeO crystallites located in micro-pores to metallic Fe , since smaller particles are more difficult to reduce [15]. Alternatively, Peak D might be assigned to the reduction of a Mo-Fe oxide species formed at high temperature during TPR. The last peak, E ($800 - 915^\circ\text{C}$), is negative. This has been ascribed [14,16] to CO effusion due to the decomposition of oxygen-containing groups present on the surface of the AC support, and/or to the reaction between partially reduced metal oxides such as MoO_3 and Fe_2O_3 with H_2 and active carbon species on the AC surface [11,17].

The effect of Mo addition on the reduction behavior of the catalysts can also be seen in Figure 2. Peaks A and B for the 0% Mo catalyst are much larger and sharper than those of the 6 and 12% Mo catalysts, apparently indicating that Mo addition significantly inhibits iron reduction. This suggests that a strong interaction between Mo and Fe oxides exists during the reduction process. The areas in Peak C for the 6% and 12% Mo catalysts are larger than that of the 0% Mo catalyst. This is due to the additional reduction of Mo oxide to MoO_2 or to Mo between 400 and 750°C .

The H_2 consumed in each reduction stage in the TPR patterns was analyzed quantitatively, following calibration of TCD peak areas by pure CuO , as described earlier. The corresponding results for the three catalysts are summarized in Table 4 in terms of the degree of reduction R_T , as defined in Eqn (1) above. The total R_T and the R_T values of iron in the first and the second reduction stages (peaks A and B respectively) decrease with increasing Mo loading, indicating that Mo addition inhibits greatly the first-step and the second-step reductions of Fe_2O_3 ($\text{Fe}_2\text{O}_3 \rightarrow$

Fe_3O_4 and $\text{Fe}_3\text{O}_4 \rightarrow \text{FeO}$ respectively). The values of R_T of the three catalysts in the third reduction stage (peaks C and D) change less after addition of Mo than do the values in the first and second stages.

CO chemisorption and Isothermal Reduction. The results of CO uptake on the catalysts are shown in Table 5. The CO uptake on the 6%Mo/AC alone (i.e. without Fe, Cu, and K) is also listed in Table 5 for comparison. CO uptakes increase monotonically with the addition of Mo into the catalyst. The incremental CO uptake with addition of 6%Mo to the Fe-Cu-K catalyst is approximately 1 $\mu\text{mol/g-cat}$, less than the CO uptake for the 6%Mo/C. However, it is unlikely that the increase in CO uptake for the 6%-Mo catalyst is due only to Mo and not by a change in the particle size of Fe, since Mo peaks are not seen on the XRD patterns of the catalyst. On the other hand, with 12% Mo on the Fe catalyst, the incremental CO uptake is greater than that which can be ascribed to Mo, and is clearly due to an increase in dispersion, D (or a decrease in average crystallite size, d). The calculated values of D and d are also shown in Table 5. The decrease in particle size with increasing Mo as determined by CO chemisorption is less than the decrease using XRD (Table 3) but qualitatively consistent. Finally, the values of the degrees of reduction, R_I , in Table 5 are comparable with those in Table 4.

IV. Conclusions

The effects of Mo addition on the physico-chemical properties of Fe-Cu-K/AC were studied for the Fischer–Tropsch synthesis reaction over catalysts. The addition of Mo improves Fe dispersion after catalysts are reduced at 400°C for 12 h. Iron carbide (Fe_2C_5) and magnetite (Fe_3O_4) are detected on spent catalysts by XRD. These are postulated to be active phases for the FTS and WGS reactions. The addition of Mo prevents iron particles from agglomerating at reduction and reaction conditions, leading to improved catalyst stability of the catalysts.

TPR studies indicate a three-step reduction process of iron oxide on AC, $\text{Fe}_2\text{O}_3 \rightarrow \text{Fe}_3\text{O}_4 \rightarrow \text{FeO} \rightarrow \text{Fe}$, in three distinctive temperature ranges, 200 - 300°C, 300 - 400°C and 400 - 800°C. The reducibility of Fe-Cu-K/AC catalysts is affected greatly by the Mo promoter. The addition of Mo creates a strong interaction between Fe and Mo oxides. As a result, the extents of reduction of Mo-containing Fe-Cu-K/AC catalysts decrease. Quantitative TPR analysis confirms the results and shows the greater influence of the first and second stage reductions of iron oxide. Preliminary analysis of the reaction results, presented earlier [7], indicate that both the 6% and 12% Mo catalysts show much greater stability than the catalyst without Mo and that catalyst activity on the 6% Mo catalyst is higher than that of the 12% Mo catalyst. This might be due to the higher degree of reduction of iron oxide on the 6%Mo catalyst, which allows more reduced Fe to be carbonized to active sites for the FTS reaction.

V. Paper Presented or Published

Dady B. Dadyburjor, “Effect of Mo Loading and Support Type on Oxygenates produced during Fischer-Tropsch Synthesis Over Fe-Mo-Cu-K Catalyst Supported on Activated Carbon”, invited paper, presented at ACS National Meeting, San Diego, March 2005.

Wen-Ping Ma, Edwin L. Kugler, and Dady B. Dadyburjor, "Effect of Mo loading and support type on oxygenates produced during Fischer-Tropsch Synthesis Over Fe-Mo-Cu-K catalyst supported on Activated Carbon", *Prepr Pap. – Am. Chem. Soc., Div. Pet. Chem.* 2005 50(2), 161.

Wenping Ma, Edwin L. Kugler, James Wright and Dady B. Dadyburjor, "Activated Carbon Supported Mo-Fe Catalysts for Liquid Fuel Synthesis via Fischer-Tropsch Synthesis: Impact of Mo Addition on Reducibility, Activity and Hydrocarbon Selectivity," in preparation.

VI. Future Work

We will focus on reactivity studies with more detailed analysis of the products, corresponding to different catalyst compositions. This will allow us to optimize catalyst composition so that CH₄ and gaseous selectivities can be decreased, while improving C₅⁺ selectivity.

VII. References

- [1] Dry M. E. *Catal. Lett.* 1991, 7: 241.
- [2] Eilers J., Posthuma S. A., Sie S. T. *Catal. Lett.* 1991, 7: 253.
- [3] Venter J. J., Kaminsky M., Geoffroy G. L., Vannice M. A. *J. Catal.* 1987, 103: 450.
- [4] Steen E. van, Prinsloo F. F. *Catal. Today* 2002, 71: 327.
- [5] Kugler, E.L., Feng, L., Li, X., Dadyburjor, D.B. *Studies in Surface Science and Catalysis.* 2000, 130A: 299-304.
- [6] Li, X.G., Feng, L.J., Liu, Z.Y., Zhong, B., Dadyburjor, D.B., Kugler, E.L. *Ind. Eng. Chem. Res.* 1998, 37, 3853.
- [7] Ma, W., Kugler, E.L., Shao H., Wright, J. and Dadyburjor, D.B. Development Of Activated-Carbon-Supported, Molybdenum-Promoted Catalysts For Diesel Fuel Synthesis, Annual Report (2004).
- [8] Bukur, D.B., Koranne, M., Lang, X.S.Rao, ., K.R.P.M., Huffman, G.P., *Appl. Catal.* 126 (1995) 85.
- [9] Lox, E.S., Marin, G.B., DeGrave, E., Bussiere, P., *Appl. Catal.* 40 (1988) 197.
- [10] Rao, K.R.P.M., Huggins, F.E., Huffman, G.P., Gormley, R.J., O'Brien, R.J., Davis, B.H., *Energy & Fuels* 10 (1996) 546.
- [11] Liang, C.H., Ying, P.L., Li, C., *Chem. Mater.* 14 (2002) 3148.
- [12] Bukur, D.B., Sivaraj, C., *Appl. Catal.* 231 (2002) 201.
- [13] O'Brien, R.J., Xu, L.G., Spicer, R.L., Bao, S.Q., Milburn, D.R., Davis, B.H., *Catal. Today* 36 (1997) 325.
- [14] Feng, L.J., Li, X.G., Dadyburjor, D.B., Kugler, E.L., *J. Catal.* 190 (2000) 1.
- [15] Jacobs, G., Das, T.K., Zhang, Y.Q., Li, J.L., Racoillet, G., Davis, B.H., *Appl. Catal.* 233 (2002) 263.

[16] Sayag, C., Benkhaled, M., Suppan, S., Trawczynski, J., Djega-Mariadassou, G., Appl. Catal. 275 (2004) 15.

[17] Liang, C.H., Ma, W.P., Feng, Z.C., Li, C., Carbon 41 (2003) 1833.

Table 1. BET Measurements of Peat-AC support and Fe-Mo-Cu-K/AC Catalysts.

Support and Catalyst	Surface Area [m ² /g]		Pore Volume [cm ³ /g]		Ave Pore Size [nm]	
	Fresh	Spent	Fresh	Spent	Fresh	Spent
Peat AC	606	-	0.48	-	5.92	-
15.7% Fe / 0.8% Cu / 0.9% K/AC (a)	350	48	0.24	0.15	4.18	10.2
6 %Mo / 15.7% Fe / 0.8% Cu / 0.9% /AC (b)	347	34	0.25	0.16	4.06	15.2
12% Mo /15.7 Fe / 0.8% Cu / 0.9% K/AC (c)	280	32	0.22	0.06	5.73	10.4

(a) Spent catalyst evaluated after 72 h, 3Nl/gcat/h/300 psig, H₂/CO = 0.9.

(b) Same as above but evaluated after 396 h.

(c) Same as above but evaluated after 216 h.

Table 2 EDS Measurements of Peat-AC support and Fresh Fe-Mo-Cu-K/AC Catalysts.

Support and Catalyst	Fe/C Mole ratio		Mo [wt%]	
	Bulk	Measurement	Bulk	Measurement
Peat AC	-	-	-	-
15.7% Fe / 0.8% Cu / 0.9% K/AC (a)	0.045	0.053	-	-
6 %Mo / 15.7% Fe / 0.8% Cu / 0.9% /AC (a)	0.051	0.056	6	4.7
12% Mo /15.7 Fe / 0.8% Cu / 0.9% K/AC(a)	0.058	0.063	11.8	8.9

Table 3. Active Phases and Particle Sizes of Spent Catalysts from XRD

Mo Loading, wt%	Fe ₅ C ₂ [nm]	Fe ₂ O ₃ [nm]
0	21.2	28.4
6	13.6	12.2
12	8.4	8.2

Table 4. H₂ Consumption and Degree of Reduction from TPR Measurements.

Mo Loading [wt%]	Measured H ₂ Consumption [mmol/gcat] (a)				Theor. H ₂ Cons. [mmol/gcat]	Degree of Reduction, R _T [%]				
	Peak A	Peak B	Peak C	Peak D		Peak A	Peak B	Peak C	Peak D	Total
0	0.81	1.44	1.56	0.12	4.34	19	33	36	2.8	90
6	0.54	1.14	2.57	0.10	6.22	8.6	18	41	1.6	70
12	0.52	1.00	2.87	0.11	8.04	6.5	12	36	1.4	56

(a) AC Support contributions have been subtracted to obtain these values.

Table 5. Results of CO Chemisorption. Catalysts contain 15.7% Fe / 0.8% Cu / 0.9% K/AC unless otherwise specified.

Mo Loading [wt%]	CO adsorbed [μmol/gcat]	Dispersion, D [%] (a)	Particle Size, D [nm] (b)	Degree of Reduction, R _I [%]
0	24.7	1.9	37.9	89.0
6	25.6	2.4	31.2	71.2
12	28.0	3.6	20.8	49.1
6Mo/AC only	1.6	-	-	-

Figure 1. X-Ray Diffraction Patterns of Spent Fe-Mo-Cu-K/AC Catalysts

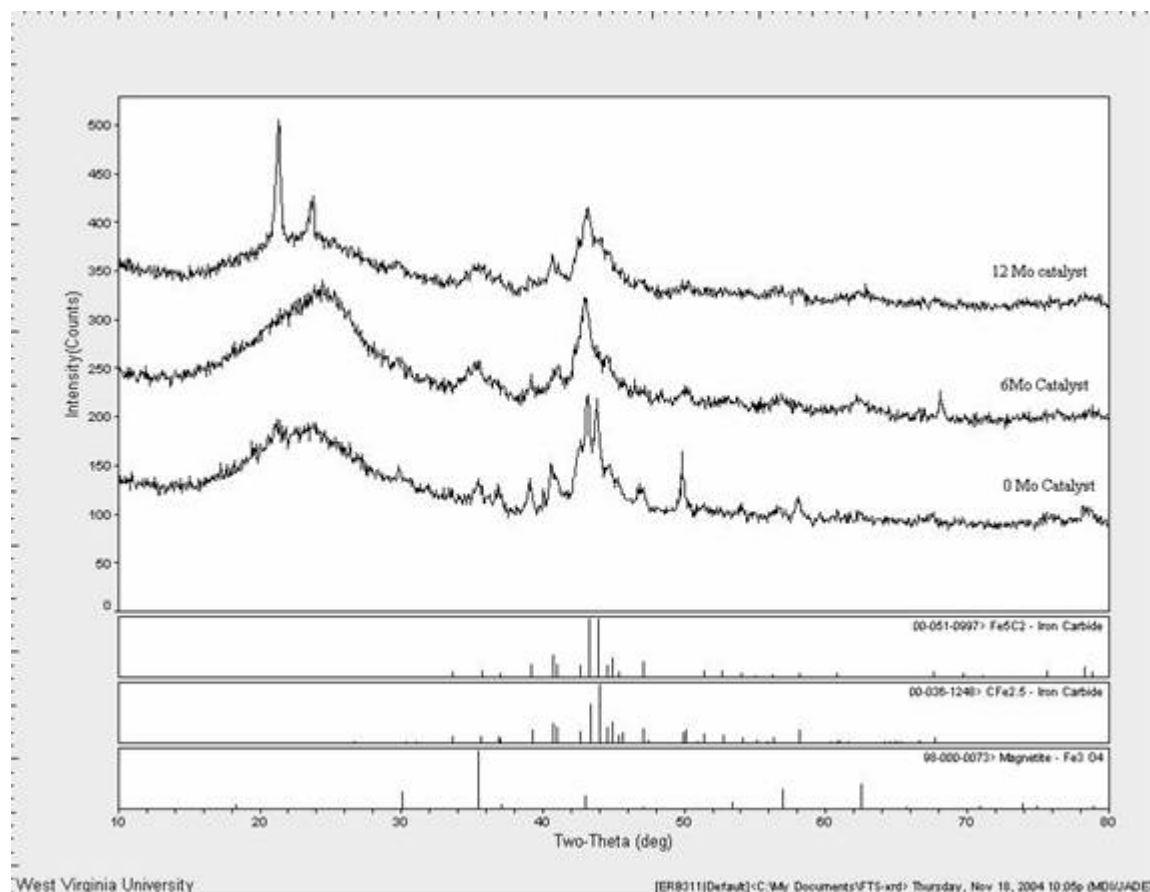
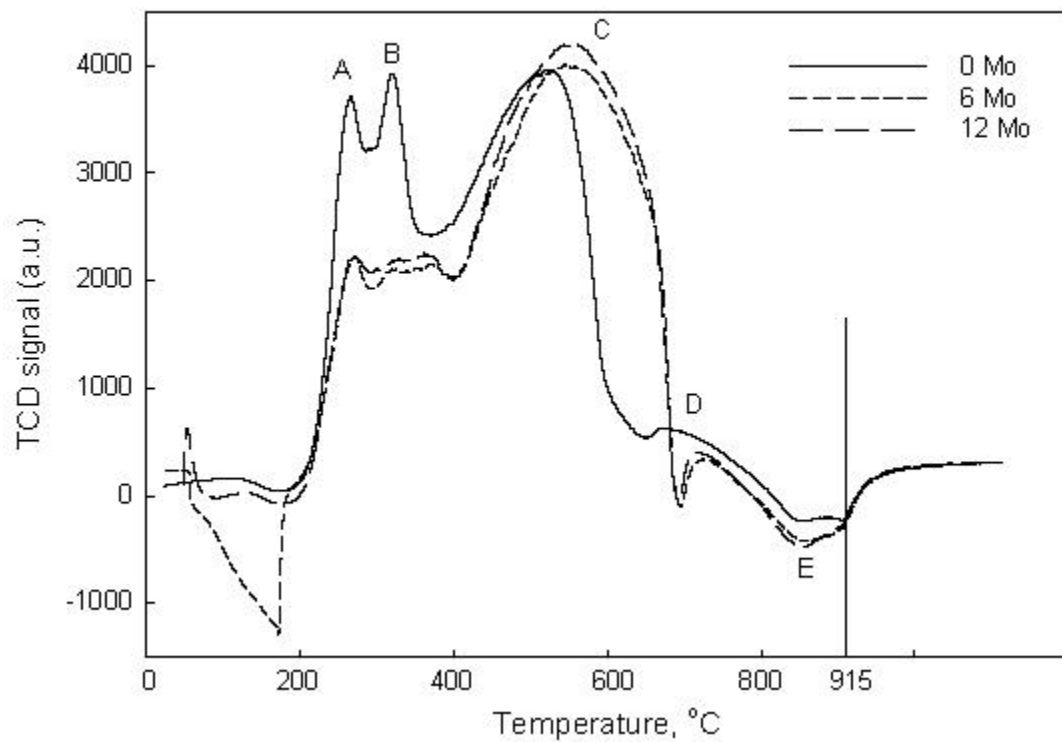


Figure 2. TPR Profiles of Fe-Mo-Cu-K/AC Catalysts.



New Catalysts for the Production of Chemicals,

Light Olefins and Hydrogen via C-1 Chemistry

Xiwen Huang, Luckner Jean, and James A. Guin

Department of Chemical Engineering

Auburn University, Auburn, AL, 36849-5127

Introduction

Our progress report for this six-month period discusses our work in two areas: (1) The production of light olefins and chemicals from methanol using SAPO catalysts, and (2) the production of hydrogen by dehydrogenation of cyclohexane over SBA supported Pt and Ru catalysts.

Hydrogen Production. The dehydrogenation-hydrogenation of cyclic hydrocarbons, i.e. cyclohexane, methylcyclohexane, tetralin, etc. has been proposed as a possible technology to store, transport, and locally produce hydrogen.¹⁻⁴ Some advantages of this are lack of poisonous CO, reaction reversibility, relatively high hydrogen content (6-8 wt.%), and convenient liquid phase transportability. We have studied the development of mesoporous silicates, such as SBA-n,⁵⁻⁷ as possible supports for metal, e. g. Pt, Ru, catalysts. These sieves possess high surface areas (700-1500 m²/g), pore volumes (0.8-1.2 cm³/g) and ordered pore structures with narrow size distribution and the pore diameter can be tailored from 2 to 50 nm.⁷

Light Olefins Production. Production of light olefins (C₂-C₄) from methanol or syngas over SAPO catalysts has generated considerable interest in recent years as this provides an indirect way of converting fossil resources to industrially valuable olefins and other value-added products such as polymers and fine chemicals. Catalytic activity and selectivity for light olefins can be influenced by many catalyst parameters such as silicon content, acid site density, acid strength, crystallite size, and nature of template. The effect of catalyst particle size using SAPO-34, -44, -47 and -56 catalysts developed earlier in our lab was studied. Our investigations included testing activity and selectivity of these SAPO's, some of which were modified by Ru addition by CFFS colleagues at the University of Utah.

Experimental

Catalyst Synthesis. The synthesis of mesoporous SBA-11, -12, -15, and -16 was performed per literature methods.^{6,7} The supports were recovered, washed, air dried at room temperature and calcined at 500°C for 6hr with air flow. SAPO catalysts synthesized by Dr. Prakash M. Adekkanattu as reported earlier under this contract were used herein.

Metals addition: For wetness impregnation of 1% Pt/SBA-15, H₂PtCl₆.6H₂O was used in H₂O. Ion-exchange was performed using Pt(NH₃)₄Cl₂ in H₂O with a small amount of aqueous NH₃ (10 wt.%) added to reach pH ~8. Both procedures were followed by solids washing, drying, and calcination. For Ru loading, the appropriate amounts of bis(2,4-

dimethylpentadienyl)ruthenium were added to SAPO and SBA supports using a vapor phase vacuum technique developed by Dr. Richard Ernst and co-workers at the University of Utah⁸. These Ru loaded samples were oxidized in oxygen up to 350°C.

Characterization. TEM was performed at the University of Kentucky by Dr. Naresh Shah and co-workers to characterize mesoporous SBA structure. SEM was performed at Auburn University.

Reactions. Cyclohexane dehydrogenation was tested in an 18" x 0.5" 316 ss fixed bed reactor by vaporizing a small amount of liquid cyclohexane into nitrogen. The catalyst was reduced in H₂ prior to feed introduction. Detailed conditions are in **Table 1**. SAPO catalysts were tested in a fixed-bed with an 81.2 cm x 0.95 cm quartz tube by vaporizing liquid methanol flowing at a rate of 3 μl/min into a nitrogen gas stream (38 ml/min) at a temperature of 400°C and pressure of 1 atm (**Figure 1**). For particle size reduction, samples were ground for 5, 10, and 15 min. time intervals with a Wig-L-Bug grinder. All analyses were by Varian 3000 GC.

Results and Discussion

Micrographs. The TEM micrographs obtained at the University of Kentucky for various SBA supports showed mesoporous structures as in **Figures 2 (a)** and **(b)**, although, the SBA 16 sample examined did not show mesoporous structure. Furthermore, following Pt impregnation some samples did not evidence typical SBA structure. In some cases Pt precipitated as larger particles, while in other cases Pt whisker morphologies were observed. For the SAPO catalysts, SEM micrographs revealed intergrowth of cubic crystals with average size of 40 μm formed during crystallization (**Figure 3(a)**), and these crystals were used to examine the effect of grinding on the catalyst particle size as shown for SAPO-44 in **Figure 3(b)**.

Hydrogen Production. The rate of hydrogen production from cyclohexane is increased at higher reaction temperature as shown in **Figure 4**. Hydrogen production begins around 100°C and is complete at about 250°C. The effect of Pt loading on cyclohexane conversion is shown in **Figure 5** at two temperatures where one observes an optimum loading around 1-2% Pt. **Figure 6** shows that among SBA's and two commercial catalysts, 1% Pt/C and 1%Pt/Al₂O₃, the 1% Pt/SBA-15 gave highest conversion and is actually higher than the two commercial catalysts. The literature reports that the pore size of SBA-15 may be adjusted by addition of organic cosolvents.⁷ To explore this effect, we added trimethylbenzene during the synthesis of SBA-15 to adjust the pore sizes to 8.6nm, 12nm and 30 nm pore size respectively, according to literature procedures (not actually measured). **Figure 7** shows that cyclohexane conversion significantly decreases when the pore size increases to 30nm. As shown in **Figure 8**, both impregnation and ion exchange of Pt yielded comparable activities. We also compared the cyclohexane conversion with two different metals, 1% Pt and 1% Ru, both on SBA-15. As shown in **Figure 9**, while the Ru catalyst is effective, the Pt variety generally has greater activity. More work using the vapor phase organometallic deposition method would be very interesting however, as the potential for higher metals dispersion is very good.

Light Olefins Production. **Figures 10** and **11** show both temperature and particle size effects on product distribution from SAPO-44. The catalyst remained active much longer with reduced particle size as shown by the greater olefins yield. Such effects were also apparent for SAPO-34 and 47, but not for SAPO-56. The effect of grinding for various times to reduce SAPO-44 catalyst particle size on C₂-C₄ olefins production is shown in **Figure 12**. The particle size reduction results in a doubling of catalyst lifetime from about 4 to 8 hours for olefins production. Similar results were obtained for SAPO-34; however effects were not as significant

SAPO's-47 and 56. The differences in these results could be due to effective pore diffusion effects particular to each separate catalyst. The effect of Ru modification of SAPO-44 can be seen by comparing the product selectivity in **Figures 13 and 14**. These results indicate the Ru-SAPO catalyst activity in **Figure 14** is about the same as the unmodified SAPO in **Figure 13**. Similar behavior was observed for Ru-SAPO-56. However, SAPO-34 yield, activity, and selectivity diminished somewhat after Ru modification.

Conclusions

Mesoporous SBA supported Pt catalysts appears to offer good potential for hydrogen production from cyclohexane, although Ru impregnated SBA is also active. Catalyst particle size reduction is effective in increasing olefins yield and lifetime in some, but not all, SAPO catalysts. Ru addition to the SAPO catalysts did not appear to offer significantly increased lifetimes, although other metals may be effective in this regard.

Future Work

We plan to continue our work on the development of catalysts for hydrogen production and for the production of light olefins from methanol .

References

1. Ali, L.I., Ali, A-G., Aboul-Fotouh, S.M., Aboul-Gheit, A.K. *Applied Catalysis A: General* 177, **1999**, 99.
2. Kariya, N., Ichikawa, M., *Applied Catalysis A: General*, 233, **2002**, 91.
3. Wang, Y., Shah, N., Huffman, G.P., *Energy & Fuels*, 18(5), **2004**, 1429.
4. Huffman, G.P., Shah, N., Wang, Y., Huggins, F.E., *ACS Div. of Fuel Chem. Preprints*, 49(2), **2004**, 731.
5. Huo, Q., Margolese, D.I., Ciesla, U., Demuth, D.G., Feng, P., Gier, T.E., Sieger, P., Firouzi, A., Chemelka, B.F., Schöth, F., Stucky, G.D., *Chem. Mater.*, 6, **1994**, 1176.
6. Zhao, D., Feng, J., Huo, Q., Melosh, N., Fredrickson, G.H. Chemelka, B.F., Stucky, G.D., *Science*, 279, **1998**, 548.
7. Zhao, D., Huo, Q., Feng, J., Chemelka, B.F., Stucky, G.D., *J. Am. Chem. Soc.*, 120, **1998**, 6024.
8. Wilson, D.R.; Stahl, L.; Ernst, R. D.; *Organometallic Synthesis*, 3, 1986, 136

Table 1. Reaction Conditions for Cyclohexane Dehydrogenation

Catalysts: (1~5%)Pt/SBA-n; 1%Pt/Al₂O₃; 1%Pt/C; 0.5g.
N₂ flowrate: 50 sccm.
Cyclohexane liquid flowrate: 0.005cc/min.
Temperatures: 100°C; 150°C; 200°C; 250°C; 300°C.
Pressure: 1 atm.
Pretreatment: 50 sccm H₂, 4 hrs, 450°C.

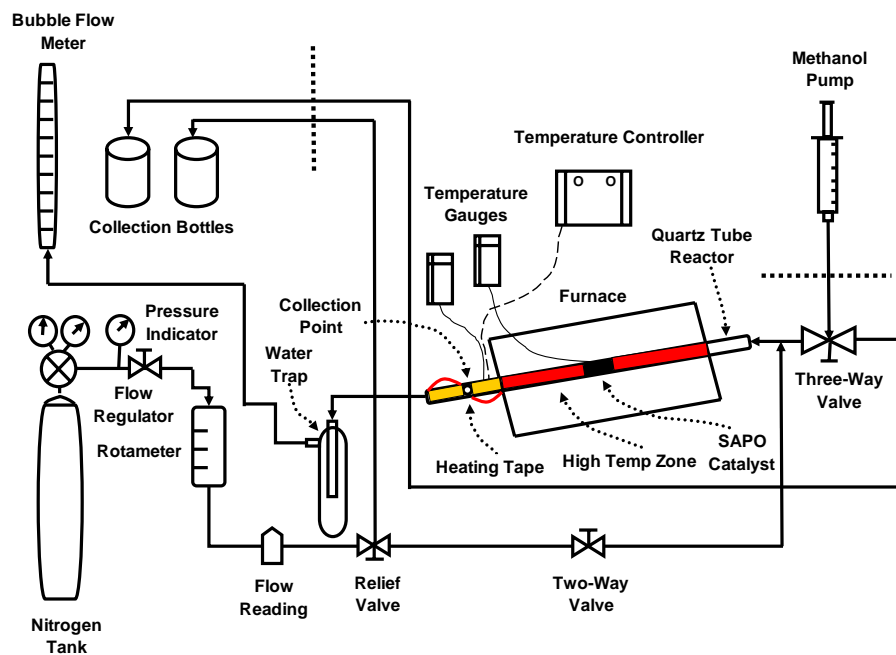


Figure 1. MTO Reactor Diagram

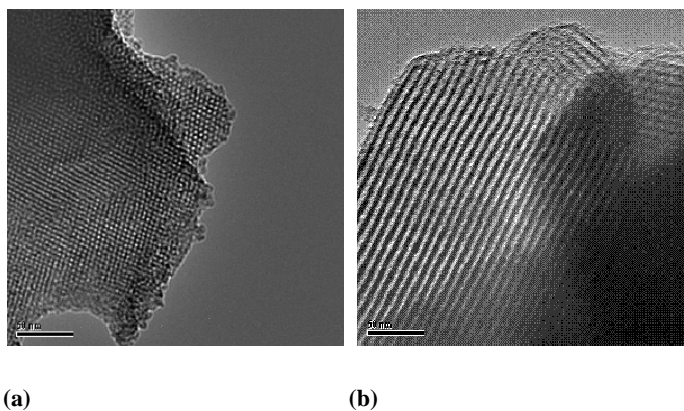
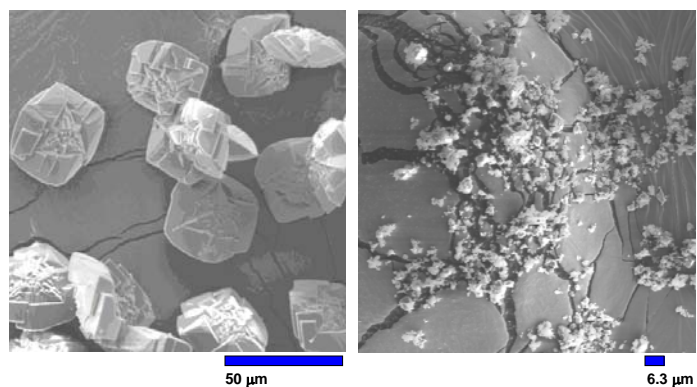


Figure 2. TEM Micrographs of SBA Supports Performed at the University of Kentucky: (a) SBA-12; (b) SBA-15. Scale = 50 nm



(a) (b)
Figure 3. SEM Micrographs of SAPO-44: (a) Catalyst in original size; (b) Catalyst after 15 min grinding .

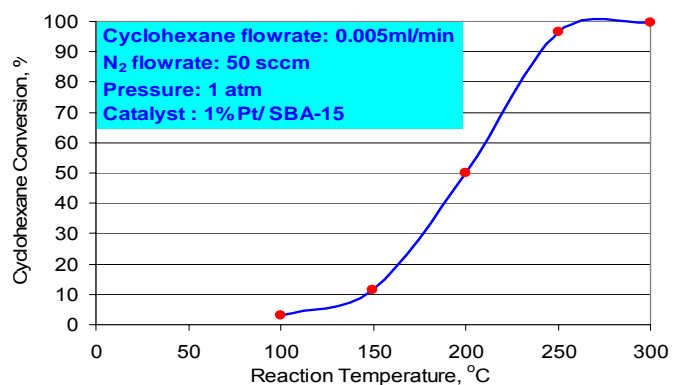


Figure 4. Temperature Effects on Cyclohexane Conversion.

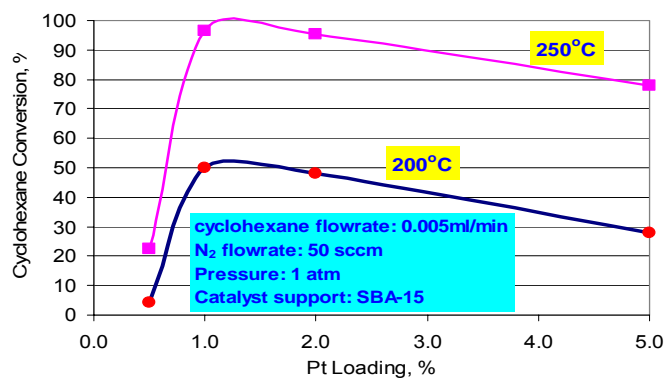


Figure 5. Pt Loading Effects on Cyclohexane Conversion.

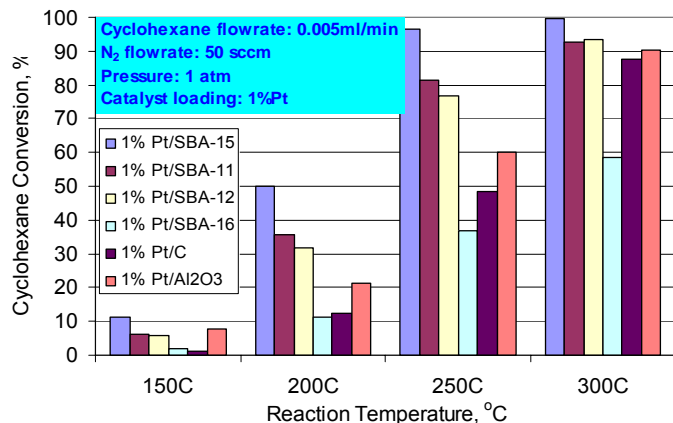


Figure 6. Catalyst Support Effects on Cyclohexane Conversion.

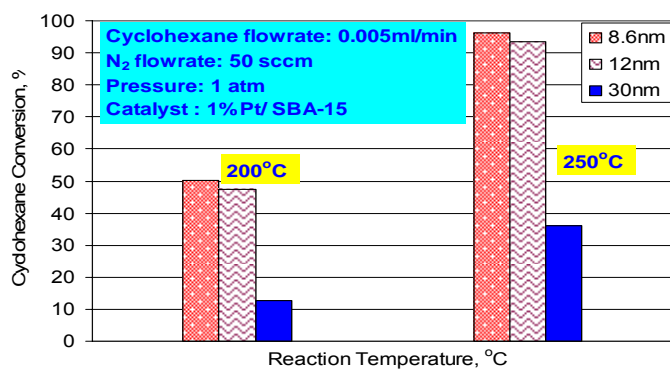


Figure 7. Catalyst Pore Size Effects.

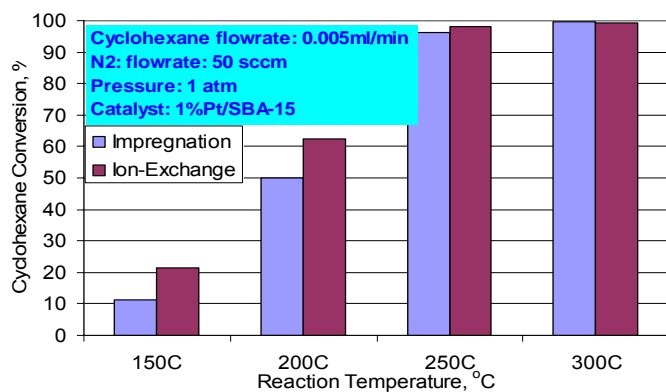


Figure 8. Effect of Impregnation vs. Ion-Exchange.

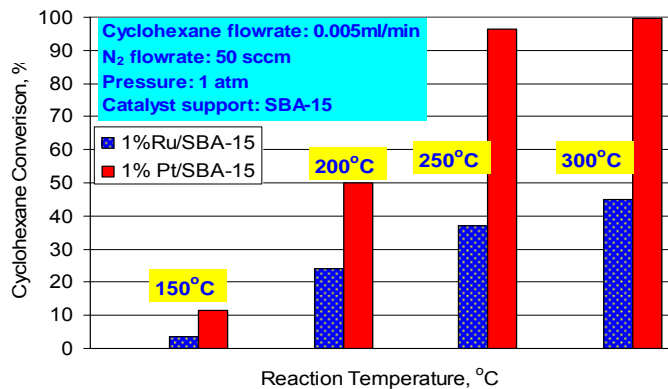


Figure 9. Comparison of Pt and Ru on SBA-15.

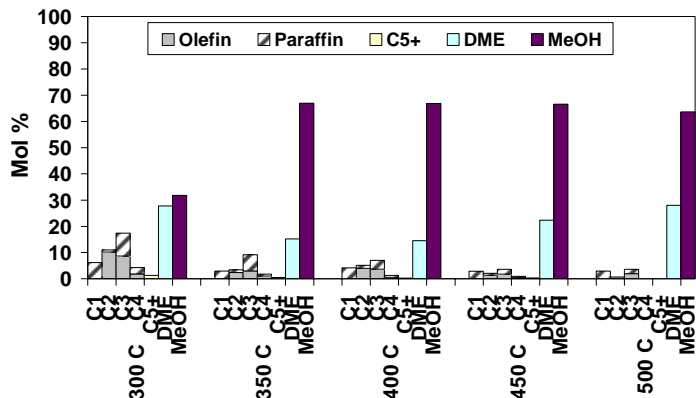


Figure 10. Temperature Effect on Product Distribution over SAPO-44, (No Grinding), WHSV = 0.6hr⁻¹

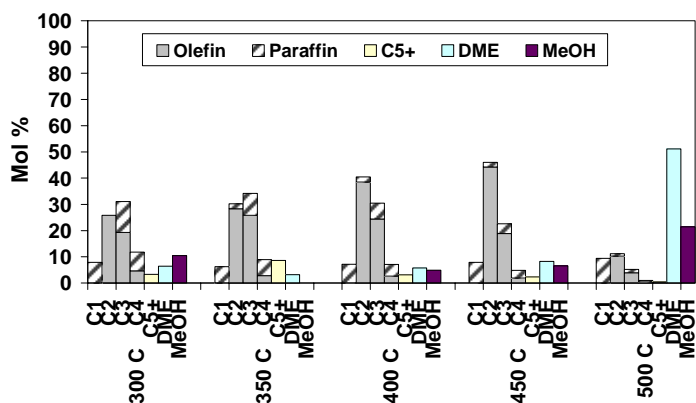


Figure 11. Temperature Effect on Product Distribution over SAPO-44, (After 15 min. Grinding), WHSV = 0.6hr⁻¹

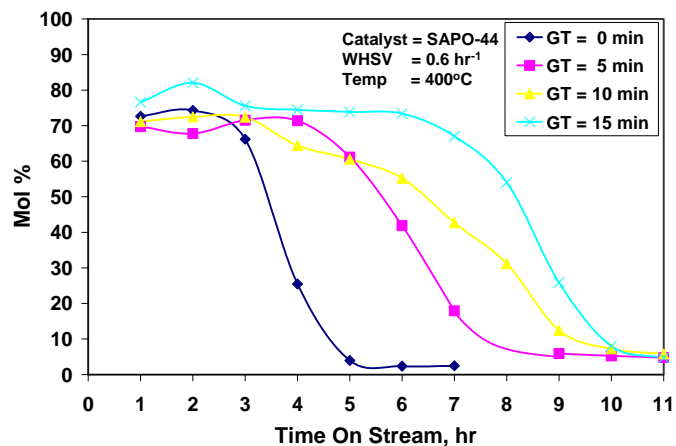


Figure 12. Grinding Time Effect on C₂ – C₄ selectivity over SAPO-44. (GT = Grinding Time)

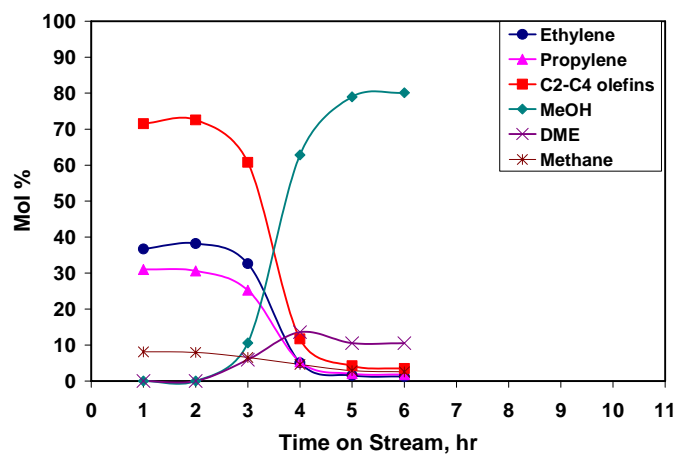


Figure 13. Product Selectivity Profile over SAPO-44.

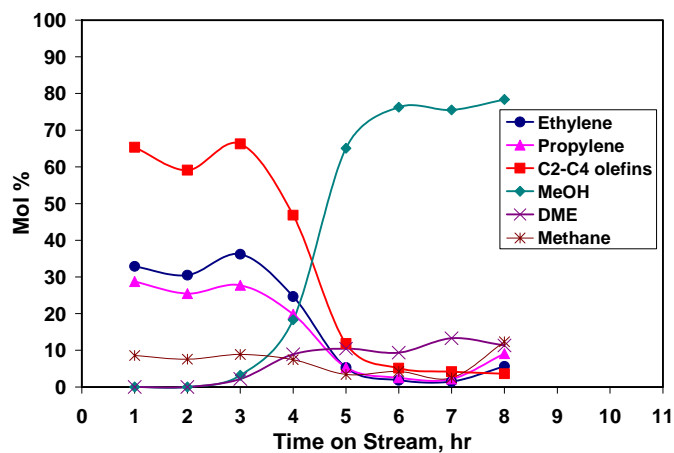


Figure 14. Product Selectivity Profile for Ru-SAPO-44.

What C-13 chemical shift tensors can tell us about metal ligand interactions in catalysts

Ronald J. Pugmire and Zhiru Ma

Department of Chemistry and Department of Chemical Engineering

University of Utah

Introduction

Catalysts will play an increasingly important role in the development of C1 chemistry and the production of hydrogen. The NMR group at Utah is now focusing on understanding subtleties in catalyst structure and function.

Experimental

We have recently focused our research on catalyst systems with the goal to explore the feasibility of obtaining FIREMAT data on various metal-ligand complexes. The FIREMAT¹ experiment has proven to be a very useful tool for obtaining carbon-13 chemical shift tensor data.

Results

Twenty years ago low temperature shift tensor principal values were obtained in the Utah laboratory on a series of metal diene complexes² and some of these data were later included in an extended data set by Oldfield, et. al.³ The earlier Utah data was obtained by fitting the powder patterns of the complexes and the error in these STPV's can be as high as 5-10 ppm. We have now begun to revisit this topic employing the high resolution FIREMAT technique. The additional resolution obtainable by this experimental technique has led to the discovery of additional resonance lines in the spectra of several metal-ligand complexes that we have recently studied. An illustrative example is found in the spectrum of (bicyclo[2.2.1]hepta-2,5-diene) dichloropalladium (II) (see Figure 1) in which the diene-carbons are split into a doublet separated by 2 ppm. This spectral feature is due to a break in the crystal symmetry arising from slight differences (~0.02 angstrom) in the palladium-diene bond lengths. The PVST data of these carbons are readily obtained from the FIREMAT data and these values are given in Table 1. Similar NMR data have been obtained in (1,5 cyclooctadiene) dimethylplatinum (II).

Table 1. Shift Tensor Principal Values in (bicyclo[2.2.1]hepta-2,5-diene)dichloropalladium(II)

Carbon	δ_{iso}	δ_{11}	δ_{22}	δ_{33}
Diene (CH)	94.1	191.2	87.1	4.0
Diene (CH)	92.1	188.9	85.5	2.0
CH	66.1	100.1	68.7	29.6
CH2	52.4	66.1	56.0	35.0

Conclusions

These data illustrate the high degree of sensitivity to local structural variations. The data we have obtained at this writing have laid the ground work of a wider range of complexes that will be studied. We will begin modeling these data by means of quantum mechanical techniques in the

next few months. Exploration of the relativistic effects on the ligands will be included in our modeling efforts.

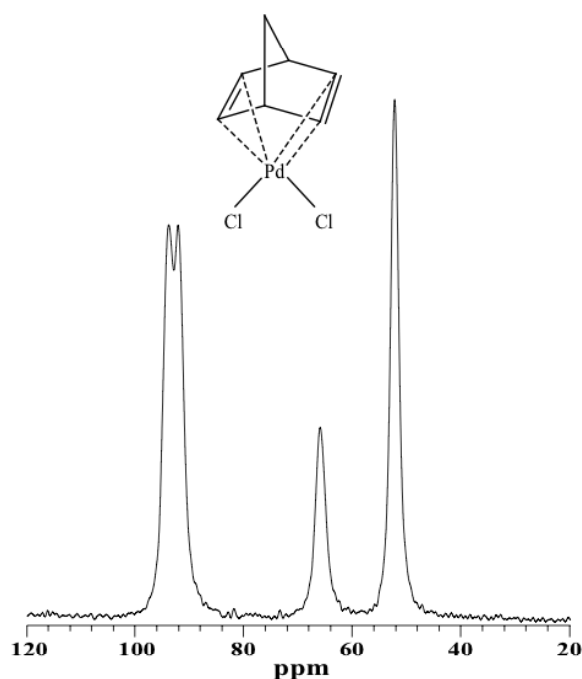


Figure 1. CP/MAS spectrum of (bicyclo[2.2.1]hetap-2,5-diene)dichloropalladium(II).

References

1. A Sensitive High-Resolution Magic-Angle-Turning Experiment for Measuring Chemical-Shift-Tensor Principal Values. D.W. Alderman, G. McGeorge, J.Z. Hu, R.J. Pugmire and D.M. Grant, 1998, *Mol. Phys.*, 95, 1113-1126.
2. Low Temperature Solution Studies of Copper(I) Complexes and Trans-Cycloalkenes and Solid State ^{13}C NMR Studies of Metal-Diene Complexes, Gregory Michael Wallraff, Ph.D. thesis, Department of Chemistry, University of Utah, 1985.
3. Solid-State NMR and Density Functional Investigation of Carbon-13 Shielding Tensors in Metal-Olefin Complexes, R. Havlin, M. McMahon, R. Scinivasan, H. Le, and E. Oldfield, *J. Phys. Chem. A* **1997**, 101, 8908-8913.

Science behind Catalysis in C1 Reactions: Catalyst characterization and determination of Active Species

M. S. Seehra, P. Dutta and A. Manivannan
Physics Department, West Virginia University.

Semiannual Report for the period October 1, 2004 to March 31, 2005

I. Introduction

Recently, a number of studies of Fischer-Tropsch (FT) synthesis using cobalt catalyst supported on high surface area xerogel [1], aerogel [2,3], SiO₂ and Al₂O₃ [4,5] have been reported. The factors that effect the yields and product distribution of the FT products include operating temperature and pressure, surface area and pore size of the support, particle size and dispersion of cobalt and its electronic state (Co⁰, Co²⁺, Co³⁺). To prepare the Co loaded catalyst, Co is usually impregnated as an oxide, followed by reduction and/or calcination to produce the desired Co⁰ state which is the active catalyst. In order to compare the yield and product distribution with Co loading, it then becomes essential to determine the concentration of the various electronic states and phases of Co present in the catalyst. In this report, we summarize the results of our recent investigations for determining the different oxidation states of Co and their concentrations in Co/xerogel, Co/aerogel, Co/SiO₂ and Co/Al₂O₃ catalysts. Only summary of these results is presented below, with the details given in the quoted papers [1-5].

II. Experimental

The crystalline phases present in a catalyst were determined by room temperature x-ray diffraction (XRD) in a Rigaku diffractometer using CuK_α radiation ($\lambda = 0.15418$ nm). The XRD technique is able to detect phases with concentration ≥ 3 %. The magnetic phases such as Co²⁺, Co³⁺, Co⁰, CoO, and Co₃O₄ were determined by magnetic measurements which were done using a commercial SQUID (superconducting quantum interference device) magnetometer. Additional information on states such as Co²⁺ was also determined by EMR (electron magnetic resonance) spectroscopy at the X-band frequency $f = 9.28$ GHz with a variable temperature (4 K to 300 K) cryostat. The important information on the electron state is contained in the g-value given by the EMR resonance condition $hf = g\mu_B H_0$, where h is the Planck's constant, μ_B is the Bohr magneton and H_0 is the resonance field of the EMR lines.

III. Results and Discussion

An example of the information obtained from the XRD studies is given in Fig. 1. Here we have shown the XRD patterns of Co/xerogel catalyst in which clear identification of Co⁰, CoO and the support SiO₂ (xerogel) is made. (This figure is from the supporting materials of Ref. 1). In the Co/SiO₂ catalysts of Ref. 4, the XRD studies could only detect Co₃O₄, and Co⁰ and CoO were absent [4]. Thus which phases of Cobalt (Co⁰, CoO or Co₃O₄) are present in a catalyst depend on the experimental conditions the catalyst is exposed to and these different states can usually be detected by XRD.

Careful analysis of the temperature (T) and magnetic field (H) variation of the magnetization (M) provide additional details about the electronic states of cobalt and their concentrations. The presence of CoO and Co₃O₄ are detected from the peaks in susceptibility $\chi = M/H$ at temperatures $T \approx 300$ K and $T \approx 40$ K respectively [3-5] whereas if Co⁰ is present, it dominates the measured magnetization from which its concentration can be determined [3]. In Fig. 2, we show our recent data from Ref. 3 on the χ vs. T variation in 10% Co/aerogel catalyst. The peak in χ near 20 K is due to Co⁰ nanoneedles with diameter $d \approx 1$ nm, whereas the peak in χ near 300 K (Fig. 3) is due to the presence of CoO. From the magnitude of the saturation magnetization of this sample at 5 K, the concentration of Co⁰ was determined to be around 8%. If Co⁰ is simultaneously present with either CoO or Co₃O₄, then from the behavior of the hysteresis loop of Co⁰ in a field cooled sample, it can be determined whether Co⁰/CoO or Co⁰/Co₃O₄ are present as composite systems in core-shell structures or as individual phases. A shifted hysteresis loop under field-cooled conditions represents a core/shell structure [1]. An example of this is given in Fig. 4 for the 5% Co/xerogel sample. Here the hysteresis loop is shifted by 55 Oe when the sample is cooled in 10 kOe suggesting a core/shell structure for Co and CoO in this sample.

Another possibility for the cobalt state is that cobalt is incorporated substitutionally into the support (e.g as Co_xSi_{1-x}O₂) or chemisorbed on the surface of the support with bonding provided by surface absorbed H₂O and O₂. In such cases, the χ vs. T data follows the Curie-Weiss law: $\chi = \chi_0 + [C/(T-\theta)]$ where C gives the concentration of the Co⁺ⁿ ions [4]. Furthermore, the variation of M vs. H at a low temperature (2 K) can be used to distinguish between Co²⁺ and Co³⁺ ions [4]. In the EMR studies of such materials, the presence of an EMR line at $g = 4.3$ is definite confirmation of the presence of Co²⁺ ions [6].

Next, the relationship between the different electronic states of cobalt and their concentrations with the F-T products and their distributions is discussed briefly. In the conventional gas-phase FT synthesis at 240⁰C and 20 bar pressure, it was found that the presence of Co₃O₄ yields higher methane selectivity whereas the presence of Co²⁺ species yielded lower methane selectivity but higher olefin selectivity [4]. Similarly why the FT activity of 10 % Co/aerogel catalysts is not much better than that of 6 % Co/aerogel [2] has been explained in our recent work [3] in that the 10% Co/aerogel contains unreduced CoO and a complex cobalt silicate in addition to the desired Co⁰.

IV. Conclusions/Future Work

Here we have described how different electronic states and phases of cobalt in cobalt-based FT catalyst are determined using XRD, magnetometry and EMR spectroscopy. Such information is essential in understanding the nature of products and their distributions in FT synthesis. Work on other catalyst systems currently underway will be reported in future reports.

V. Papers Published/References

1. Silica Xerogel Supported Cobalt Metal Fischer-Tropsch Catalysts for Syngas to Diesel Range Fuel Conversion: B. C. Dunn, D. J. Covington, P. Cole, R.J. Pugmire, H.L.C. Meuzelaar, R.D. Ernst, E.C. Heider, E. M. Eyring, N.Shah, G.P. Huffman, M. S. Seehra, A. Manivannan, and P. Dutta; *Energy & Fuel*, 18, 1519-1521, (2004).

2. Silica aerogel supported catalysts for Fischer-Tropsch synthesis: B. C. Dunn, P. Cole, D. J. Covington, M.C. Webster. R.J. Pugmire, R.D. Ernst, E. M. Eyring, N.Shah, and G.P. Huffman; *Appl. Catal. A: General*, 278, 233-238 (2005).
3. Characteristics of Cobalt nanoneedles in 10% Co/aerogel Fischer-Trosch catalyst: P. Duuta, B.C. Dunn, N. Shah, E. M. Eyring, G. P. Huffman, A. Manivannan and M.S. Seehra; (to be submitted).
4. Characterization of Fischer-Tropsch Cobalt-based Catalytic Systems (Co/SiO₂ and Co/Al₂O₃) by X-ray Diffraction and Magnetic Measurements: P. Dutta, N.O. Elbashir, A. Manivannan, M.S. Seehra, and C.B. Roberts; *Catalysis Letters* 98, 203-210 (2004).
5. Impact of Cobalt-based Catalyst Characteristics on the Performance of Conventional Gas-Phase and Supercritical-Phase Fischer-Tropsch Synthesis: N.O. Elbashir, P. Dutta, A. Manivannan, M.S. Seehra, and C.B. Roberts; *Applied Catalysis A : General* (2005), 12 pages (in press).
6. Nature of the reversible paramagnetism to ferromagnetism state in cobalt-doped TiO₂: A. Manivannan, G. Glaspell, P. Dutta and M. S. Seehra, *J. Appl. Phys.* May 2005, 3 pages (in press).

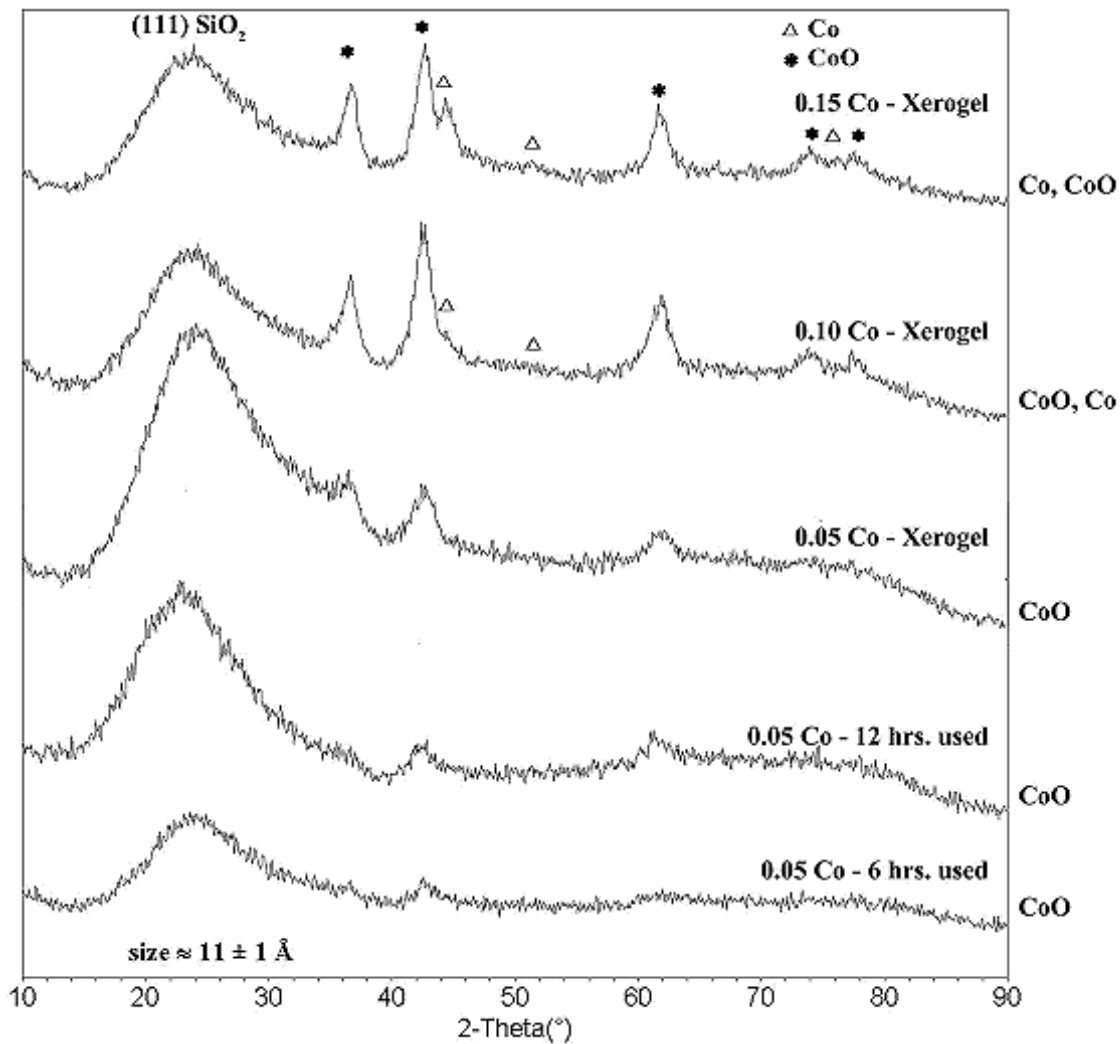


Figure 1. Room Temperature x-ray diffractograms of five samples of Co/xerogel with the peaks for Co^0 , CoO and SiO_2 identified. The size $\approx 11 \text{ \AA}$ is for SiO_2 [Ref. 1].

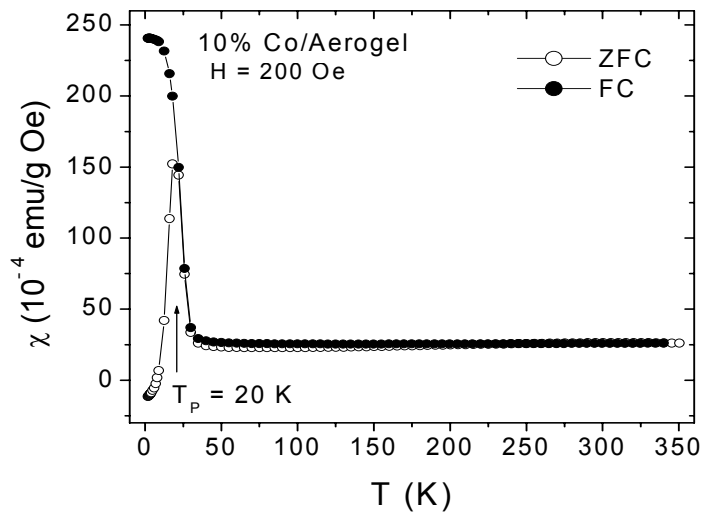


Figure 2. Temperature dependence of the magnetic susceptibility χ of 10% Co/aerogel catalyst for the ZFC (zero-field cooled) and FC (field-cooled) cases.

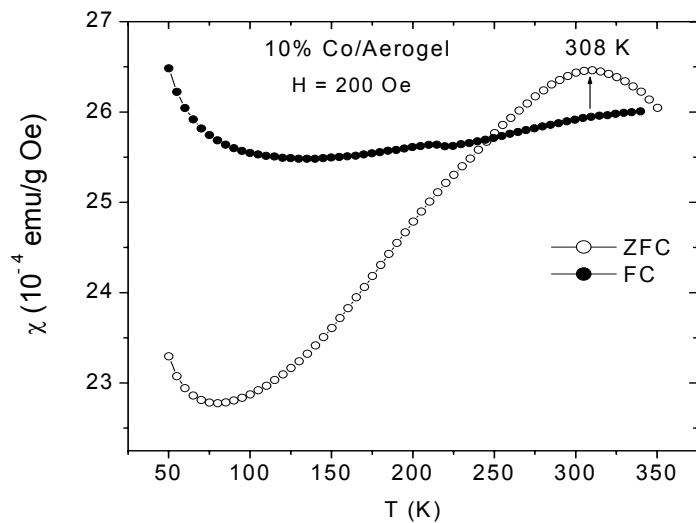


Figure 3. Expanded version of the χ data of Figure 2 for higher temperatures.

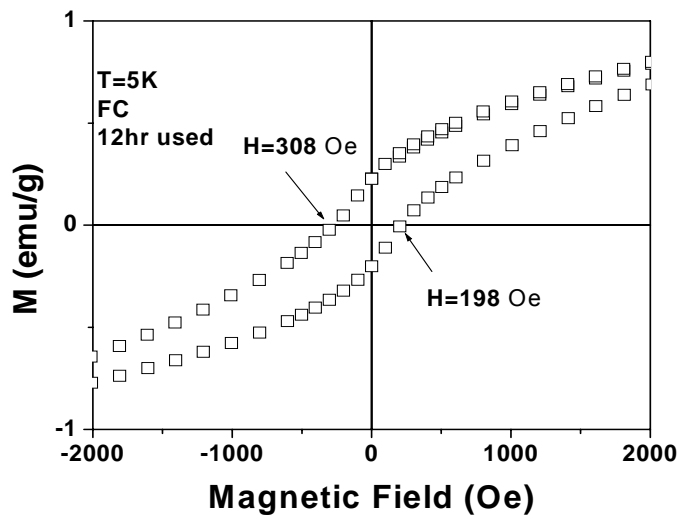
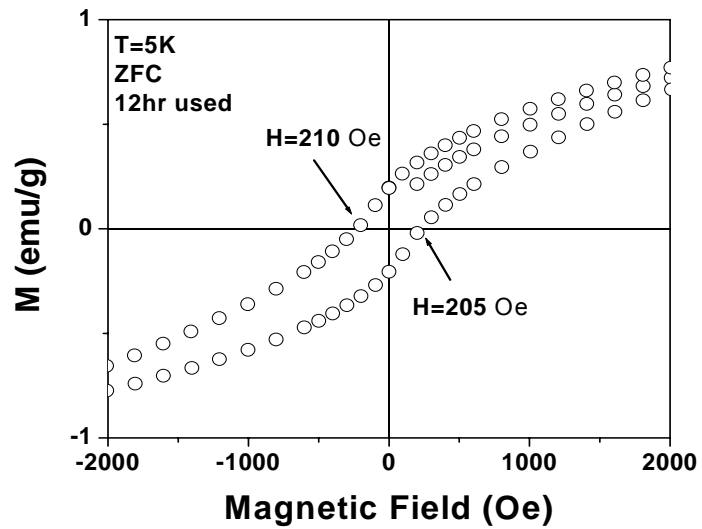


Figure 4. Hysteresis loops measured at 5 K for the 12-hr sample of 0.05 Co/aerogel under the ZFC and FC ($H = 10$ kOe) conditions. The loop shift for the FC case supports the core/shell model discussed in the text.

Mössbauer, XAFS and TEM Analysis of Fe-Mo WGS catalysts

Frank E. Huggins, Y. Chen, N. Shah
University of Kentucky, Lexington, KY 40506

Introduction

A suite of six catalyst samples designed for use or used in the water-gas shift (WGS) reaction were received from Dr. Dadyburjor, West Virginia University. The six samples consisted of relatively coarse, dark-brown particles and were identified only as WVU-1 through WVU-6. These samples were submitted for analysis by Mössbauer and Mo K-edge spectroscopies. A brief transmission electron microscopic investigation was also carried out on samples WVU-1 and WVU-2.

Experimental Methods

(a) Mössbauer spectroscopy:

Mössbauer spectroscopy was carried out using Halder, GmbH, Mössbauer control and driving units interfaced by means of MCS/PHA boards from Canberra Nuclear, Inc., to a personal computer running MS-DOS. The Mössbauer spectra were collected over two regions of 512 channels (1,024 total channels) in mirror image mode using a symmetric constant acceleration waveform. Collection times were ~ 100 μ s per channel and the data collection and driving unit oscillations were synchronized by means of a start pulse from the Halder control unit, which occurred at a rate of ~ 9 Hz. Data were accumulated in the MCS mode at a rate of about 10,000-20,000 cts/sec and continued until at least 10^6 counts had been collected in each channel. An Ar/CH₄ filled proportional counter, operating at 1750 V, was used to record the counts. This signal was amplified by means of a pre-amplifier and an amplifier before reaching the MCS/PHA boards. To calibrate the unknown spectrum, the Mössbauer spectrum of a thin (6 μ m) metallic Fe foil was accumulated at the opposite end of the drive using a similar proportional counter and signal amplification system. The gamma-ray source material at each end of the driving unit consisted of radioactive ⁵⁷Co doped into a thin Rh foil. This isotope of Co decays by electron capture to an excited state of ⁵⁷Fe, which then emits the gamma-ray of 14.4 keV that is used for the Mössbauer experiment. Samples of the catalyst for Mössbauer spectroscopy consisted of approximately 65 to 75 mg of crushed material held in a compression holder that exposed a thin disc of material approximately 1.5 cm in diameter and 0.1 cm in thickness to the gamma-ray beam.

Mössbauer data analysis consists of least-squares fitting of the catalyst Mössbauer spectra to various combinations of 2-line quadrupole and 6-line magnetic components. A pure lorentzian line-shape is assumed for the individual peaks in the different components. A minimization of the statistic, χ^2 , is the desired target of the least-squares fitting procedure. Ideally, the value for this parameter should be ~ 1 per channel in the spectrum, or ~ 500 for a fully acceptable fit to the data. From the least squares fitting, various Mössbauer parameters, such as the isomer shift (I.S. in mm/s, relative to the isomer shift of metallic iron at room temperature), the quadrupole splitting (Q.S. in mm/s), full width at half peak height (width in mm/s). and the magnetic hyperfine splitting (H0 in kGauss) are derived for the different quadrupole and magnetic components. The values for these parameters are used to identify the iron-bearing phase that gives rise to the particular component in the spectrum. The area under the peaks in the various

components is then used to quantify the distribution of Fe among the different iron-bearing components in the catalyst.

(b) Mo XAFS spectroscopy:

Molybdenum X-ray absorption fine structure (XAFS) spectroscopy was performed at the K-edge of Mo at $\sim 20,000$ eV at beam-line X-18B of the National Synchrotron Light Source (NSLS) at Brookhaven National Laboratory, Upton, NY. The Mo XAFS spectrum was collected in both absorption and fluorescent geometries using an Ar-filled ionization counter (I_1) and a Lytle detector (I_f), respectively, after the X-rays interacted with the sample. The fluorescent spectra were marginally superior to the absorption spectra. A nitrogen-filled ionization detector was used to determine the intensity of the X-ray beam (I_0) incident on the sample. An energy range from about 200 eV below the Mo K-edge at 20,000 eV to as much as 600 eV above the edge was used for the Mo XAFS spectra. The range in energy was determined by Bragg's law and the angle of rotation of a Si(111) double crystal monochromator. The monochromator was not significantly detuned for the collection of the Mo XAFS spectra as detection of higher harmonic reflection from the silicon crystal is not anticipated to be a serious problem for Mo. Spectrum calibration was provided by a thin foil of Mo metal that was placed in a second absorption experiment after the catalyst experiment. The first major inflection peak (first significant peak in the unsmoothed derivative spectrum of the Mo foil) was used as the calibration point for the catalyst spectra. This peak is assumed to occur at 20,000 eV. Samples of the catalysts for Mo XAFS spectroscopy consisted of crushed material held in thin polypropylene baggies that exposed a thin rectangular aggregate of catalyst, approximately 1.5-2.0 cm in length and 0.5 cm in height, to the X-ray beam. The actual vertical height of the X-ray beam was reduced to 0.1 mm by means of a slit so as not to compromise resolution at the Mo K-edge energy.

Data analysis is initiated by first calibrating the catalyst's Mo XAFS spectrum relative to the zero point of the XAFS spectrum of metallic Mo foil, then normalizing the spectrum to the edge-step, and finally dividing the Mo XAFS spectra into separate X-ray absorption near-edge structure (XANES) and extended X-ray absorption fine structure (EXAFS) regions. As is well described in the literature [1-3], the XANES region is used without further modification as a "fingerprint" of how the Mo exists in the catalyst materials; it largely reflects the oxidation state of the Mo and the immediate bonding of the Mo atom or ion to its nearest neighbor ligands. In contrast, the EXAFS region is converted to a reciprocal space (k-space) representation and weighted by k^3 to yield the $k^3(\chi)$ spectrum. This spectrum is then subjected to a Fourier transform, which converts it to a radial structure function (RSF). Additional processing of both the XANES and EXAFS/RSF spectral regions is then possible. This can take the form of least-squares fitting the unknown catalyst to various combinations of standard XANES or EXAFS spectra of Mo compounds, principal component analysis with standard spectra, or FEFF fitting of individual atom shells in the EXAFS/RSF spectra.

(c) Transmission Electron Microscopy:

Transmission electron microscopy (TEM) was performed on a 200 kV field emission analytical transmission electron microscope (JEOL-2010F) equipped with an Oxford energy-dispersive X-ray spectrometer, a scanning (STEM) unit, and a Gatan imaging filter (GIF) system. The GIF provides both energy-filtered imaging and diffraction and parallel detection EELS. All images

and spectra were recorded with a slow-scan charge coupled device (CCD) camera with a 1024 x 1024 pixel array and processed with Gatan Digital Micrograph software.

The analysis consisted of finding various interesting particles within the catalyst mass of the right thickness for TEM. Particles were then investigated according to one or more of the various analytical methods available on the TEM to the microscopist. Images and spectra were recorded digitally.

Results

(a) Mössbauer spectroscopy:

Mössbauer spectra of all six samples are shown in Figure 1. The spectra vary significantly from sample to sample, although samples 2 and 4 appear very similar to each other, as do samples 1, 3, and 6. Samples 2 and 4 do not contain any magnetic phases, whereas the other four spectra contain a significant fraction of iron in magnetic form. The various components contributing to the spectra are indicated by the 2-line and 6-line diagrams above the spectral data. The magnetic six-line patterns arise from χ and $\acute{\epsilon}$ Fe-carbides, while the central doublet arises from iron oxides. Note that the spectrum of sample 2 is shown at a reduced velocity setting compared to the other spectra. It and the closely similar spectra for sample 4 arise entirely from iron present as ferrihydrite. The results of the data analysis by least-squares fitting for various Mössbauer parameters (I.S. – isomer shift; Q.S. – quadrupole splitting; H_0 – magnetic hyperfine field) are summarized in Table 1.

The data show that the outermost magnetic component has I.S. values between 0.24 – 0.27 mm/s and H_0 values between 213 – 216 kGauss for the four samples that exhibit magnetic components. Such variation is relatively small and not much greater than experimental errors. Although there is reasonable agreement for samples 1 and 3 for the other two inner magnetic components, the same components in samples 5 and 6 show rather more variation, particularly in the hyperfine magnetic splitting parameter. Based on published data for iron carbides [4-6], the magnetic components appear to arise from χ -carbide and $\acute{\epsilon}$ -carbide. Furthermore, an additional component with a large quadrupole splitting has been added to make these fits more statistically robust. It would appear that there is some superparamagnetic (spm) behavior in the carbides in these two samples. Again, similar behavior has been reported previously for iron-based catalysts used in the commercial manufacture of acetonitrile [4] and for Fischer-Tropsch catalysts [5,6]. Samples 2 and 4 do not exhibit any magnetic components; all of the iron in these samples appears to be present as iron oxides, in particular, as ferrihydrite, a small particle iron oxyhydroxide. Mössbauer spectra of similar phases have been described in the literature [7-9], including a Mo-substituted ferrihydrite in which the Mo was located at the particles' surfaces as the molybdate anion (MoO_4^{2-}) [10].

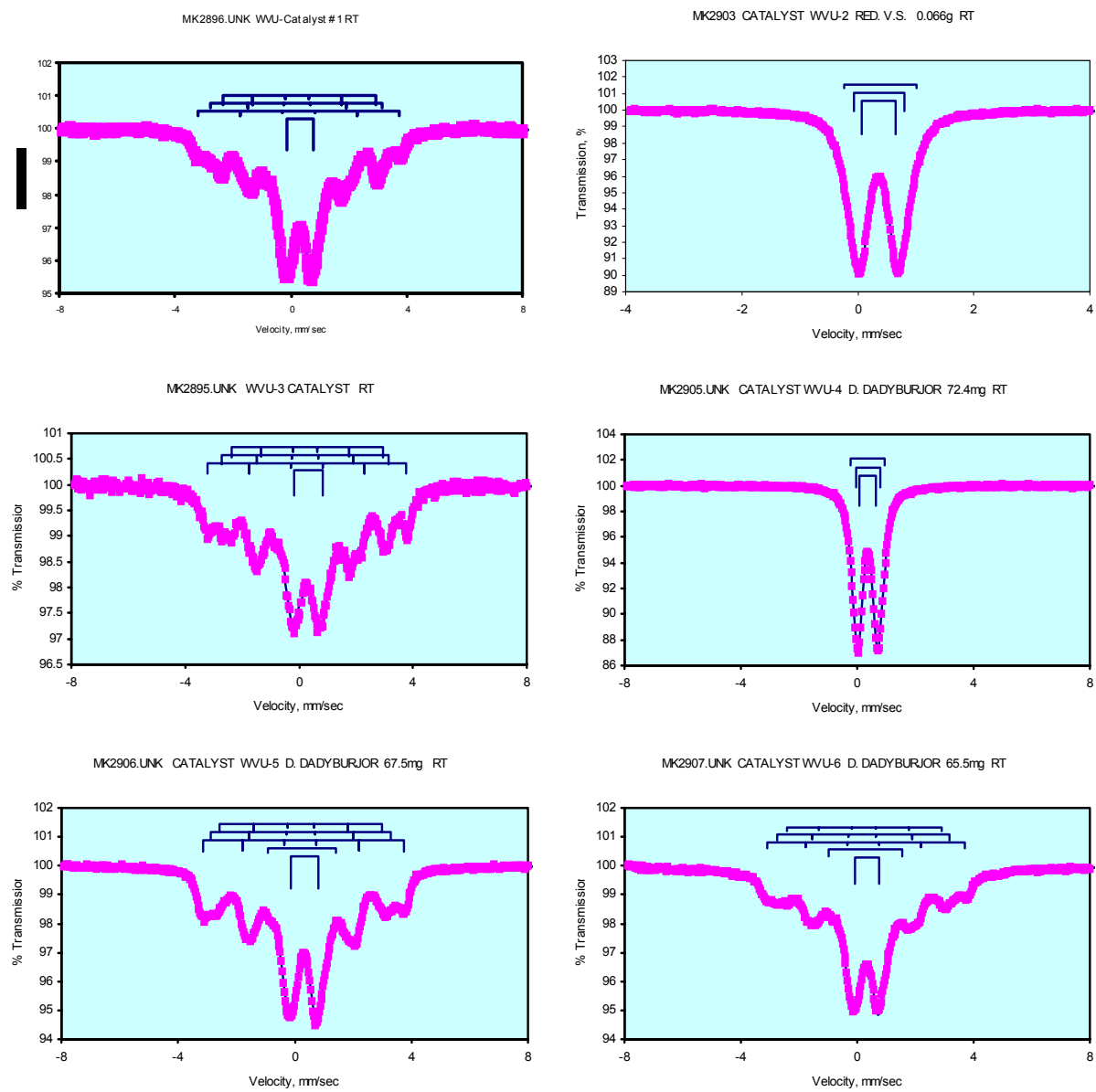


Figure 1: Mössbauer spectra of the six Fe-Mo catalyst samples received from Dr. Dadyburjor.

Table 1: Results of Mössbauer Least-squares Fitting of Fe-Mo Catalyst Samples

<u>Spectrum</u>	<u>Comp.¹</u>	<u>I.S.</u>	<u>Q.S.</u>	<u>H₀</u>	<u>Width</u>	<u>%Fe</u>	<u>I.D.</u>
		mm/s	mm/s	kGauss	mm/s		
MK2896	1 QS	0.33	0.92		0.81	56	Fe ³⁺ Oxide
WVU-1	1 H0	0.26	0	215	0.49	13	χ-carbide
	2 H0	0.22	-0.01	183	0.51	14	χ-carbide
	3 H0	0.25	0.04	165	0.36	17	é, χ-carbide
MK2903	1 QS	0.36	0.59		0.33	60	Ferrihydrite
WVU-2	2 QS	0.36	0.87		0.33	33	Ferrihydrite
	3 QS	0.38	1.25		0.33	7	Ferrihydrite
MK2895	1 QS	0.34	0.99		1.05	49	Fe ³⁺ Oxide
WVU-3	1 H0	0.27	0	216	0.5	23	χ-carbide
	2 H0	0.21	0	182	0.37	14	χ-carbide
	3 H0	0.25	0.04	165	0.36	14	é, χ-carbide
MK2905	1 QS	0.36	0.59		0.33	55	Ferrihydrite
WVU-4	2 QS	0.37	0.83		0.33	35	Ferrihydrite
	3 QS	0.37	1.16		0.33	10	Ferrihydrite
MK2906	1 QS	0.34	0.94		0.69	45	Fe ³⁺ Oxide
WVU-5	2 QS	0.25	2.35		0.69	6	spm carbide?
	1 H0	0.24	0.04	213	0.45	22	χ-carbide
	2 H0	0.22	0	191	0.36	11	χ-carbide
	3 H0	0.22	0.01	173	0.42	16	é, χ-carbide
MK2907	1 QS	0.32	0.88		0.70	52	Fe ³⁺ Oxide
WVU-6	2 QS	0.15	3.16		0.70	8	spm carbide?
	1 H0	0.25	0.06	213	0.40	10	χ-carbide
	2 H0	0.25	0	174	0.83	30	é, χ-carbide

¹Quadrupole components are indicated as QS; magnetic components as H0.

(b) Mo XAFS spectroscopy:

Mo K-edge XAFS spectra were recorded and divided into separate XANES and EXAFS regions. The XANES region spectral data are shown in Figure 2. They consist of an abrupt edge that reflects the Mo 1s (K-edge) absorption process to the continuum upon which various peaks are superimposed that arise from electronic and other transitions within individual Mo atoms. The most obvious feature is the relatively sharp inflection point that occurs about half-way up the absorption edge; it is most prominent for samples 2 and 4, but is present, albeit somewhat less obviously, in all other samples as well. This feature is characteristic of the Mo(VI) oxidation state, especially the molybdate anion species, MoO₄²⁻. Other peaks occur on top of the absorption edge; as shown in Figures 3 and 4, there are a minimum of three peaks that contribute to the edge structure, up to about 70 eV above the absorption edge.

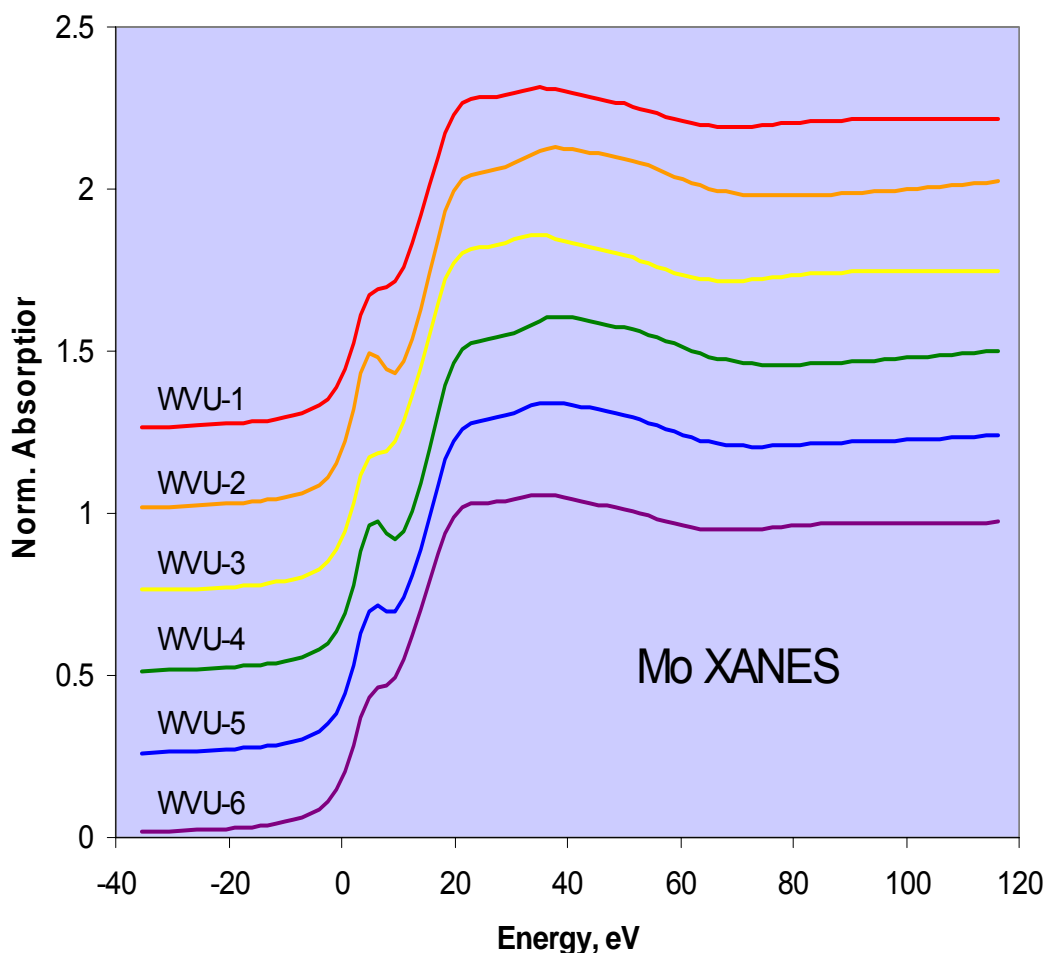


Figure 2: Mo XANES spectra of the six Fe-Mo catalysts from Dr. Dadyburjor, WVU.

There are systematic changes that occur with the 4 individual peaks upon comparing the XANES spectra. These are best demonstrated and quantified by least-squares fitting of the XANES spectra, according to the fitting model shown in Figures 3 and 4, and detailing the variation of the parameters derived from the least-squares analysis. These data are summarized in Table 2 and will be discussed in the subsequent section of this report.

Attempts were made to analyze the EXAFS/RSF region as well; but to date these have not been too successful. It is not clear why the EXAFS region is so recalcitrant in releasing information for the $k^3(\chi)$ spectra did not appear overly complex. Most RSF showed a phase-shift uncorrected peak at about 1.35 – 1.40 Å; such a peak is consistent with the Mo-O bonds in molybdate anions. However, there were a number of large apparently spurious peaks in the RSF spectra making more detailed analysis impossible.

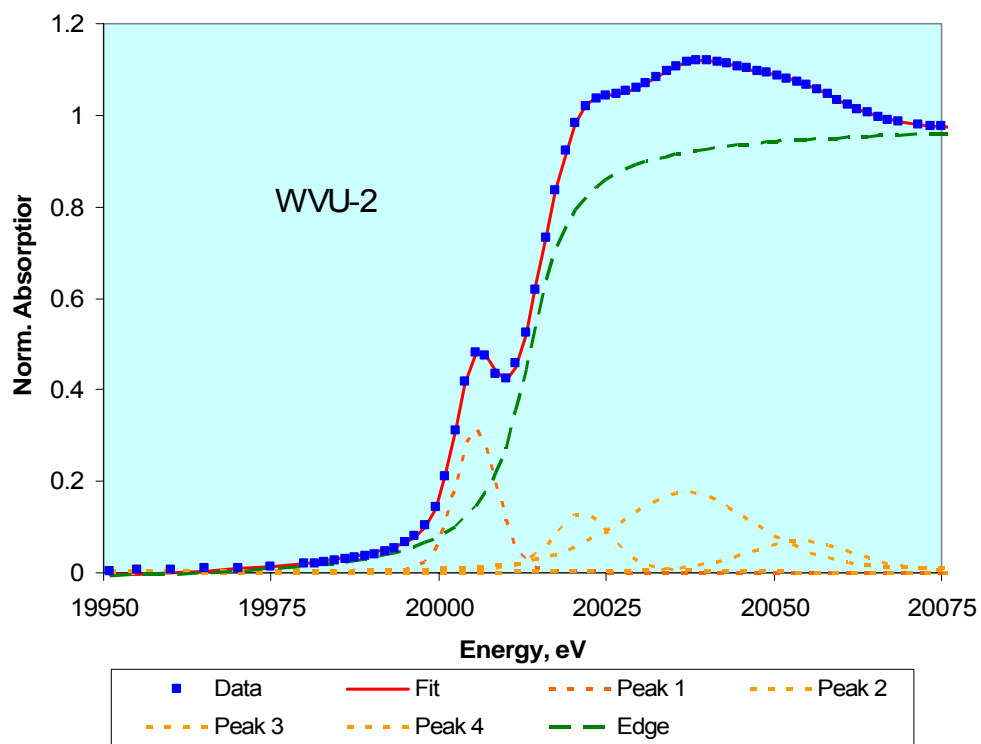


Figure 3: Least-squares fitted Mo XANES spectrum of catalyst sample WVU-2.

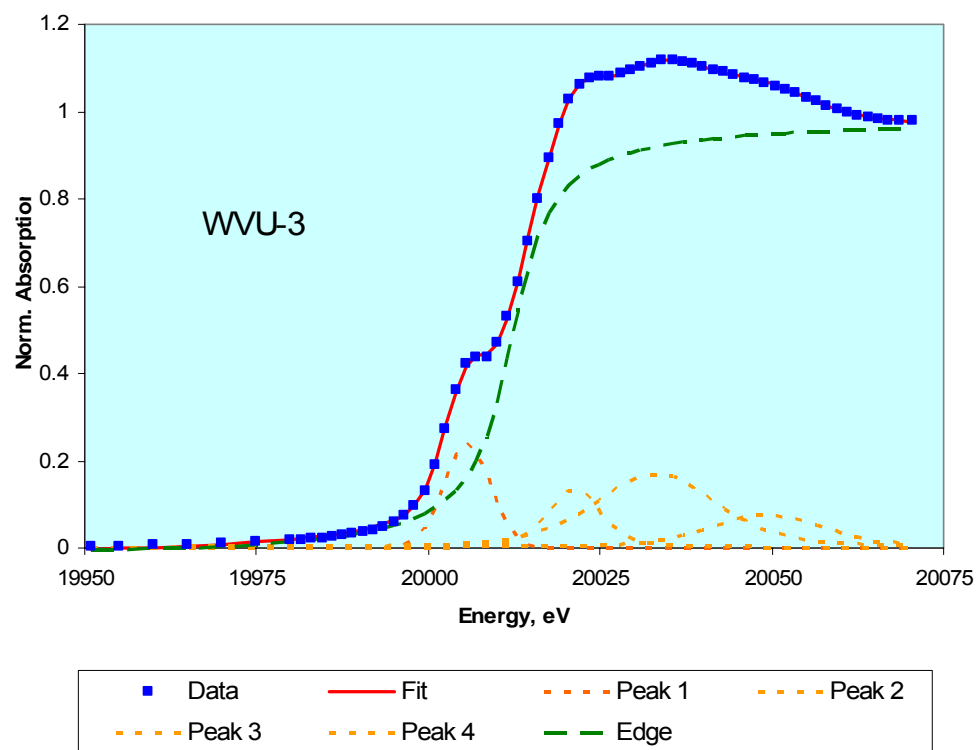


Figure 4: Least-squares fitted Mo XANES spectrum of catalyst sample WVU-3.

Table 2: Results from Least-Squares Analysis of Mo XANES of 6 samples from Dr. Dadyburjor

	<i>MOCAT.157A</i> <i>WVU-1</i>	<i>MOCAT.160A</i> <i>WVU-2</i>	<i>MOCAT.163A</i> <i>WVU-3</i>	<i>MOCAT.166A</i> <i>WVU-4</i>	<i>MOCAT.169A</i> <i>WVU-5</i>	<i>MOCAT.172A</i> <i>WVU-6</i>
Total Area	65.76	73.94	65.63	73.57	70.32	64.6
1. Height	0.265	0.315	0.239	0.307	0.282	0.26
1. Position	6.05	5.54	5.67	5.92	5.9	5.8
1. Width	8.5	7.34	7.91	7.37	7.77	8.37
1. Area	2.42	2.61	2.01	2.54	2.345	2.32
2. Height	0.127	0.131	0.133	0.135	0.115	0.132
2. Position	21.4	21.4	21.4	21.8	21.6	21.3
2. Width	9.94	9.94	9.06	10.1	9.13	9.7
2. Area	1.6	1.66	1.545	1.74	1.34	1.625
3. Height	0.147	0.176	0.17	0.179	0.1655	0.159
3. Position	34.1	36.9	33.1	37.16	34.9	33.6
3. Width	22.8	24.6	20.8	24.2	24.3	22.15
3. Area	4.06	5.23	4.315	5.235	4.865	4.26
4. Height	0.05	0.071	0.076	0.072	0.069	0.062
4. Position	50.8	53.7	49.2	54.2	51.4	50.4
4. Width	18.3	19.1	20.1	19.35	19.8	19.6
4. Area	1.08	1.625	1.8	1.66	1.63	1.422
Edge Height	1.02	1.015	1.013	1.013	1.019	1.016
Edge Position	12.18	13.5	12.1	13.8	12.9	12.3
Edge Width	13.5	15	13.6	14.9	14.45	13.53
Edge Area	59.7	66.8	59.34	66.4	63.89	58.13
% Area Peak 1	3.7	3.5	3.1	3.5	3.3	3.6
% Area Peak 2	2.4	2.2	2.4	2.4	1.9	2.5
% Area Peak 3	6.2	7.1	6.6	7.1	6.9	6.6
% Area Peak 4	1.6	2.2	2.7	2.3	2.3	2.2
% Area Edge	86.1	85.0	85.3	84.8	85.5	85.1

N.B. All positions are given relative to the zero-point of energy at 20,000 eV.

(c) Transmission Electron microscopy:

A brief TEM investigation was conducted on samples WVU-1 and WVU-2 as these two samples appeared to differ the most according to the spectroscopic data. Some observations made with the TEM, based on the micrographs and the EDS and EELS spectra shown in Figures 5-10, are described.

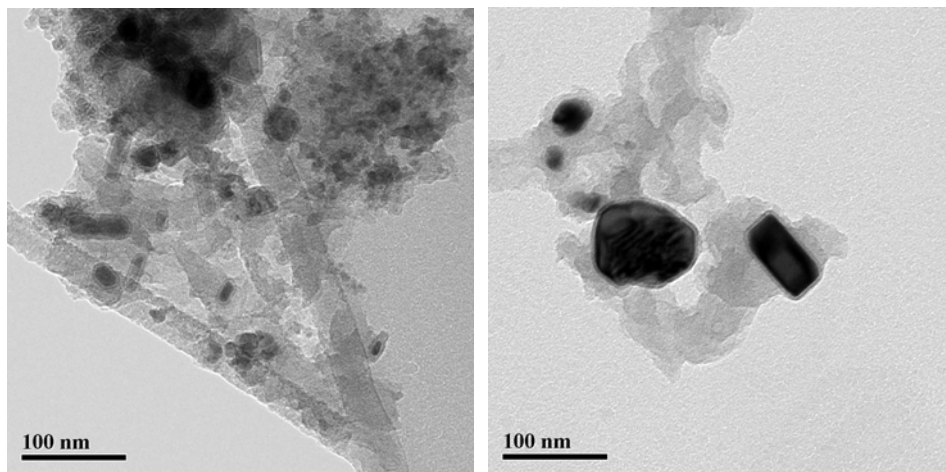


Figure 5: TEM micrograph of WVU-1 catalyst particles.

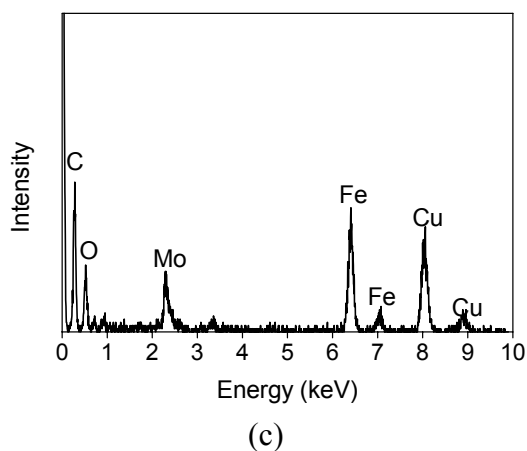
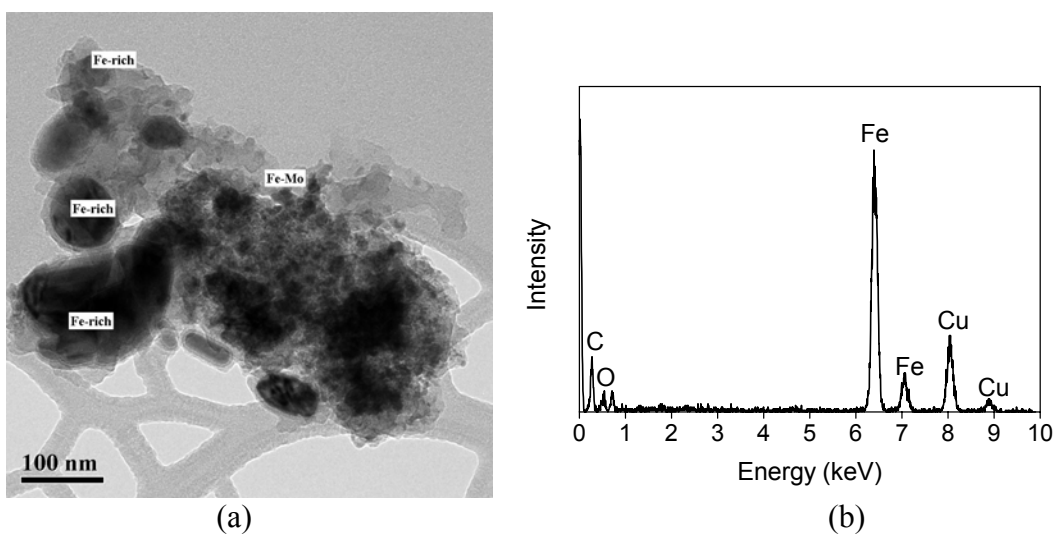


Figure 6: (a) TEM micrograph of Fe-rich and Fe-Mo catalyst particles. (b) EDS spectrum recorded from the Fe-rich particles. (c) EDS spectrum recorded from the Fe-Mo particles. Cu peaks are from TEM grids.

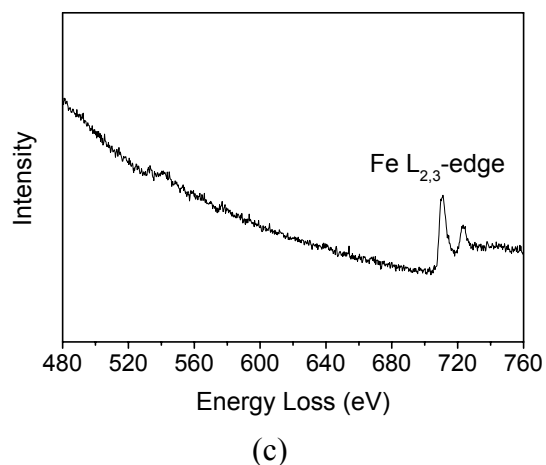
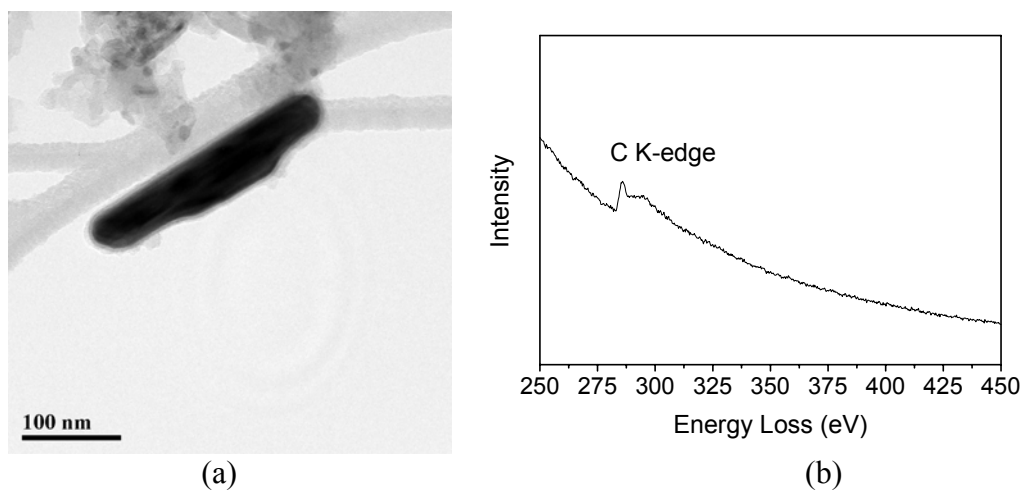


Figure 7: TEM micrograph (a), carbon K-edge (b) and iron L-edge EELS spectrum (c) of a rod-like iron carbide particle.

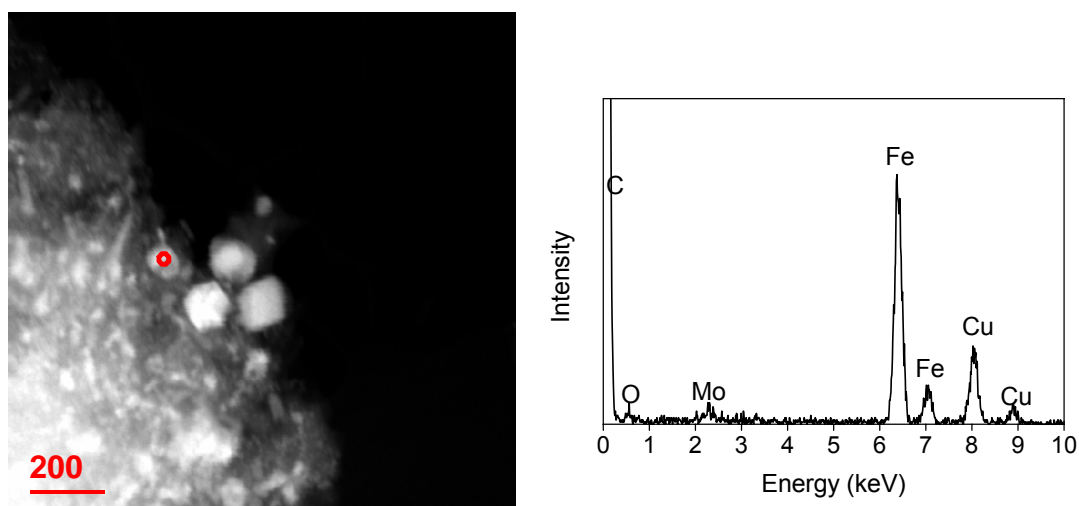


Figure 8, left: HAADF (high-angle annular dark-field) image of several Fe-Mo catalyst particles; right: EDS spectrum recorded from the particle indicated by the red spot. Cu peaks are from TEM grids.

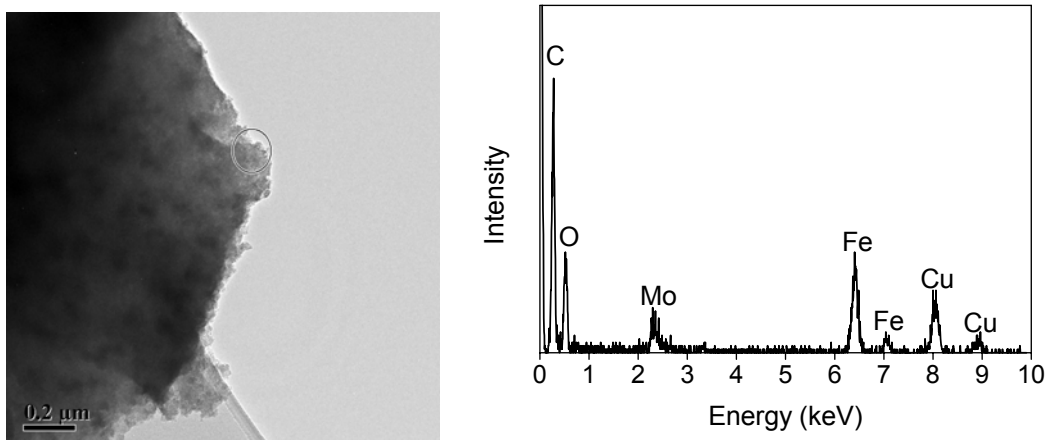


Figure 9. Sample WVU-2: left: TEM micrograph of a large carbonaceous particle; right: EDS spectrum recorded from the circled region shown in left image shows C, Fe, Mo and O peaks. Cu peaks are from TEM grids.

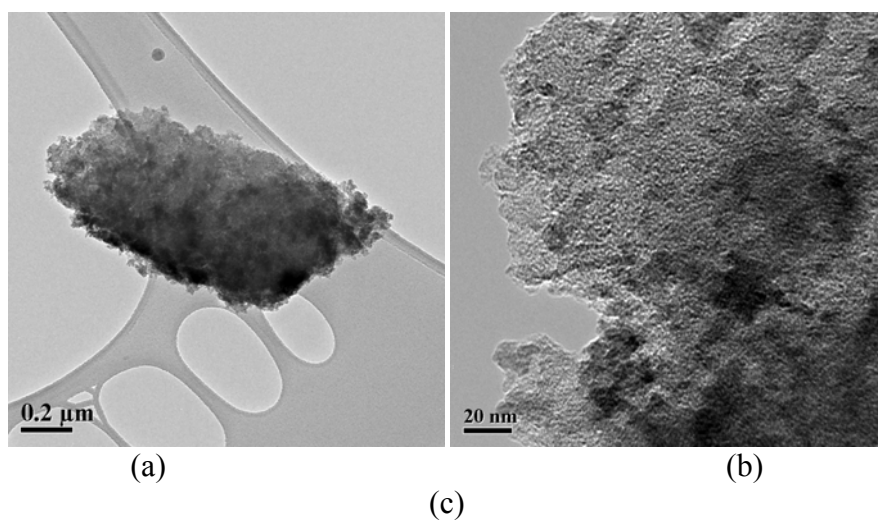


Figure 10: (a) low-mag. TEM micrograph, (b) higher-mag. TEM micrograph, and (c) EDS spectrum of a carbonaceous particle. Fe and Mo signals can be detected from the carbonaceous matrix. However, it seems that separate catalyst particles haven't fully developed.

The catalyst particles in sample WVU1 have typical sizes varying from 15-150 nm. Iron tends to exist in the form of separate crystals with larger sizes, while Mo tends to exist in the form of smaller aggregated particles. Both Fe-rich and Fe-Mo mixed catalyst particles have been observed. Many of the catalyst particles seem to be in the form of carbides.

The catalyst particles in sample WVU2 seem not to be very well developed. Carbonaceous supports have been observed that contain both Fe and Mo (probably in the form of salt?).

Discussion

The samples divide clearly into two distinct sets of samples: set 1, consisting of WVU-2 and WVU-4, and set 2 consisting of WVU-1, WVU-3, WVU-5 and WVU-6. As indicated by the Mössbauer data, Figure 11, the former set of samples do not contain any iron carbides, whereas the latter set of 4 samples contain significant iron carbide.

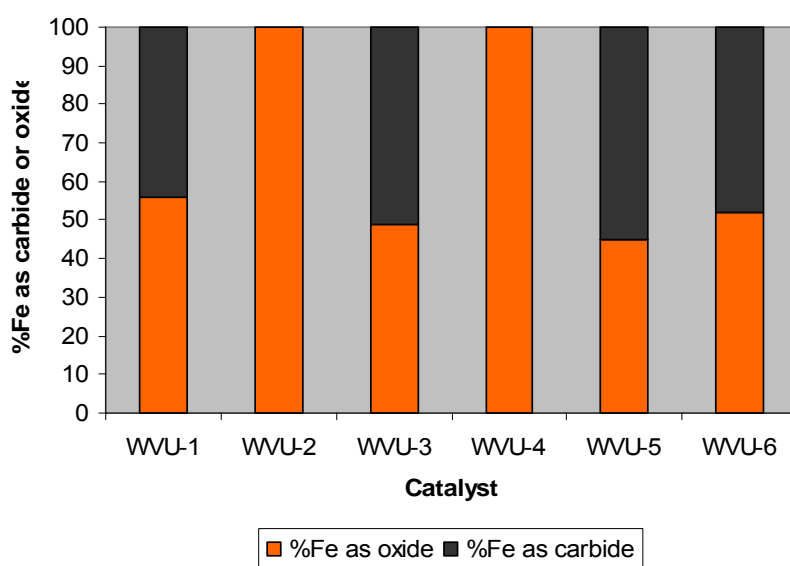


Figure 11: Histogram showing the distribution of Fe between oxide and carbide forms for the six samples, as obtained from the Mössbauer data.

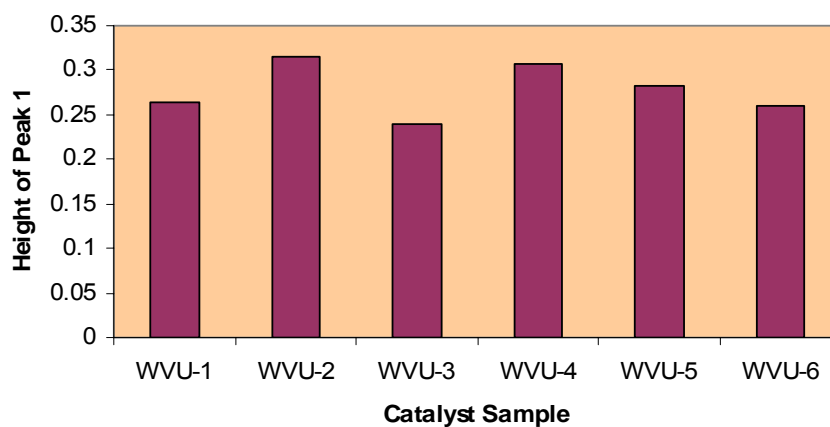


Figure 12: Histogram of the height of peak 1 for the six catalyst samples normalized to the edge step, as obtained from the Mo XAFS data.

A similar separation is also apparent in the Mo XAFS data. Figure 12 shows the height of the inflection peak (peak 1) relative to the edge step. Samples 2 and 4 have significantly more height (and resolution – q.v. Figure 4) for Peak 1 than the other four samples. A very similar separation can also be seen in Figure 13, which shows the variation among the six catalyst samples in the positions of the four least-squares fitted peaks. Data for peaks 2 and 4 occur at distinctly higher energy than for the other four samples. Sample 5 appears transitional on the basis of the Mo XAFS data.

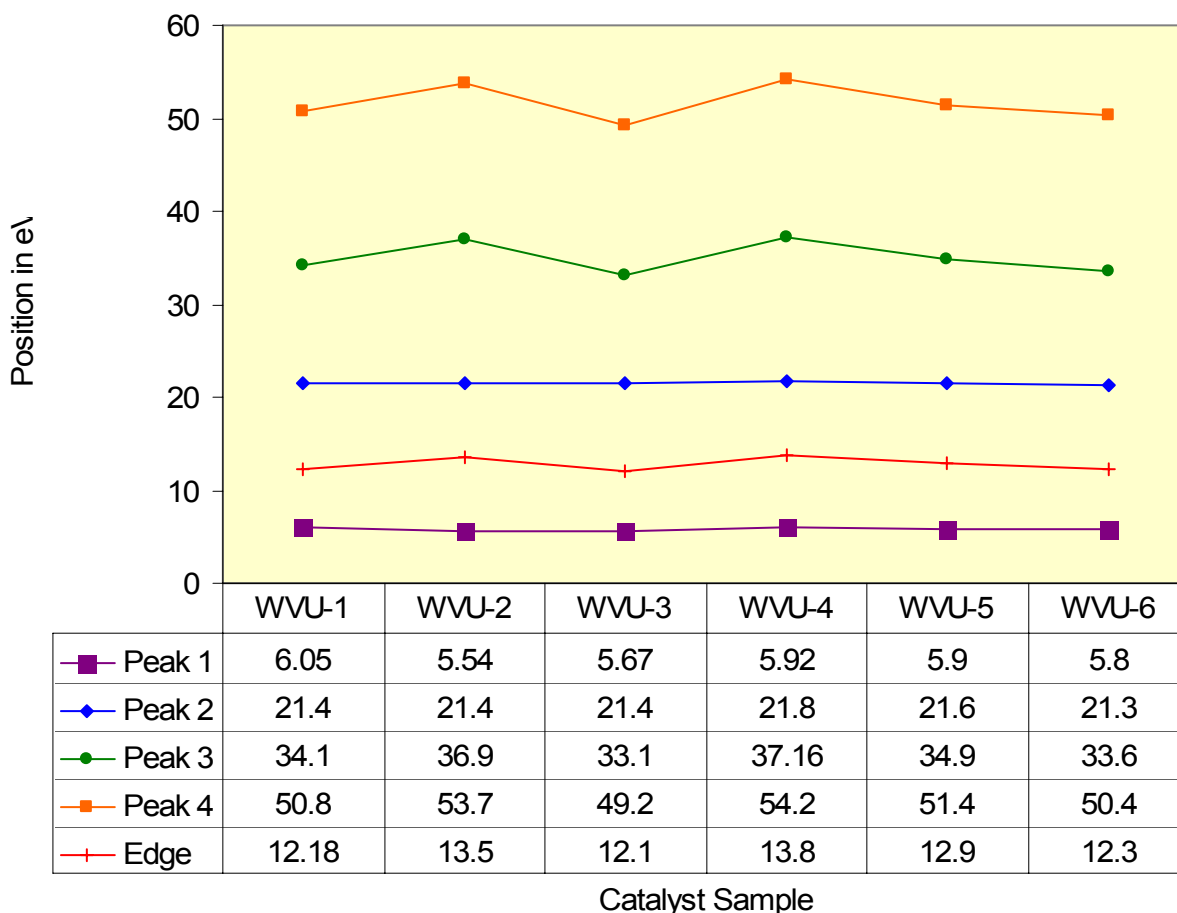


Figure 13: Variation of peak position in eV, relative to the Mo K-edge at 20,000 eV, of the four least-squares fitted peaks (q.v. Figures 3 and 4) in the Mo XANES region. Note that the peak positions of Peaks 3 and 4 and the edge are shifted to higher energy compared to the positions of the same peak for the other four samples. As before, data for sample WVU-5 appears to be transitional.

Both the Mössbauer and XAFS data indicate that samples WVU-2 and WVU-4 are significantly different to the other four samples. The data for the K edge position and for peaks in the Mo XANES spectra suggest that the Mo oxidation state is, on average, higher (principally as Mo(VI) in molybdate) in WVU-2 and WVU-4 than in the other four samples, which appear to be a mixture of Mo(VI) and Mo(IV). Similarly, the Mössbauer data indicate that the iron oxidation state is entirely Fe³⁺ for samples WVU-2 and WVU-4, but a mixture of Fe³⁺ (in oxide forms) and

Fe⁰ (in carbide forms) for the other four samples. Hence, we conclude that samples WVU-2 and WVU-4 represent largely unreacted catalyst materials, in which the formal oxidation states of Fe and Mo are +3 and +6, respectively. The other four samples represent samples that have been exposed to the WGS reaction and have been partially converted to mixtures of iron and molybdenum carbides. The question of whether the Mo and Fe are present in the same carbide or oxide phase or form distinct carbide and oxide phases is less clear. The preliminary TEM study was inconclusive; Mo-free Fe-rich particles, Fe-free Mo particles, and some Fe-Mo mixed particles were observed. Similarly, the Mössbauer parameters for the ferrihydrite phase in samples WVU-2 and WVU-4 appear quite similar to those in 100% Fe systems, as do the Mössbauer parametric data for the carbides in the other four samples. However, the oxide phase has clearly changed between the two sets of samples; the simple apparent 2-peak spectrum in samples WVU-2 and WVU-4 has clearly given way to something more complex with significantly different Mössbauer parameters (slightly lower isomer shift and larger average quadrupole splitting) suggesting that the ferrihydrite phase may be undergoing a transformation to superparamagnetic iron oxides before being reduced to carbide.

References:

- [1] G.E. Brown, Jr., G. Calas, G.A. Waychunas and J. Petiau, in: F.C. Hawthorne (Ed.), **Spectroscopic Methods in Mineralogy and Geology**; Rev. in Mineral. Vol. 18, Mineralogical Society of America, Washington, DC, 1988, Chapter 11, pp. 431-512.
- [2] P.A. Lee, P.H. Citrin, P. Eisenberger and B.M. Kincaid, **Rev. Mod. Phys.** 53 (1981) 769-808.
- [3] D.C. Koningsberger and R. Prins, **X-ray Absorption. Principles, Applications, Techniques of EXAFS, SEXAFS, and XANES**, J. Wiley & Sons, New York, 1988.
- [4] M.V. Badani and W.N. Delgass, *The active phase of iron catalysts for acetonitrile synthesis.* **J. Catalysis** 187 (1999) 506-517.
- [5] K.R.P.M. Rao, F.E. Huggins, G.P. Huffman, R.J. Gromley, R.J. O'Brien, and B.H. Davis, *Mössbauer study of iron Fischer-Tropsch catalysts during activation and synthesis.* **Energy & Fuels** 10 (1996) 546-551.
- [6] K.R.P.M. Rao, F.E. Huggins, V. Mahajan, G.P. Huffman, V.U.S. Rao, B.L. Bhatt, D.B. Bukur, B.H. Davis, and R.J. O'Brien, *Mössbauer spectroscopy study of iron-based catalysts used in Fischer-Tropsch synthesis.* **Topics in Catalysis**, 2 (1995) 71-78.
- [7] U. Schwertmann and U. Cornell, **Iron oxides in the laboratory.** VCH, Weinham, Germany, 1991.
- [8] E. Murad, and U. Schwertmann, *The Moessbauer spectrum of ferrihydrite and its relations to those of other iron oxides.* **American Mineralogist**; 65 (1980) 1044-1049.
- [9] J. Zhao, F.E. Huggins, Z. Feng, and G.P. Huffman, *Surface-induced superparamagnetic relaxation in nanoscale ferrihydrite particles.* **Phys. Rev B.** 54 (1996) 3403-3407.
- [10] J. Zhao, Z. Feng, F.E. Huggins, N. Shah, G.P. Huffman, and I. Wender, *Role of molybdenum at the iron oxide surface.* **J. Catalysis**, 148 (1994) 194-197.

HYDROGEN PRODUCTION FROM METHANOL IN SUPERCRITICAL WATER

Jayant B. Gadhe and Ram B. Gupta

Department of Chemical Engineering
Auburn University
Auburn, AL 36849-5127.

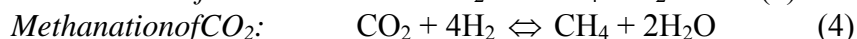
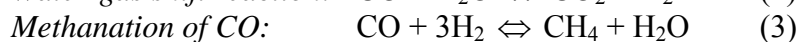
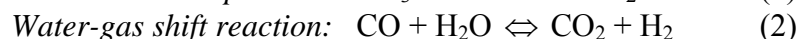
Introduction

The development of proton exchange membrane fuel cells for various transportation applications has resulted in a need of on-board and stationary reformers which can supply high purity hydrogen at low cost. Designing a process to produce H₂ at a very high pressure is an attractive approach for mobile and portable applications owing to its low storage volume. The reforming of hydrocarbons can be carried out in the presence of supercritical water instead of steam as used in the conventional processes, to produce H₂ at a very high pressure.

There are several advantages of carrying out the reforming reactions in supercritical water over the conventional processes. The density of supercritical water is higher than that of steam which results in a high space-time yield and the higher values of thermal conductivity and specific heat of supercritical water are beneficial for the endothermic reforming reaction. H₂ is available at a high pressure which can be stored directly, thus avoiding the problems associated with its compression. The process becomes economical as the compression work is reduced owing to the low compressibility of liquid feed as compared to that of gaseous H₂.¹

Hydrocarbons are completely soluble in supercritical water which minimizes the formation of char or slag which may otherwise cause catalyst deactivation. This is particularly important in the generation of H₂ from heavy oils such as diesel. The generation of H₂ by the steam reforming of biomass leads to the formation of significant amounts of tar and char which limits the yield of H₂ and the gaseous product contains higher hydrocarbons in addition to the desired light gases. Researchers have carried out the catalytic gasification of biomass or its model compounds in supercritical water to produce H₂-rich gas with effectively no tar or char formation.²

Methanol is chosen as feedstock for reforming because of its high hydrogen-to-carbon ratio and absence of carbon-carbon bonds. It is in the liquid state under normal conditions and hence can be stored and pumped easily. The major reactions involved in the methanol reforming are:



To study the impact of pressure on the H₂ yield, equilibrium calculations were performed using Gibbs free energy minimization method and Peng-Robinson equation of state. **Figure 1** shows that as pressure increases, there is an increase in the CH₄ moles and decrease in the H₂, CO and CO₂ moles. It suggests that methanation of CO (reaction 3) and CO₂ (reaction 4) is favored at higher pressures. Methanation of CO results in a loss of 3 moles of H₂ while methanation of CO₂ results in a loss of 4 moles of H₂. To enjoy the benefits of the reforming of

methanol in supercritical water which are mentioned before, it becomes important to prevent the loss of H₂ by minimizing the methanation reactions.

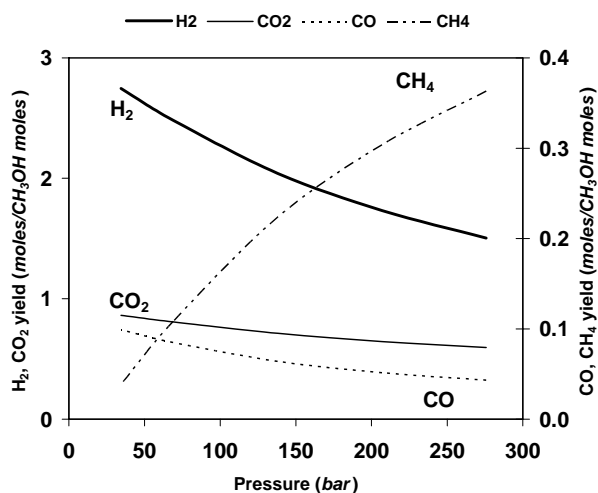


Figure 1. Dependence of gas yield on pressure using ASPEN+ equilibrium calculations. (10 wt.% methanol, 700 °C)

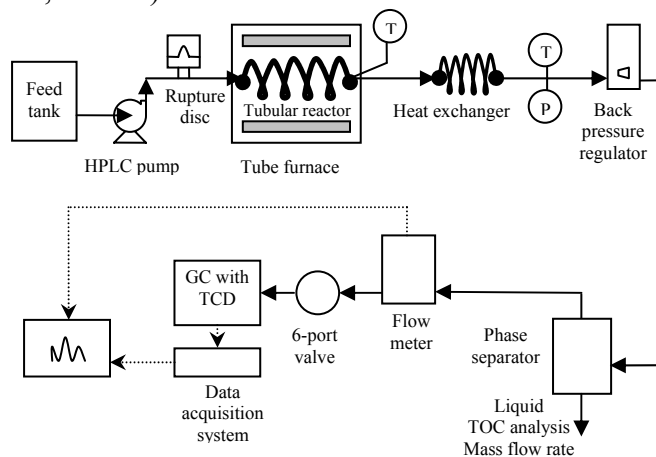


Figure 2. Schematic of the experimental setup used for methanol reforming in supercritical water.

Experimental

Materials. Methanol (99.9%), KOH (88.7% assay) and K₂CO₃•1½H₂O (99.9% assay) were obtained from Fisher.

Apparatus. Figure 2 shows schematic of the apparatus used in the study. A tubular reactor made of Inconel 600 (Microgroup) having a composition of 73% Ni, 18% Cr, 9% Fe was used. The reactor wall provides the catalytic surface area for the reactions. Later the reactor was replaced with a Ni-Cu tubing (Supelco) having a composition of 67% Ni, 33% Cu.

Aqueous methanol from the feed tank was pumped to the reactor using an HPLC pump (Waters 590). The reactor was heated using a tube furnace equipped with a temperature controller (Thermolyne 21100). The gas mixture exiting the reactor was cooled using an air-

cooled heat exchanger made of SS 316 tubing. Pressure was measured by a pressure gauge P. The pressure was let down to the ambient by means of a back pressure regulator (Straval). The gas-liquid mixture was separated in a glass phase separator having gas tight valves to prevent the escape of gases. The gas flow rate was measured using a gas flow meter (Omega FMA-1600). A six-port injection valve (Valco) having a 100 μ L sample loop was used for the online sample injection. The gas composition was measured using a gas chromatograph (Varian 3700) equipped with a TCD and 60/80 Carboxen-1000 carbon molecular sieve column. (Supelco) The mass flow rate of the liquid coming out of the phase separator was measured using a balance. The total organic carbon (TOC) content of the liquid was analyzed using a TOC analyzer (OI Analytical Model 700).

Results and Discussion

Figure 3 shows that as pressure is raised from 34 to 276 bar, the H₂, CO and CO₂ moles decrease while the CH₄ moles increase as anticipated, suggesting that the methanation reactions, of both CO and CO₂ are favored at the higher pressures. The H₂ yield (H₂ moles/ CH₃OH moles) has dropped from 2.75 at 34 bar to 1.50 at 276 bar. The increase in density at the higher pressures leads to an increase in the residence time which ranged from 7 seconds at 34 bar to 59 seconds at 276 bar which resulted in the near-equilibrium yields.

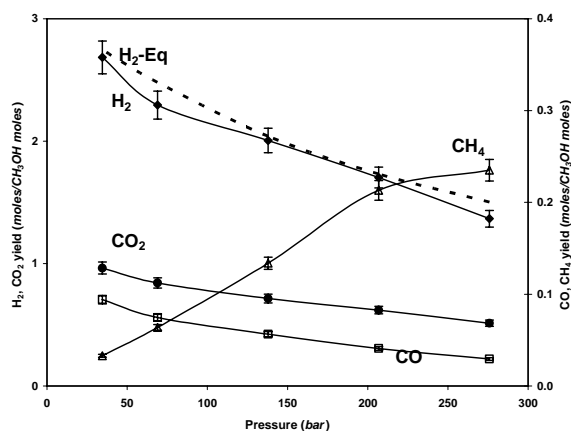


Figure 3. Effect of pressure on gas yield. (10 wt.% methanol, 0.5 mL/min, 700 °C, reactor length = 2 m)

The pressure variation was studied again in the Ni-Cu reactor at a lower residence time. **Figure 4** shows that the increase in pressure has a very little effect on the gas yields in this case. The H₂ yields which are higher than the equilibrium H₂ yields, remain fairly constant over the entire pressure range. The CH₄ yield is found to be almost negligible. This could be the combined effect of the low residence time, which ranged from 2 seconds to 17 seconds in this case and possibly the catalytic activity of the Ni-Cu reactor.

This behavior of the Ni-Cu reactor can be explained based on the mechanism of CO methanation. It proceeds via dissociative chemisorption of CO and H₂ to form intermediates which combine to form CH₄ as shown in reactions 5 to 7.



Alloying Ni with Cu results in the dilution of active Ni in an inactive matrix which diminishes the number and size of Ni clusters which are necessary for the dissociation of CO and deposition of C_s on the surface. The Ni-Cu tubing reduces the number of places where C_s can be formed and held and decreases the extent of methanation of CO and CO₂.³

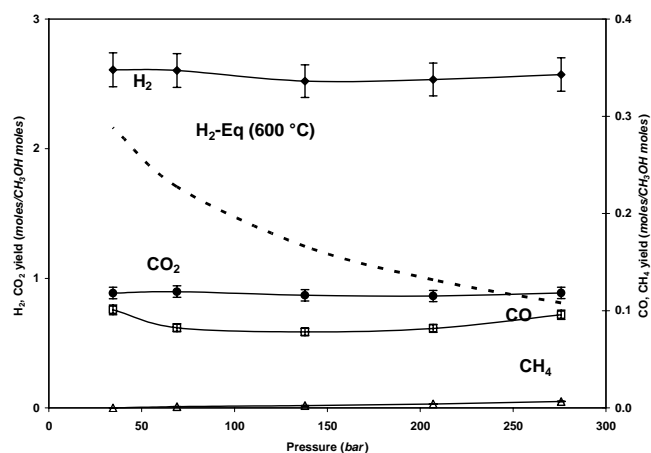


Figure 4. Effect of pressure on gas yield with Ni-Cu reactor. (10 wt.% methanol, 1 mL/min, 600 °C, reactor length = 1 m)

The performance of the Inconel 600 reactor can be improved by adding K₂CO₃ or KOH in aqueous methanol. **Figure 5** shows the increase in the H₂ yield and the decrease in the CH₄ yield.

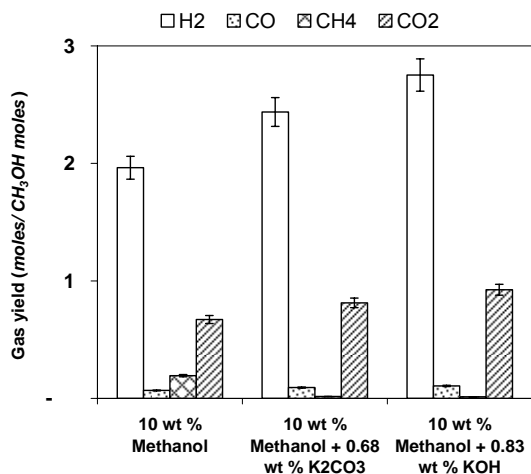


Figure 5. Effect of K₂CO₃ and KOH addition. (10 wt.% methanol, 1 mL/min, 700 °C, reactor length = 2 m)

Conclusions

CH₄ formation during reforming of methanol in supercritical water can be suppressed by (1) operating at a low residence time, (2) using Ni-Cu reactor or (3) adding K₂CO₃ or KOH in the feed.

References

1. Boukis, N.; Diem, V.; Habicht, W.; Dinjus, E. *Industrial & Engineering Chemistry Research* **2003**, 42(4), 728-735.

2. Antal, Michael Jerry, Jr.; Allen, Stephen Glen; Schulman, Deborah; Xu, Xiaodong; Divilio, Robert J. *Industrial & Engineering Chemistry Research* **2000**, 39(11), 4040-4053.
3. Araki, M.; Ponec, V. *Journal of Catalysis* **1976**, 44(3), 439-48.

Coproduction of Hydrogen and Chemicals by decomposition of methanol

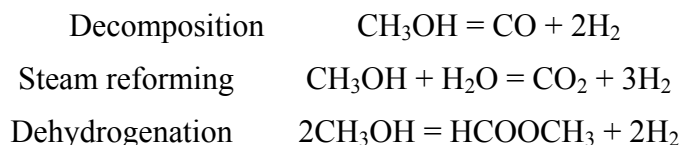
F. Shi, Y. Zhang, J. W. Tierney and I. Wender

Department of Chemical Engineering, University of Pittsburgh

Introduction

Methanol is produced in huge amounts from synthesis gas derived chiefly from natural gas. In 2003 world capacity for methanol production was over 50 million tons. Very large plants are being built near resources of cheap natural gas. Methanol is a hydrogen-rich liquid, and provides a great deal of convenience in storage, transport and handling as a source of hydrogen.

Hydrogen can be generated from methanol in several ways:



Dehydrogenation of methanol produces hydrogen as well as methyl formate (MF). MF has been proposed as a building block for chemicals. It is a stable liquid and can be catalytically converted to important chemicals including dimethyl formamide, formamide, ethylene glycol, acetic acid, dimethyl carbonate and formaldehyde.¹⁻⁴

Since MF is an intermediate in a series of reactions, fast desorption and diffusion are essential for high selectivity to MF and hydrogen. In this study, work has started on the gas phase dehydrogenation of methanol to produce hydrogen and MF on a series of copper-based catalysts. The effects of supports and promoters are under investigation. The formation of hydrogen via steam reforming is also of interest.

Experimental

Catalyst preparation. A series of copper-based catalysts were prepared by incipient wetness impregnation of aqueous $\text{Cu}(\text{NO}_3)_2$ solution onto various supports: a zeolite (ZSM-5), Al_2O_3 , and MgO . The impregnated samples were dried at 110°C for at least 8 hours prior to calcination at 350°C in air for 3 h. Catalysts were pelletized to 60-80 mesh for testing. Before reaction, catalysts were reduced at 250°C with 70 ml/min H_2/Ar (5:2) gases for 3 h.

Catalyst testing. The equipment shown as Figure 1 was built for testing the dehydrogenation and the steam reforming of methanol. Temperature, flow rate and sampling procedure are programmable. The reactor is a U-shape quartz microreactor with maximum 2 ml catalyst loading. Liquid methanol is fed using a syringe pump (100DX, ISCO). In this study, 0.6 to 0.8 g catalyst is loaded and reduced at 250°C with 70 ml/min H_2/Ar (5:2) gases for 3 h. Methanol is fed at the rate of 3 ml/h. The feed is evaporated at 150°C and mixes with 20 ml/min of Ar preheated to the same temperature. Gas lines before entering the microreactor and the GC are heated to 150°C with electrical tapes. Products are analyzed by two on-line Hewlett Packard GCs: one equipped with a TCD detector and with a Carbonsphere packed column (6 feet, 3/8 in) for analysis of H_2 , CO , CH_4 , CO_2 ; another is equipped with a FID and HP-5 capillary column for analysis of methanol, methyl formate, dimethyl ether and other organic products. Liquid products are also collected with a cold trap at -80°C and then are analyzed using GC-MS.

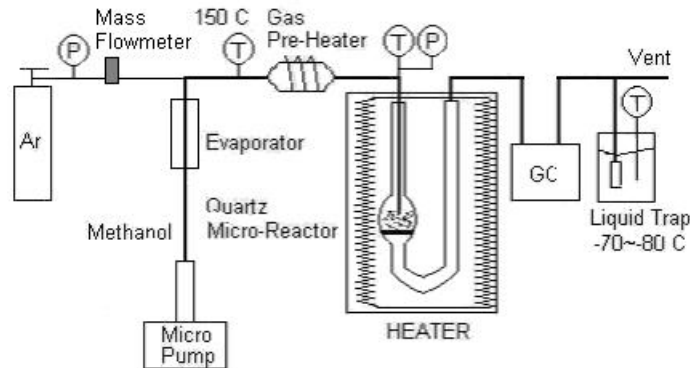


Figure 1 A Schematic of Methanol Dehydrogenation Apparatus

Results and Discussion

Properties of Catalysts: BET surface areas were measured by an ASPS-2010 Analyzer (MicroMeritics) using a liquid nitrogen adsorption method. Results are summarized in Table 1.

Table 1 A Summary of BET surface area of catalysts*

Catalysts	BET Surface Area, m ² /g
Cu/ZSM-5	307.4
Cu/Al ₂ O ₃	110.5
Cu/MgO	47.3

* 10 wt% Cu for each catalyst

Thermodynamic calculations: Thermodynamic calculations for methanol dehydrogenation and steam reforming (methanol/water=1) have been conducted using ASPEN Plus 12, based on a Gibbs free energy minimization method. Results for hydrogen and MF production are shown in Figure 2. At temperatures below 200°C, methanol dehydrogenation to MF and hydrogen is favored; at temperatures above 300°C, complete decomposition of methanol to H₂ and CO dominates. Although steam reforming can produce more hydrogen than methanol dehydrogenation, it decreases the formation of MF.

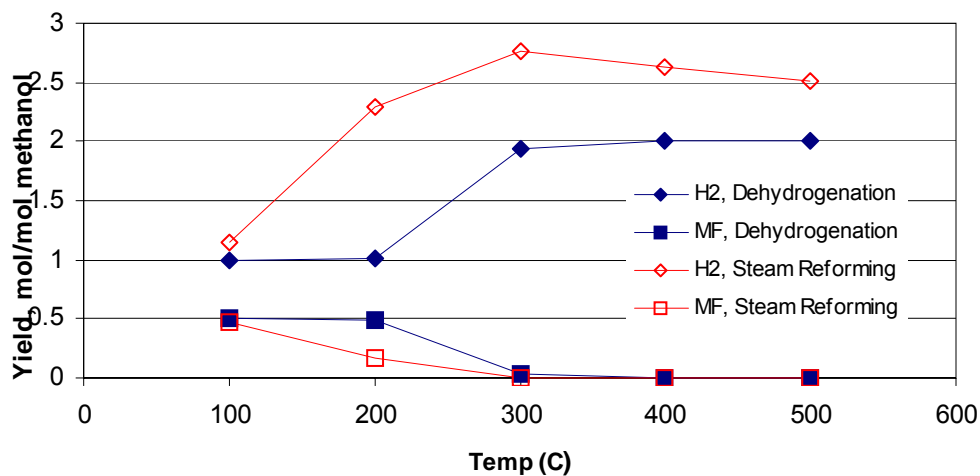


Figure 2. H₂ and MF productions by methanol dehydrogenation

Catalyst performance. Methanol dehydrogenation experiments have been carried out on copper-based catalysts at different temperatures, from 150°C to 250°C at 10°C intervals. Some preliminary experimental results have been obtained and are reported here. Methanol conversion and relative hydrogen production at various temperatures are shown in Figure 3

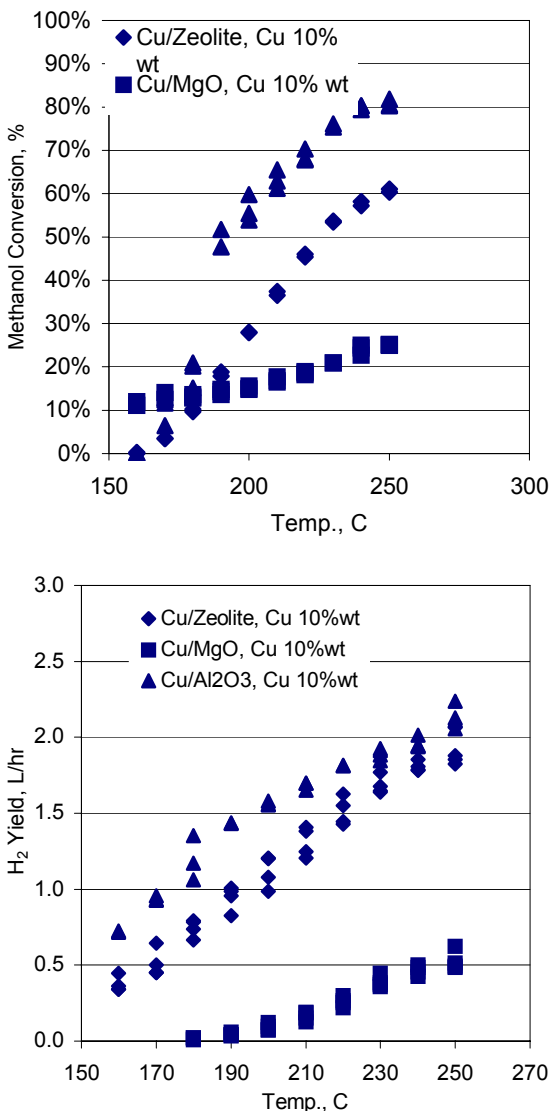


Figure 3. Methanol conversion and hydrogen production vs temperature.

Figure 3 shows that the conversion of methanol increases with increase in temperature with all three catalysts. Cu/Al₂O₃ is the most active catalyst; the conversion of methanol can reach 80% at 250°C. Cu/MgO is the least active; methanol conversion is below 25%. Conversion does not correlate with the BET surface area of the catalysts; the copper surface area, which will be explored in future work, may be more relevant to catalyst activity. Hydrogen yields show the same trend as with the conversion of methanol: Cu/Al₂O₃ > Cu/ZSM-5 > Cu/MgO. More than two liters of hydrogen per hour is produced at 250°C on Cu/Al₂O₃. Dimethyl ether is also

formed on the Cu/ZSM-5 and Cu/Al₂O₃ catalysts due to acidity of the supports. Only limited amounts of MF were obtained; modifications of catalysts are under investigation to improve MF selectivity. The effect of water concentration on H₂ and MF formation is also being studied.

Conclusions

Thermodynamically, coproduction of hydrogen and methyl formate is favored at temperatures below 220°C. At temperatures higher than 250°C, complete methanol decomposition is favored to form syngas with a ratio of H₂/CO=2. The presence of steam favors hydrogen but decreases methyl formate production. Copper catalysts are active for decomposition of methanol in the order of Cu/Al₂O₃>Cu/ZSM-5>Cu/MgO. An increase in methyl formate selectivity would reduce the CO content in the products. Promoters are needed to improve MF selectivity.

References

1. Iwasa, N.; Takezawa, N. *Top. Catal.* **2003**, 22, 215.
2. [Hashimoto, K.](#); [Toukai, N.](#) *J. Mol. Catal. A* **2002**, 186, 79.
3. Shreiber, E. H.; Roberts, G. W. *Appl. Catal. B* **2000**, 26, 119.
4. Lee, J. S.; Kim, J. C.; Kim, Y. T. *Appl. Catal.* **1990**, 57, 1.

Hydrogen by Catalytic Reforming of Glycols

B. Liu, Y. Zhang, J.W. Tierney and I. Wender
Department of Chemical Engineering, University of Pittsburgh

Introduction

Hydrogen is a clean and efficient fuel and it will be the ultimate fuel in the future. Currently, hydrogen is made mainly from fossil fuels by steam-reforming, partial oxidation, or gasification. Production of hydrogen by steam-reforming of hydrocarbons requires a complex combination of multiple processes to achieve low carbon monoxide levels (e.g., 10–100 ppm) to be used in PEM fuel cells. An important step toward a simple process for the production of hydrogen containing low levels of carbon monoxide may be made possible by the discovery that hydrogen can be produced by catalytic reforming of glycols in the liquid phase at temperatures near 240°C.¹⁻³ This process has the advantage that reforming of the oxygenated hydrocarbon and the water–gas shift (WGS) are both thermodynamically favorable at the same low temperatures, thus making it possible to conduct both reactions in one reactor. The process eliminates the need to vaporize water and glycol and leads to low levels of carbon monoxide.

In our studies we focused on ethylene glycol (EG), a chemical found in the cooling system of most vehicles, and on glycerol, a by-product of the hydrolysis of fats and oils to make biodiesel. We found both EG and glycerol could be reformed to hydrogen and carbon dioxide at 240°C. Hydrogen yields from reforming EG and glycerol were 82% and 70%, respectively.

Experimental

Catalyst preparation. Preliminary tests were carried out on Pt/Al₂O₃ with 1 wt% Pt purchased from Aldrich. The preparation of various Pt and Ni catalysts on different supports and with the addition of promoters is ongoing.

Catalyst testing. The continuous fixed-bed liquid phase microreactor with computer control as described in previous reports has been built and is currently in operation. The reactor is a 3/8 inch od and 1/4 inch id rod of stainless-steel tubular reactor with a packed bed of catalyst about 10mm long. A thermocouple inserted into the middle of the catalyst bed in the reactor insures accurate measurement of temperature. In this study, one gram of platinum on alumina powder was loaded into the reactor, and activated by hydrogen at a rate of 50 ml/min, with a temperature program ramping from room temperature to 250°C at 1°C /min, holding at 250°C for 2 hours. A liquid solution of 10 wt% ethylene glycol (or glycerol) was introduced in an up flow configuration at 6.0ml/h with a syringe pump. The total pressure of the system was regulated to 350psi-680psi with nitrogen. For each experiment, reaction temperature was gradually increased from 220°C to 270°C in 10 degree intervals. The system pressure was kept at 50psi over the water vapor pressure at that temperature to keep the system in the liquid phase. Liquid products were collected in a cold trap and analyzed by GC and GC-MS. The stream of effluent gas went through two automatic sampling valves and was analyzed by an online GC (HP5890) equipped with two packed columns: Porapak Q with FID for analysis of light organic products and Carboneiseive with TCD for analysis of H₂, CO, CO₂.

Results and Discussion

Aqueous-phase reforming of 10 wt% of EG or of glycerol solutions was carried out in the fixed bed tubular reactor. The effluent gas compositions for ethylene glycol reforming at various temperatures are shown in Table 1. At temperatures below 260°C, hydrogen and carbon dioxide constitute more than 99% of the gas. Methane and ethane products constitute less than 1% in most cases and increase with reaction temperature. Carbon monoxide could not be detected in these experiments. Analysis of the liquid phase is ongoing. Preliminary results show that liquid-phase products contain small amounts of alcohols (methanol and ethanol), organic acids (acetic and glycolic acids), and acetaldehyde.

Table 1. Gas effluent from reforming of EG

Temperature (°C)	H ₂ %	CO ₂ %	CH ₄ %	C ₂ H ₆ %
230	70.0	29.5	0.27	0.19
240	70.2	29.3	0.33	0.15
250	67.7	31.5	0.55	0.24
260	67.7	31.3	0.69	0.30
270	67.5	31.0	1.19	0.30

The composition of the gases produced by the aqueous-phase reforming of 10% glycerol is shown in Table 2. Compared to EG, glycerol produces five to ten times more methane. Reforming of glycerol is more complicated than that of EG.

Table 2. Gas effluent from reforming of glycerol

Temperature (°C)	H ₂ %	CO ₂ %	CH ₄ %	C ₂ H ₆ %
220	61.6	34.6	3.46	0.3
230	62.4	34.4	2.95	0.34
240	62.8	33.8	2.98	0.36
250	63.8	33.0	2.78	0.41
260	62.4	34.0	3.12	0.51
270	61.6	33.4	4.4	0.6

Hydrogen yields from reforming of EG and glycerol are shown in Figure 1. Hydrogen yields increase with temperature below 230°C and become flat above that temperature. Reforming of glycerol exhibits a higher hydrogen yield at 220°C but a lower flat hydrogen yield than that of EG. The maximum hydrogen yields obtained from reforming of EG and from glycerol in these experiments are 82% and 70%, respectively.

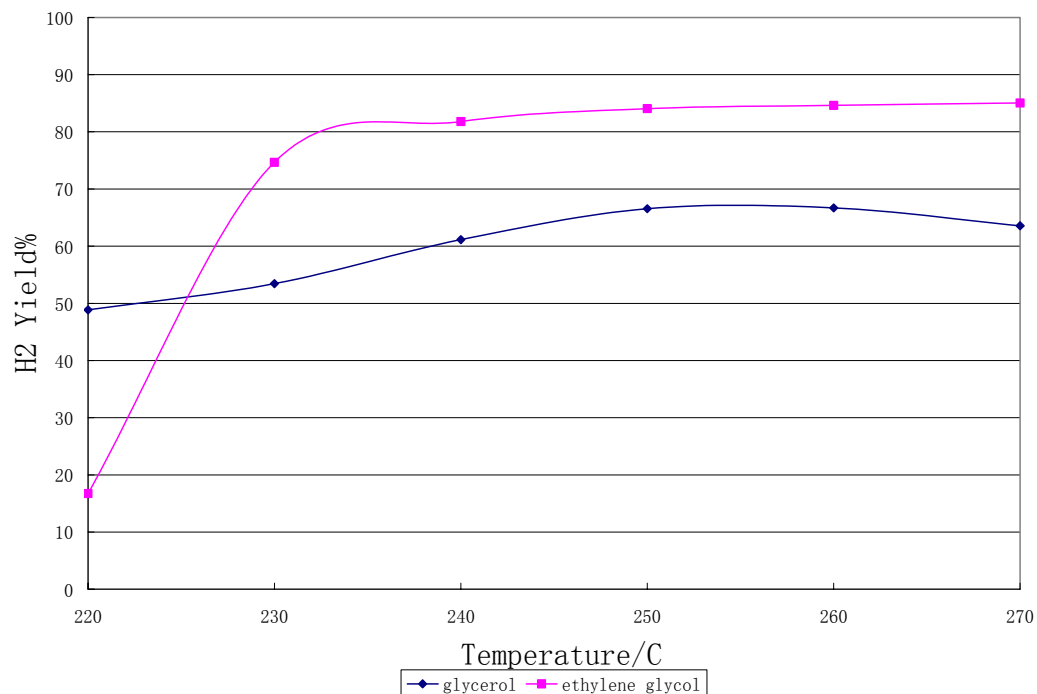


Figure 2. H₂ yields from aqueous-phase reforming of ethylene glycol and glycerol

Conclusions

Our experiments on the aqueous-phase reforming of ethylene glycol and of glycerol in a continuous system have shown that significant amounts of hydrogen are produced with low CO. This method for producing hydrogen appears promising for use in PEM fuel cells.

References

1. R. R. Davda, J. W. Shabaker, G. W. Huber, R. D. Cortright and J.A. Dumesic, *Applied Catalysis B: Environmental* 43 (2003), 13–26.
2. J. W. Shabaker, G. W. Huber, R. R. Davda, R. D. Cortright and J. A. Dumesic, *Catalysis Letters* 88 (2003), 1–2
3. J. W. Shabaker, R. R. Davda, G. W. Huber, R. D. Cortright and J. A. Dumesic, *Journal of Catalysis* 215 (2003), 344–352.

HYDROGEN PRODUCTION BY CATALYTIC METHANE DECOMPOSITION USING A SEMI-CONTINUOUS FLUIDIZED-BED REACTOR

Shankang Ma, Yuguo Wang, Naresh Shah, Gerald P. Huffman

University of Kentucky, 533 S. Limestone Street, Suite 107, Lexington, KY 40508-4005

Introduction

Previously, we have developed alumina supported binary catalysts, (M-Fe)/Al₂O₃ (M=Pd, Mo, or Ni), that are very active for catalytic dehydrogenation of lower alkanes to produce pure hydrogen and carbon nanotubes.^{1,2,3} One major setback in such laboratory scale experiments is accumulation of carbon nanotubes (CNT), a potentially valuable byproduct, within the reactor. In a fixed bed mode of operation, this CNT accumulation starts hindering the flow of the reactant and product gas streams and builds up a back pressure within a few hours.

One possible way to dislodge nanotubes anchored to the catalyst particles on the surface of the alumina support is to mechanically breaking the nanotubes at these linkages by physical agitation. Fluidization of the bed should induce turbulent flow of the catalytic bed media and repeated inter-particle collisions that could shear nanotubes from the active metallic catalysts. Once freed, CNT should be carried away by the fluidizing gas stream to be externally collected and the re-activated catalyst should continue to decompose methane, producing additional hydrogen and carbon nanotubes. In this paper, we report results from the preliminary tests carried out to validate the aforementioned hypothesis.

Experimental

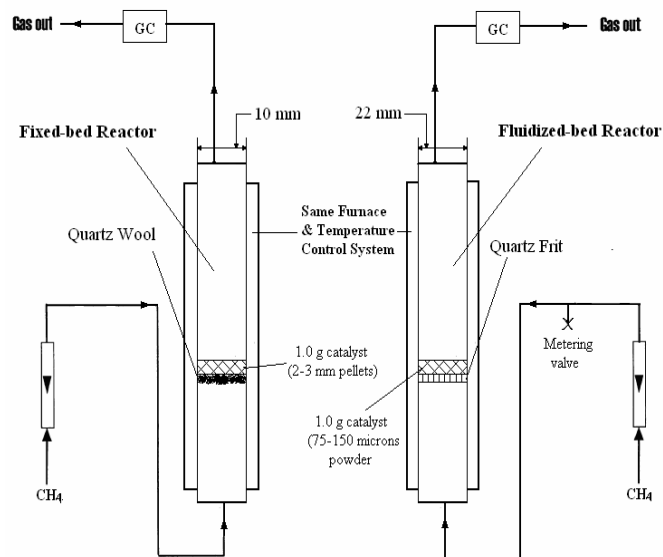


Figure 1 Comparison of fixed-bed and fluidized-bed reactors.

Most of the hydrogen production work using fluidized bed reported in the literature concern the production of syngas.^{4,5,6,7} When used for the production of carbon nanotubes, fluidized bed reactors are typically fed with higher carbon content gases and not methane.^{8,9,10,11,12} Lee et al.¹³ have used a fluidized bed reactor for hydrogen production from catalytic decomposition of

methane using activated carbon catalysts with very low methane conversion. Weizhong et al.¹⁴ have employed a two-stage fluidized bed reactor for production of hydrogen and carbon nanotubes from methane.

Figure 1 is a schematic diagram comparing salient features of our old fixed bed reactor¹ with the new fluidized bed reactor. The two setups are identical except for larger reactor diameter (for high methane flow rate required for fluidization) and a quartz frit fused to the quartz wall of the reactor instead of a quartz wool plug (for catalyst support). Because there is no thermal methane decomposition at a reactor temperature of 700 °C, the pores in the quartz frit were never plugged with carbon. By increasing the methane flow rate from 10 ml/min to >~100 ml/min, the reactor mode can be varied from fixed bed to fluidized bed. At high methane flow rates (15 l/min), the entire reactor can be emptied of catalyst and CNT very quickly and new catalyst can be added to the reactor from the top (not shown in the schematic) at low or zero methane flow rate.

For all fluidized bed reactor experiments, 1 gram of as prepared (0.5%Mo-4.5%Fe)/Al₂O₃ catalyst was used at reactor temperatures of 650-700 °C. To achieve good fluidization, the catalyst particle size was kept between 70 and 150 microns.

Results

Figure 2 shows volume percent hydrogen in the reactor exit stream as a function of time on stream for different methane feed flow rates. With increasing methane flow rate, hydrogen production efficiency decreases as methane-catalyst contact time decreases.

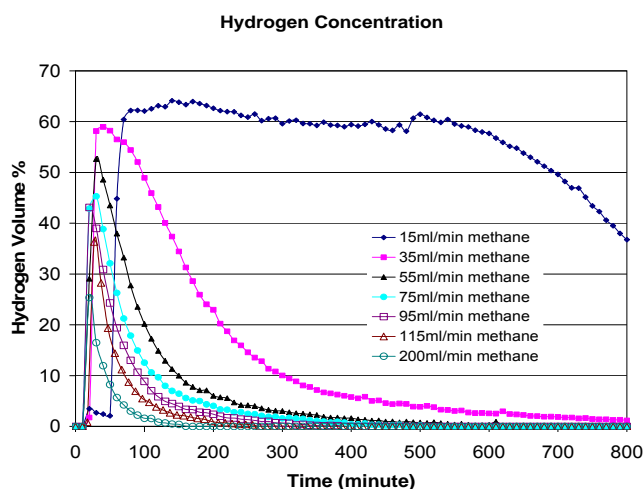


Figure 2. Time-on-stream hydrogen production at different methane flow rates.

Most of the hydrogen production work using fluidized bed reported in the literature concern the production of syngas.^{15,16,17,18} When used for the production of carbon nanotubes, fluidized bed reactors are typically fed with higher carbon content gases and not methane.^{19,20,21,22,23} Lee et al.²⁴ have used a fluidized bed reactor for hydrogen production from catalytic decomposition of methane using activated carbon catalysts with very low methane conversion. Weizhong et al.²⁵ have employed a two-stage fluidized bed reactor for production of hydrogen and carbon nanotubes from methane.

Table 1 Hydrogen production efficiency at different methane flow rates and different reactor modes

	Methane Flow Rate (ml/min)	Linear Velocity (m/s)	Total Methane Input (ml) in 800 minutes	Total Hydrogen Produced (ml) in 800 minutes	Efficiency (H ₂ /CH ₄)
Fixed bed Mode	15	2.37	12000	9210	77%
	35	5.52	28000	4830	17%
	55	8.68	44000	3350	8%
	75	11.84	60000	3110	5%
Fluid Bed Mode	95	14.99	76000	2830	4%
	115	18.15	92000	2000	2%
	200	31.57	160000	1790	1%

To compare efficiency of the hydrogen production, we have to compare areas under individual curves in figure 2. As shown in table 1, the reactor is most efficient in producing hydrogen at the lowest flow rate and highest reactant-catalyst contact time. As the flow rate increases, some of the methane just passes through the voids in the catalyst bed without coming in contact with any active metallic catalyst sites. At even higher flow rates, most of the methane acts simply as a fluidizing medium and not a reactant. As mentioned earlier, methane decomposition under these reaction conditions is purely a catalytic reaction and if a methane molecule does not come in direct contact with an active catalytic site, it will not undergo decomposition.

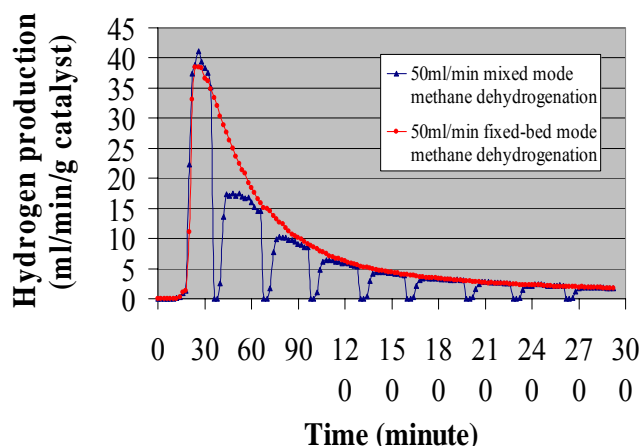


Figure 3 Comparison of fixed bed mode and mixed mode hydrogen production by catalytic methane dehydrogenation.

Based purely on these observations, there is no real advantage of operating the reactor in the fluidized mode. However, it is worth reflecting that the main reason for operating the reactor was not improving the activity. Rather, the tumbling and collisions of bed particles in a fluidized bed was hypothesized to cause separation of nanotubes from the anchoring metal catalyst sites. To achieve both high hydrogen production efficiency and separation of nanotubes, a periodic mode switching experiment was performed. In such an operation, the reactor will be mostly operated in the high efficiency, low flow rate, fixed bed mode for generation of hydrogen. At regular intervals, the flow rate can be increased for short durations, at the penalty of low hydrogen production efficiency, to fluidize the bed in order to separate nanotubes from the catalyst bed material and remove them from the reactor. Figure 3 compares hydrogen production for a fixed bed mode operation and a periodically fluidized fixed bed mixed-mode of operation. It is evident that after short fluidization, the active catalyst sites do not regain their catalytic activity because of separation and harvesting of the CNT.

During initial shakedown experiments of the new reactor set-up at different methane flow rates, we had noticed that at the very high methane flow rate (15 l/min), the catalyst bed can be fluidized very vigorously and expanded completely out of the length of the tube. As a result, all the catalyst bed material can be ejected out of the reactor almost instantaneously at the operating temperature just by increasing the flow rate. Figure 4 shows the hydrogen production for four such replenishing/complete blow out cycles.

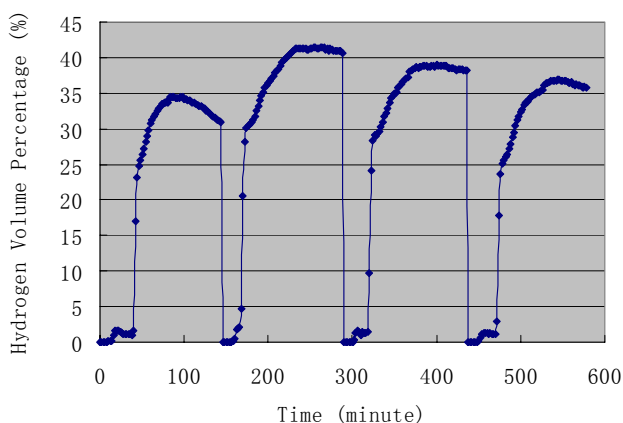


Figure 4 Semi-continuous hydrogen production by cyclic blowing out the reacted catalysts and attached CNT and replenishing the reactor with completely new catalytic bed material at 650 °C.

Conclusions

To overcome the plugging of the fixed bed reactor by CNT in methane dehydrogenation and to make hydrogen and nanotube production continuous, fluidized-bed mode and mixed-mode catalytic dehydrogenation experiments were performed. These experiments showed that the hydrogen production is most efficient only in a fixed bed mode at low methane flow rates. The results also negated the validity of the hypothesis that the tumbling and inter particle collisions of bed material would efficiently separate nanotubes anchored to the catalyst bed particles. A very high methane flow rate was successfully used to rapidly blow the entire bed material and attached nanotubes out of the reactor. The reactor was replenished with fresh catalyst at the operating temperature to generate hydrogen in a very efficient semi-continuous process.

Publications

Shankang Ma, Yuguo Wang, Naresh Shah, Gerald P. Huffman, “Hydrogen Production by Catalytic Methane Decomposition using a Semi-Continuous Fluidized Bed Reactor”, *Prepr. Pap.-Am. Chem. Soc., Div. Fuel Chem.*, **50 (2)** (2005), in press; full paper in preparation.

Future work

Optimization work on hydrogen production reactors will continue.

References

- ¹ Shah, N.; Panjala D.; Huffman, G.P. *Energy & Fuels*, **2001**, *15*(6), 1528-34.
- ² Shah, N.; Wang, Y.; Panjala D.; Huffman, G.P. *Energy & Fuels*, **2004**, *18*(3), 727-735.
- ³ Wang, Y.; Shah, N.; Huffman, G.P. *Catalysis Today*, **2005**, *99*, 359-364.
- ⁴ Santos, A.; Menendez, M. Monzon, A.; Santamaria, J.; Miro, E.E.; Lombardo, E.A. *J. Catal.* **1996**, *156*, 83.
- ⁵ Bharadwaj, S.S.; Schmidt, L.D. *J. Catal.* **1994**, *146*, 11.
- ⁶ Opoku-Gyamfi, K.; Adesina, A.A. *Appl. Catal. A: Gen.* **1999**, *180*, 113.
- ⁷ Tomishige, K., *Catalysis Today* **2004**, *89*, 405–418.
- ⁸ Wang, Y.; Wei, F.; Luo, G.; Yu, H.; Gu, G., *Chemical Physics Letters* **2002**, *364*, 568–572.
- ⁹ Qian, W.; Wei, F.; Wang, Z. *AIChE Journal* **2003**, *49*(3), 619-625.
- ¹⁰ Mauron, P.; Emmenegger, C.; Sudan, P.; Wenger, P.; Rentsch, S.; Zuttel, A. *Diamond and Related Materials*, **2003**, *12*, 780-785.
- ¹¹ Corrias, M.; Caussat, B.; Ayrat, A.; Durand, J.; Kihn, Y.; Kalck, P.; Serp, P. *Chem. Engr. Sc.*, **2003**, *58*, 4475-4482.
- ¹² Venegoni, D.; Serp, P.; Feurer, R.; Kihn, Y.; Vahlas, C.; Kalck, P. *Carbon*, **2002**, *40*, 1799-1807.
- ¹³ Lee, K.K.; Han, G.H.; Yoon, K.J.; Lee, B.K. *Catalysis Today* **2004**, *93-95*, 81–86.
- ¹⁴ Weizhong, Q.; Tang, L.; Zhanwen, W.; Fei, W.; Zhifei, L.; Guohua, L.; Yongdan, L. *Appld. Catal. A: General*, **2004**, *260*, 223-228.
- ¹⁵ Santos, A.; Menendez, M. Monzon, A.; Santamaria, J.; Miro, E.E.; Lombardo, E.A. *J. Catal.* **1996**, *156*, 83.
- ¹⁶ Bharadwaj, S.S.; Schmidt, L.D. *J. Catal.* **1994**, *146*, 11.
- ¹⁷ Opoku-Gyamfi, K.; Adesina, A.A. *Appl. Catal. A: Gen.* **1999**, *180*, 113.
- ¹⁸ Tomishige, K., *Catalysis Today* **2004**, *89*, 405–418.
- ¹⁹ Wang, Y.; Wei, F.; Luo, G.; Yu, H.; Gu, G., *Chemical Physics Letters* **2002**, *364*, 568–572.
- ²⁰ Qian, W.; Wei, F.; Wang, Z. *AIChE Journal* **2003**, *49*(3), 619-625.
- ²¹ Mauron, P.; Emmenegger, C.; Sudan, P.; Wenger, P.; Rentsch, S.; Zuttel, A. *Diamond and Related Materials*, **2003**, *12*, 780-785.
- ²² Corrias, M.; Caussat, B.; Ayrat, A.; Durand, J.; Kihn, Y.; Kalck, P.; Serp, P. *Chem. Engr. Sc.*, **2003**, *58*, 4475-4482.
- ²³ Venegoni, D.; Serp, P.; Feurer, R.; Kihn, Y.; Vahlas, C.; Kalck, P. *Carbon*, **2002**, *40*, 1799-1807.
- ²⁴ Lee, K.K.; Han, G.H.; Yoon, K.J.; Lee, B.K. *Catalysis Today* **2004**, *93-95*, 81–86.
- ²⁵ Weizhong, Q.; Tang, L.; Zhanwen, W.; Fei, W.; Zhifei, L.; Guohua, L.; Yongdan, L. *Appld. Catal. A: General*, **2004**, *260*, 223-228.